Addis Ababa University
አዲስ፡አበባ፡ዩኒቨርሲቲ
SEEK WISDOM, ELEVATE YOUR INTELLECT AND SERVE HUMANITY !

ADDIS ABABA UNIVERSITY

COLLEGE OF NATURAL AND COMPUTATIONAL SCIENCES

SCHOOL OF EARTH SCIENCES

DETECTION AND MAPPING DISTRIBUTION OF IRON ORE MINERALIZATION USING ASTER AND SENTINEL−2 MSI DATA IN SEKOTA DISTRICT, NORTHERN ETHIOPIA

BY

JERBAW TIRUNEH ABEJEHU
ID NO: GSR/5621/15
ADVISORS:
DR. BINYAM TESFAW
PROF. WORASH GETANEH

ADDIS ABABA UNIVERSITY
ADDIS ABABA, ETHIOPIA
MAY 25, 2024

ADDIS ABABA UNIVERSITY
COLLEGE OF NATURAL AND COMPUTATIONAL SCIENCES
SCHOOL OF EARTH SCIENCES

DETECTION AND MAPPING DISTRIBUTION OF IRON ORE MINERALIZATION USING ASTER AND SENTINEL−2 MSI DATA IN SEKOTA DISTRICT, NORTHERN ETHIOPIA

A THESIS SUBMITTED TO THE SCHOOL OF EARTH SCIENCES, ADDIS ABABA UNIVERSITY IN PARTIAL FULFILLMENT OF THE REQUIREMENTS FOR THE DEGREE OF MASTERS OF SCIENCE IN REMOTE SENSING AND GEO-INFORMATICS

BY:

JERBAW TIRUNEH ABEJEHU
ID NO: GSR/5621/15

Addis Ababa University
Addis Ababa, Ethiopia
May 25, 2024

Declaration

I, hereby, affirm that I have conducted the thesis titled "Detection and mapping distribution of iron ore mineralization using ASTER and Sentinel−2 MSI data, in Sekota district, Northern Ethiopia." under the guidance of Dr. Binyam Tesfaw, associate professor of Remote Sensing and Geo-informatics at the School of Earth Sciences, Addis Ababa University, and prof. Worash Getaneh, professor of economic geology at the School of Earth Sciences, Addis Ababa University. This research was undertaken between the years 2022 and 2024 as part of my master of science program in remote sensing and geo-informatics. Furthermore, I confirm that this work has not been submitted to any other university or institution in pursuit of any degree or diploma.

Place: Addis Ababa, Ethiopia
Date: May 25, 2024

(Jerbaw Tiruneh)

Addis Ababa University

College of Natural and Computational Sciences

School of Earth Sciences

This is to certify that Mr. Jerbaw Tiruneh has conducted a thesis entitled: "Detection and mapping distribution of iron ore mineralization using ASTER and Sentinel−2 MSI data in Sekota district, Northern Ethiopia" submitted in partial fulfillment of the requirements for the Master of Science degree in Remote Sensing and Geoinformatics at Addis Ababa University. This thesis adheres to Addis Ababa University's thesis guidelines and meets the required quality and standards.

Approved by Board of Examining Committees

1. Dr. Binyam Tesfaw ____/_______/_________
   (**P.Advisor**) **Signature** **Date**

2. Prof. Worash Getaneh ______________________________________/_________/_________
   (**Co-Advisor**) **Signature** **Date**

3. Prof. V. Suryabhagavan ____/__________/_____
   (**Examiner**) **Signature** **Date**

4. Prof. Dereje A.____/___________/______
   (Examiner) **Signature** **Date**

5. Dr. Bayissa Regassa______________________________________/____________/_______
(**Head of School of Earth Sciences**) **Signature** **Date**

Acknowledgments

I am incredibly grateful to my advisor, dr. Binyam Tesfaw, associate professor of Remote Sensing and Geo-informatics, at the School of Earth Sciences, Addis Ababa University, for his invaluable guidance throughout this thesis. His patience, constructive feedback, and progressive approach shaped this work. I also extend my sincere thanks to Professor Worash Getaneh, professor of Economic Geology, at the School of Earth Sciences, Addis Ababa University for his insightful comments and timely guidance.

My deepest appreciation goes to Bonga University for the financial support that enabled me to pursue my postgraduate studies in the remote sensing and geo-informatics stream at Addis Ababa University. I am also grateful to the School of Earth Sciences, Addis Ababa University for providing access to the essential remote sensing and GIS lab facilities.

On a personal note, I am immensely thankful to Ms. Israel A. for her unwavering love and encouragement, which fueled my energy throughout this journey. My sincere thanks also go to Ms. Workinesh J. for her material and moral support.

Finally, I am grateful to all my friends and remote sensing and geo-informatics classmates for their contributions of ideas and their constant encouragement during my studies and this research work.

Table of Contents

List of Figures

List of Tables

List of Abbreviations

ASTER	Advanced spaceborne thermal emission and reflection radiometer
ASB2/B1	ASTER band 2/ band 1
ASB4/B5	ASTER band 4/band 5
CEM	Constrained Energy Minimization
CHIRPS	Climate Hazards Group InfraRed Precipitation with Station
DEM	Digital Elevation Model
DN	Digital Number
EGI	Ethiopian Geological Institute
ENVI	Environment for visualization of images
ERSDAC	Earth Remote Sensing Data Analysis Center
ESRI	Environmental System Research Institute
ETM	Enhanced Thematic Mapper
FLAASH	Fast Line-of-sight Atmospheric Analysis of Spectral Hypercubes
FoM	Figure of Merit
GEE	Google Earth Engine
GPS	Global Positioning System
L1T	Level One Trigger
LSU	Linear spectral unmixing
LULC	Land-use Land-cover
MSL	Mean sea level
METI	Ministry of Economy Trade and Industry
MNF	Maximum noise fraction
MSI	Multispectral imager
MTMF	Mixture-tuned matched filtering
NASA	National Aeronautics and Space Administration
NDVI	Natural Difference Vegetation Index
OLI	Operational land imager
PC	Principal component
PC4	Principal component 4
PC3	Priincipal component 3

PCA	Principal component analysis
PPI	Pixel Purity Index
SAM	Spectral angle mapper
S2B4/B2	Sentinel 2 band 4 / band 2
S2B11/B12	Sentinel 2 band 11 /band 12
SDI	Spectral divergence information
SFF	Spectral feature fitting
SMACC	Sequential Maximum Angle Convex Cone
SSGIE	Space Science & Geospatial Institute of Ethiopia
SWIR	Short wave infrared region
TIR	Thermal Infrared
USGS	United States Geological Survey
VNIR	Visible and Near Infrared
X	Mean
XRD	X-ray diffraction

Detection and mapping distribution of iron ore mineralization using ASTER and Sentinel 2 MSI data in Sekota district, Northern Ethiopia
Jerbaw Tiruneh Abejehu, MSc. Thesis
Addis Ababa University, May 2024

Abstract

Iron plays a vital role in fueling the economic development and technological advancement of a country. Despite Ethiopia, being endowed with a large amount of iron ore resources in different parts of the country, prospective zones are not delineated properly. Therefore, this research aims to identify the iron ore prospective zones in the Sekota district of Ethiopia utilizing ASTER and Sentinel 2B satellite data for further onsite exploration and testing. In addition, powder diffraction analysis was conducted to determine the type of iron ore. The image processing techniques such as band ratio, ASTER band 2/band 1 (ASB2/B1) and Sentinel 2 band 4 /band 2 (S2B4/B2), principal component analysis (PCA), and subpixel level mapping techniques including linear spectral unmixing (LSU) and mixture-tuned matched filtering (MTMF) were used to map hematite abundance. ASTER band 4/ band 5 (ASB4/B5) and Sentinel 2 band 11/band 12 (S2B11/B12) ratios were also used to map the distribution of lateritic iron. ASB2/B1 and S2B4/B2 band ratios mapped hematite iron ore covering an area of 102.5 and 97. 68 km^2 respectively. ASB4/B5 band ratio detected 138.46 km^2 of lateritic iron and the S2B11/B12band ratio delineated a comparably 168.13 km^2 area. The selected PC4 of ASTER delineated hematite mineralized zones covering 133.40 km^2 and Sentinel 2 PC3 of 110.70 km^2 area. A very high match was found between the extracted hematite endmember and USGS resampled hematite spectra. The spectral fit was 0.74 for ASTER and 0.86 for Sentinel 2. Hematite anomaly zones were identified with MTMF and LSU techniques using these endmembers in different parts of the study area. Powder x-ray diffraction analysis revealed high hematite phases ranging from 36.8%−85.5% of Fe_2O_3. A strong positive correlation between was found S2B4/B2 and S2B4/B2 (r=0.83), ASB2/B1 and ASTER PC4 (r=0.94). Moderate correlations for ASB2/B2, S2B4/B2 (r=0.44), PCA (r=0.44), ASTER and Sentinel−2 MTMF (r=0.36). Results of both datasets show comparable areal coverage and overlay with three of the existing known iron occurrence polygons. Techniques employed in this research were effective in narrowing hematite mineralized potential zones for further exploration and can be used in other localities.

Keywords: Band ratio, PCA, Endmember collection, MTMF, XRD

CHAPTER ONE

1. Introduction

One of the important applications of remote sensing is geological discussion and mineral detection from the reflectance properties of the Earth's materials (Saibi et al., 2018; Shirazy et al., 2021). Satellite images are extremely useful in solving various geological problems. They are used as critical tools in many sectors of geology, including but not limited to geotechnical investigation, groundwater exploration, regional geology, structural mapping, mineral exploration, geomorphology, natural hazards mapping, and so on (EG Sciences, 2022; Saibi et al., 2018; Shirazy et al., 2021). Products of remote sensing investigations can be used as a low-cost, preliminary screening tool to identify the areas for further sampling and geological studies (Lupa et al., 2020). Integrating remote sensing and other geological techniques in mineral exploration typically increases the effectiveness in identifying mineralized zones and lowers the uncertainty frequently connected with mineral prospecting (Ombiro et al., 2021).

Hyperspectral and multispectral imageries with reliable spatial resolution were effectively utilized for geological investigations (Peyghambari & Zhang, 2021). Different researchers (Dadon et al., 2011; Zhang & Li, 2014) have used freely available EO-1 Hyperion data for lithological classification using an advanced SAM technique. Hyperion data is also widely used for prospecting of minerals such as alteration minerals, iron ore deposits, and sulfate-bearing ore deposits (Bishop et al., 2017; Zadeh et al., 2013). Many multispectral imageries take advantage of wider area coverage and free accessibility than space-born EO-1 Hyperion data. Due to this reason, numerous multispectral remote sensing imageries including Landsat 8, ASTER, WorldView 3, SPOT-5, and Sentinel−2 MSI imageries were widely used throughout the world for geological investigations including lithological discrimination and lineament extraction (Bishta & Sonbul, 2021; Marzouki & Dridri, 2022;) and mineral mapping (Honarmand et al., 2012; Sun et al., 2017).

The most commonly used conventional digital image processing techniques in geological studies include false color composites and band ratios for lithological discrimination (Bajwa et al., 2020; Gad & Kusky, 2007; Khalifa et al., 2020) and locating mineral deposits (Fatima et al., 2017; Gopinathan et al., 2020; Osinowo et al., 2021). The band ratio technique is performed by dividing the high-reflectance band by low-reflectance (high-absorption) bands to highlight specific geological targets. It enhances spectral properties while minimizing undesired information and highlights some targets that cannot be observed in the original data, allowing them to be easily interpretable (Beiranvand Pour & Hashim, 2014). Other advanced digital image processing techniques built-in with commercial software like ENVI are widely used for mineral mapping. The feature-oriented principal component technique developed by Crosta and Moore in 1989 was effectively used for alteration mineral mapping by different researchers (Crosta et al., 2003; Honarmand et al., 2012). Improvements in scene cover, spatial resolution, and spectral resolution of satellite sensors produce large datasets making information retrieval difficult. A technique commonly used to reduce the dimensionality of large satellite images, making data more interpretable while also decreasing information loss, is principal component analysis (PCA) (Jolliffe & Cadima, 2016). Results from different research show that independent component analysis is more effective in detecting geological anomalies (Oskouei, 2010; Shirmard et al., 2020; & Yang & Cheng, 2015). Spectral angle mapper, spectral information divergence, and spectral feature fitting techniques are also widely used for the detection of mineral anomalies using reference spectra. These techniques evaluate the spectral curve similarity and fit of absorption features to reference spectra (Kayet et al., 2018; Shaik et al., 2021; Vignesh & Kiran, 2020).

The use of satellite remote sensing in Ethiopia for geological applications is in a young stage due to several factors. The unavailability of spectrally and spatially high-resolution images is the main problem in the country. Ethiopia has diverse and complex topographical and geological features which makes it difficult to create an automated model for regional-scale mapping. Using public domain satellite datasets such as ASTER, Landsat Series, and some Sentinel 2, there have been some attempts at lithological and structural mapping (Gani & Abdelsalam, 2006; Seid & Suryanarayana, 2021) and detection of different types of mineralized zones including hydrothermal alteration mineral mapping (Raggiunti et al., 2021) and iron oxides mapping (Abay et al., 2022) using remote sensing data in Ethiopia. Remote sensing data with geospatial techniques are more widely applied in the area of hydrogeological mapping than in mineral resource exploration in the country. Ethiopian Geological Institute has identified many metallic mineral resources in many parts of the country though there have been several geologically unexplored areas in the country. One of geologically the most unexplored areas is the Waghmra zone despite its large reserve for many economic minerals. According to a short synopsis report conducted on major resource bases and constraints for the development Waghimra zone, the area is the host of many economically valuable mineral resources such as iron, gold, zeolites, and gemstones (Shume et al., 2019). The mineral resource exploration activity was hampered by inadequate infrastructure and inaccessible exposures in the area. Unpublished reports on iron occurrence by the Ethiopian Geological Institute and private companies show that there is high hematite occurrence in the study area though their investigation relies only on roadside exposures. Consequently, this research aims to detect iron ore mineralized zones and map the spatial distribution using publicly available satellite images of ASTER and Sentinel 2 MSI data and evaluates the effectiveness of remote sensing techniques employed for mapping iron ore mineralization in the Sekota district.

1.1. Statement of the problem

Despite Ethiopia being endowed with extensive mineral resources, many parts of Ethiopia remain geologically under-explored (Tadesse et al., 2003). One example of a place in Ethiopia that has not been well explored geologically is the Waghimra zone, characterized by complex geological formations that host many mineral resources, especially iron ore deposits. Local communities (traditional craftsmen) use the exposed iron hosting rocks by smelting traditionally to prepare some tools. Exploration works done by the Ethiopian Geological Institute and Access Capital private company revealed the presence of high-grade hematite ore exposed on the surface of the earth. However, their study was only limited to a small number of surface exposures and didn't apply sufficient methods to discriminate iron ore mineralized zones in other localities. In such areas, remote sensing techniques play a very important role in identifying mineral anomaly zones using remote sensing image processing techniques that enhance the delineation of targets. Consequently, this research delineates surface geology, detects iron ore mineralized zones, and maps its distribution employing multi-remote sensing techniques such as band ratios, selective PCA, subpixel abundance mapping techniques such as mixture tuned matched filtering (MTMF), and linear spectral unmixing with ASTER and Sentinel−2 data to delineate occurrence of iron mineralization in unknown areas of Sekota district. Powder X-ray diffraction analysis (XRD) of samples taken from known Serrel, Akma Yehonnes, and Shinaba iron ore blocks was done and secondary geochemical analysis data was used to identify the type of iron ore.

1.2. Objectives of the study

The main aim of this research is to map iron ore mineralized zones and their spatial distribution using ASTER and Sentel−2 data, field observation, and X-ray diffraction analysis. The specific objectives include;

- Analysis of iron ore mineralization abundance using band ratio, feature-oriented PCA, mixture-tuned matched filtering, and linear spectral unmixing.
- Identifying the type of iron ore mineralization in the study area with x-ray and geochemical analysis.
- Evaluation and validation of remote sensing-based techniques utilized for iron mineralization detection.

1.3. Significance of the study

Iron plays a vital role in the development of a country's economy and technological improvement of a country. According to the United Nations database on international trade, Ethiopia imports an average of 705 million USD worth of iron in 2022 and is working to replace imported iron and steel with locally produced resources (Endale, 2022). This requires a comprehensive country-wide exploration of prospective areas in the country. One of the highly potential areas of the country is Waghimra zone which has a total economically feasible 29 million tons of iron (Content, 2017). However, the estimated tonnage is only considered surface exposures along the main road. However, many inaccessible places that have similar geologic formations with visible iron strips on the surfaces of exposed rocks are not mapped properly. In such cases, remote sensing exploration techniques allow the identification of iron-bearing zones. So, this research can be helpful for further detailed onsite exploration and the mining process by narrowing prospective areas in the study area.

1.4. Research questions

1. What are digital image processing techniques used to detect iron minerals?
2. What type(s) of iron mineralization is/are found in the study area?
3. Which sensors (ASTER and Sentinel 2 MSI) give better results in the detection and mapping of iron minerals?
4. Which digital image processing techniques better detect iron minerals?
5. What is the correlation between techniques employed in this study for mapping iron ore mineralization?

1.5. Scope of the study

The scope of this study is the detection and mapping of the distribution of iron ore mineralization using remote sensing techniques and identifying the type of the main iron ore with x-ray diffraction and geochemical analysis. The distribution of iron ore mineralization depends on several factors including but not limited to geological history, types of lithological units present, and presence of the iron formation processes like hydrothermal fluids and volcanism. This research also focuses on identifying the type of dominant iron ore mineralization in the study area.

1.6. Limitations

One of the primary limitations of this research is the inability to evaluate the grade/content of iron ore using multispectral satellite data. Space and airborne remote sensing datasets with high spectral resolution like hyperspectral imageries, which have a much wider range of wavelengths that offer precise quantification and grade estimation for different ore minerals. This research utilized multispectral remote sensing datasets, ASTER and Sentinel 2 which are effective in the identification and delineation of iron ore mineralized zones but not able to estimate the grade of an ore. Another limitation of this research is grain size can affect the spectral response of targets. Grain size might have an impact on the way light is reflected from the surface of an object. The iron ore with finer grain size and coarser grain might show different spectral signatures in electromagnetic radiation. Even though the substance is chemically the same, this can cause variation in the material's spectral signature and may result in errors in advanced image processing algorithms. One more limitation of this research is that the quantity of samples used for analysis is small, a total of 10 samples were taken for the X-ray diffraction analysis to identify the type and verify the results of different algorithms used in this study. Further research is required to verify these results and estimate reserves reliably for economic exploitation.

1.7. Organization of the thesis

This thesis is organized into six chapters. Introduction of the study including a problem statement, specifying the objectives of the study, and its limitations. In the second chapter, relevant and recent articles were reviewed in detail about the data used and techniques employed in their studies. A description of the study area in terms of geographic location, physiography, geological characteristics, and land-use and land-cover is included in chapter three. In this chapter, a description of the data and used, preprocessing and hematite iron abundance mapping techniques were described. Chapter four contains preprocessing and abundance mapping results. Finally, a discussion of the results and conclusion were included in chapters five and six respectively.

CHAPTER TWO

2. Literature review

2.1. Surficial mineral mapping using satellite images

Several satellite images have been utilized for geological studies since the first launch of Landsat in July 1972. Many public-domain satellite images including Landsat 8 and Sentinel 2 have particularly benefited mineral detection and mapping investigation in many parts of the world (Adiri et al., 2020). Satellite images have a greater variety of uses in mineral prospecting and mapping which allow geologists to identify mineral anomalies from surface exposures, track ongoing mining operations, and monitor the environmental impacts of mining activities. Many minerals have characteristic absorption and reflectance features at particular wavelength ranges in the electromagnetic spectrum (Chattoraj et al., 2020). This is due to characteristics of certain minerals that have undergone specific electronic energy level transitions connected to the modification of electronic orbitals (Okada, 2022). In this chapter recent research works that have utilized products of the public domain and commercial satellites for mineral exploration are reviewed thoroughly.

Alteration mineral zones were mapped using multisource satellite multispectral and hyperspectral remote sensing data. (Wu et al., 2023). For extraction of alterations of minerals, methods applied and images used depend on spectral resolution and position of minerals absorption features in the electromagnetic spectrum. Using alteration mineral absorption and reflective bands of different minerals on Landsat 8 OLI oxides of iron and alteration minerals were mapped by dimensionality reduction techniques called principal component analysis. Most magnesium and aluminum hydroxyl alterations such as chlorite and epidote, muscovite, illite, and kaolinite have characteristic absorption features in the SWIR region. Due to ASTER's high spectral resolution compared to Landsat 8, these minerals were extracted from ASTER by applying conventional processing techniques, principal component analysis, and mixture-tuned matched filtering. In this study, mixture-tuned matched filtering (MTMF) applied to ZY1-02D hyperspectral data was found effective in extracting alterations of minerals compared to other methods and datasets used.

Band ratios, MNF (minimum noise fraction), and independent component analysis techniques were utilized on Landsat 8 OLI and ASTER data to differentiate lithologies and different minerals (Baid et al., 2022). Phyllic (muscovite and illite), prophyllitic (chlorite), and argillic (kaolinite) alterations were suitably detected on ASTER data and iron oxides from Landsat 8 depending on the position of absorption of minerals features concerning the wavelength range of bands. The ASTER band ratio (ASB6/B8) and (ASB5+ ASB7)/B6 identified amphibole and sericite-illite-smectite minerals respectively at different lithological formations. Carbonate-chlorite-epidote minerals were detected by ASTER band ratio of (ASB7+ASB9)/B8. Landsat band6/band 5 (LB6/B5) and band6/band7 (LB6/B7)were used to extract ferric oxides and laterites respectively. In the research, they found that the minimum noise ratio, and PCA to ASTER were more effective in delineating different formations than Landsat 8.

Iron ore deposits were identified using Landsat 8 OLI data in Central Eastern Egypt (Ghoneim et al. 2022). The new Landsat 8 band ratio, band 6/band2 (LB6/B2) was used to detect iron-bearing host rocks. Crosta technique of principal component analysis involves an in-depth evaluation of the spectral behavior of iron minerals concerning Landsat 8 bands to select the best component that shows iron ore anomalies. The constrained energy minimization technique applied using USGS mineral spectra identified iron minerals similar to band ratio and principal component analysis. Before applying an algorithm for abundance mapping it is better to explore the quality of data. This means the images should be radiometrically and atmospherically corrected to get surface reflectance. Jing et al. (2014) suggested a straightforward technique for ASTER data atmospheric correction using hyperspectral data that yields excellent outcomes in vegetation-less and dry regions. They applied the ASTER band ratio for mapping the distribution of ferric iron, kaolinite, muscovite, and chlorite minerals. The principal component analysis technique analysis was not used in this study because it is not suited for large areas that require multiple scenes. This is due to mosaicking not possible as analyzed datasets have different eigenvalues. To reduce the dimensionality of CASI-SASI data the applied MNF technique and selected endmembers using pixel purity index. The MTMF method was utilized for delineating mineral distributions.

Various types of iron ore deposits were identified using the ASTER band ratio technique (Gopinathan et al., 2020). The variation is due to geologic and geomorphic factors that affect the formation of a certain iron mineral type. The ASTER band ratio techniques used for ferric and ferrous oxides were ASTER ASB2/B1 and (ASB5/B3) + (ASB1/B2). The band ratio result showed a high correlation result with geochemical analysis. Therefore, iron ore deposits can be effectively detected using ASTER data for areas where field survey is limited. Delineating the distribution of iron oxides with different digital image processing techniques was done in the Negash area, Tigray region of Ethiopia (Abay et al., 2022). Landsat 8 OLI band ratio, band4/band3 (LB4/B3) was applied to demarcate hematite-type iron mineralization that has a Fe^{+3} oxidation state. Similarly, the band ratio, band6/band5 (LB6/B5) was used to detect iron oxide which has a Fe^{+2} oxidation state. The ASTER band ratios, ASB2/B1, and combined band ratio (ASB5/B3 + ASB1/B2) were used to map iron oxides with Fe^{+3} and Fe^{+2} oxidation states respectively. The Crosta principal component analysis technique used by Abay et al. (2022) involved the selection of absorption and reflection bands of iron oxides to generate uncorrelated components. Later selection of a component for iron mineral mapping is also based on minerals' properties of absorption and reflection. Endmember selection for mixture tuned matched filtering was done by PPI and n-D visualizer.

Evaluation of satellite-based techniques including band ratio, principal component analysis (PCA), MTMF, and spectral angle mapper (SAM) for mapping hydrothermal alteration mineral zone mapping with ASTER data in Northern Iran shows a high correlation between results (Noori et al., 2019). The lithological units and the different alteration zones and silicification zones were mapped with selective principal component analysis and band ratio transformation. In principal component analysis, the first four bands of ASTER were employed for detecting iron ore mineralization zones, bands from bands 4-6 were employed for delineating argillic type alteration, bands 5-7 were selected for mapping Phyllic alteration zones, and bands 7-9 for detection propylitic alteration zones. Band selection was dependent on the characteristic reflective and absorption features of minerals. Different alteration mineral groups were detected with SAM and MTMF techniques.

Researchers employed different digital image processing techniques mapping alteration minerals using ASTER and Landsat ETM+ images (Hajibapir et al., 2014). They utilized all bands of ETM+ and all visible and near, and short-wave bands of ASTER for the calculation of principal component analysis. Generated principal components, the first and third components of ASTER were capable of detecting kaolinite and muscovite minerals which are characteristics of argillic and Phyllic alteration respectively in their study. The spectral angle mapper was also effective in the classification of argillic, Phyllic, and chlorite-type alteration zones. ASTER and high spatial and spectral resolution commercial satellite images, IKONOS, and WorldView 2 were utilized for mapping iron ore mineralization and ore controlling factors. They employed band combination and principal component analysis. Marble, diorite, and schist were discriminated with band combination, band ratio band 4/band1 (IKB4/B1), and band b5/band3 (IKB5/B3) of IKONOS. The first four bands of ASTER and IKONOS, and b1, b2, b3, b7, and b8 of the WorldView–2 data for principal component transformation. Finally, they concluded that high-resolution satellites can detect minerals at the mine scale. Lanfranchi et al. (2021) employed a SAM and MTMF algorithm on Sentinel 2 data to detect iron ore mineralization in West Congo Orogen. These techniques are useful in detecting the target by calculating spectral similarity images and reference spectra. Sentinel 2 sensor has many bands in absorption wavelength ranges of different iron minerals. Hematite-rich zones were delineated effectively with both techniques at 60 and 20 m spatial resolution. Utilization of Landsat 8 OLI and SRTM DEM data for litho-structural mapping of the Serdo area, Afar region of Ethiopia (Seid & Suryanarayana 2021). The applied convolution filter, principal component analysis, intensity hue saturation, and false color composite techniques to Landsat 8 data and hill-shade to DEM to extract geological units and structures. They mapped six main geological units and 1859 structures at a scale of 1:100,000. According to their study, spatially pan-sharpened VNIR and SWI bands of Landsat 8 are effective in identifying lithologic structures and their textural properties. Hydrothermal alteration minerals, different geological units mapping, and classification of surface features in the Main Ethiopian Rift area using Landsat 8 OLI data (Raggiunti et al., 2021). They used supervised classification techniques for lithological classification and hydrothermal manifestations mapping. A Total of 519 hydrothermal manifestations were used as training samples that were collected from different kinds of literature. Fault mapping was done using the existing database on geological structures in the Main Ethiopian Rift and manually digitizing from DEM. They found five geological classes associated with different hydrothermal activity.

Evaluation of the effectiveness of ASTER and Landsat 8 OLI data in litho-structural features was done in the Jbel Sagho region of Morocco (Marzouki & Dridri, 2022). The false color composite of ASTER 531 and analogous Landsat 8 751 were used to distinguish granites/rhyolites, aphanitic basalt from sandstone. Advanced remote sensing-based techniques such as PCA, and MNF, maximum likelihood classification, and spectral angle mapper were also employed in their study. Lineaments were digitized manually from DEM and automatically from both ASTER and Landsat 8. The lineaments extracted from Landsat 8 were few due to relatively low spatial resolution compared to the ASTER sensor. In their study, granitic formations, rhyolite and ignimbrite formations, and aphanitic basalts and sandstones were effectively discriminated using ASTER and

Landsat 8 false-color composites, PCA, and MNF. Results from maximum likelihood classification and spectral angle mapper are consistent with existing geological maps, especially for ASTER data.

2.2. Remote sensing-based techniques for iron minerals mapping

There are various digital image processing techniques developed for lithological discrimination and mineral mapping. In this review widely and effectively used techniques such as band ratios and band combinations, PCA, SAM, spectral divergence information (SDI), and spectral feature fitting are thoroughly investigated from different research works in different parts of the world. Effective application of such techniques requires a very good understanding of the procedure and how they are employed for different remote sensing data sets.

2.2.1. Band combinations and band ratios

Spectral band selection for false color composites to discriminate specific lithologies or minerals depends on the spectral response of the specific target. The optimum Index Factor technique is used for the automatic selection of best combinations instead of visual selection (Marzouki & Dridri, 2022). According to Marzouki and Dridri, false color combinations of components generated by principal component analysis enhance lithological identification. In their study, the Landsat 8 751 combination gives the best information for lithological delineation. It effectively delineated pelites, sandstones, diorites, and ignimbrites and the ASTER 531 band combination can discriminate granites, and aphanitic basalts from sandstones.

Band ratios are selected based on the spectral responses of a target. They are simple mathematical operations done by dividing the maximum reflectance values at one band and the minimum reflectance values at another band. All forms of iron ore mineralization can be detected by the band ratio of Sentinel 2 S2B4/B2 due to the distinctive high reflectance and absorption properties of iron minerals (Van Der Werff & Van Der Meer, 2016). Iron ore deposits such as hematite, jarosite, and goethite exhibit very similar characteristics in spectral response in the VNIR and SWIR range. Jarosite and hematite have reflectance peaks near 0.72 μm and 0.74 μm, and absorption troughs near 0.43 μm and 0.88 μm respectively. Based on this spectra response, several band ratios are developed depending on the spectral resolution of different sensors. Ge et al. (2018b) used three band ratios such as band 6/band 1 (S2B6/B1), band6 / band8a (S2B6/B8a), and band 6 + band 7/band 8a (S2B6+B7/B8a)of the Sentinel 2 for the extraction of hematite mixed with jarosite and goethite, and the mixture of iron-bearing minerals, respectively. These iron ores are ferric types of iron oxides. Ge et al. (2018b) detected them with a sentinel 2 band ratio of S2B11/B8 and a Landsat 8 band ratio of LB6/B5. Due to the mineral's spectral response characteristics at different wavelength locations, many mineral indices are proposed and used to identify specific minerals. ASB2/B1, (ASB5/B3 + B1/B2), band3/band4 and Landsat 8 general iron oxide red band/blue band, and band6/band5 were also effectively used by different researchers for mapping different iron oxides and hydroxides (Abay et al., 2022; Gopinathan et al., 2020; & Traore et al., 2020).

2.2.2. Selective PCA

The principal component analysis first proposed by Crosta and Moore (1989) and modified by Loughlin (1991) can be applied to large remote sensing data sets to produce different uncorrelated components in which one of the components enhances the spectral responses of certain minerals (Crosta et al., 2003). PCA technique has been used as a valuable tool for mapping minerals with different datasets in different parts of the world (Guha et al., 2018; Hung, 2020b; Wu et al., 2023). Many authors have used Crosta's principle to determine the representative PCA for the effective detection of the intended mineral (Abay et al., 2022; Honarmand et al., 2012; Traore et al., 2020). Its capacity to reduce data dimensionality and extract usable features from spectral data makes it very helpful in remote sensing applications, where it helps with mineral deposit mapping and identification. Abay et al. (2022) utilized the first four bands of ASTER and Landsat OLI bands 2, 4, 5, and 6 to calculate principal component analysis. Due to the enhancement of spectral information with principal component analysis, they were able to map the distribution of ferric and ferrous iron ore deposits in the Negash area. Hung (2022b) calculated principal component analysis using Sentinel 2B bands, b2, b8A, b11, and b12 to detect hydrothermal minerals in Vinh Phuc Province, Northern Vietnam. It was effective in mapping the distribution of hydrothermal minerals. Guha et al. (2018) transformed the first 6 bands of Landsat 8 from bands 2−7 to principal components. It allowed them to select the principal component that has spectral information of intended hydrothermal minerals. The fourth principal component generated from the first four bands of ASTER and Landsat 8 bands 2, 4, 5, and 6 effectively used to detect the distribution of iron oxides (Abay et al., 2022). Depending on the high reflection and absorption characteristics of the target mineral, certain bands are selected. To select the component that has spectral information of the target mineral, Eigenvalues are examined using characteristic reflectance and absorption bands. The target mineral is highlighted by bright pixels if the eigenvalue loading is negative in the absorptive band; the target mineral is highlighted by dark pixels if the eigenvalue loading of the reflective band is negative (Crosta et al., 2003).

2.2.3. Spectral angle mapper

Spectral Angle Mapper Classification (SAM) is an automated image classification technique that compares the angle between known reference spectra and unknown image spectra treating both of them as vectors in space. It computes the angle between the two vectors after converting the spectra into a vector in a space with the number of band dimensions (Shirazi et al., 2018). It is an easy and rapid technique in which a pixel spectrum having greater angles from the maximum specified angle match with the reference spectrum is not considered (Lillesand et al., 2015). The SAM algorithm uses endmember spectra that can be taken straight out of the image or spectral library (Noori et al., 2019). The benefit of the SAM algorithm is that it classifies according to the entire spectrum response rather than concentrating on particular absorption and reflection features (Chen et al., 2010). The degree of similarity between reference and image spectra is indicated by an angle between them. A smaller angle denotes a higher degree of similarity, whereas a wider angle indicates a low degree of similarity (ENVI help). SAM technique has been widely utilized for mapping hydrothermal alteration minerals (Rani et al., 2023; Shirazi et al., 2018; Noori et al., 2019).

2.2.4. Spectral feature fitting

Spectral feature fitting is used to determine the fit absorption curves of material in unknown image spectra with known spectra (Clark & Swayze, 1995). It uses a least square technique to calculate the fit of the absorption feature of the material on the two spectra. This technique detects materials by calculating the match of position, shape, and strength of absorption bands of the known spectrum with the image spectrum (Van Der Meer, 2004). Before applying the spectral feature fitting, the reference spectra should be resampled to image spectra, and the reliable wavelength range of reference spectra should be correct for better match and minimization of the error (Behnia, 2007; Jain & Sharma, 2018). Endmembers can be selected from the image by using a purity pixel index/n-D visualizer (Abay et al., 2022). Automatic selection of end members from an image especially from multispectral images is possible in ENVI software.

2.2.5. Constrained energy minimization

The constrained energy minimization (CEM) technique is a powerful supervised classification technique that allows target minerals to be identified and their distribution mapped even in situations where they are present in small amounts mixed with other materials (Ghoneim, et al., 2022). This technique is effective in subpixel mineral detection and is capable of detecting even subtle mineral signals from multispectral data separating subpixel targets within multispectral satellite data (Pour, et al., 2019). This method suppresses the background to the lowest possible level while maintaining a steady output energy (Du et al., 2003). The overall output energy image is reduced, and the total energy of each pixel is converted to suppress unwanted information and boost the target information. The CEM algorithm has performed better in delineating different types of alteration zones more accurately than the ACE and SAM algorithms, according to a comparison of the output from all three algorithms (Rani et al., 2023). CEM is a strong and adaptable instrument for mineral mapping, offering precise and comprehensive data with notable benefits over conventional remote sensing techniques. It is a useful tool for exploration and mapping in a mixed geological environment due to its adaptability, noise reduction capabilities, and subpixel detection abilities.

2.2.6. Mixture-tuned matched filtering (MTMF)

Applying pixel-level mapping techniques such as; band ratios and PCA techniques does not accurately map the target from the pixel containing mixed signatures. In such cases, sub-pixel level mapping techniques including MTMF, spectral unmixing, and SAM are important and are used to map specific mineral abundance from mixed spectra. It has been used by many researchers and requires end members of the target to be mapped (Abay et al., 2022; Yousefi et al., 2018). It utilizes four main steps; 1. Minimum noise fraction (MNF), pure pixel calculation, n-d visualization, and abundance mapping. MNF transform is a valuable technique in reducing the dimensionality of remote sensing data and increasing data quality by segregating components that have noise. The principle of MTMF for abundance mapping is it separates different spectral signatures within a pixel into discrete endmembers that coincide with different materials of pure minerals (Kruse & Perry, 2013). Various methods are available for endmember collection. Spectral hourglass and SMACC (Sequential Maximum Angle Convex Cone) are automatic endmember collection techniques in ENVI software. A spectral hourglass uses a simplex hull-based geometric method to gradually separate pure endmembers from a dataset whereas SMACC iteratively finds endmembers by measuring their angle with existing cones. Incases, where the endmembers generated by them are not representative of the target to be mapped; the spectral signature of known places would be used.

2.2.7. Evaluation of remote sensing-based techniques

Assessing the effectiveness of remote sensing-based techniques employed for mineral mapping can be done using different techniques. The validity and accuracy of results are also trusted if the methods/techniques used give comparable results with positive correlation. Baid et al. (2023) evaluated band ratio, independent component analysis, and MNF techniques used for geological unit mapping and mineral prospecting with ground data. The ground data used in this research were X-ray diffraction analysis and onsite reflectance spectrometry with a handheld spectroradiometer. Ghoneim et al. (2022) verified the performance of remote sensing-based techniques employed for mapping iron ore deposits using field observation and geochemical analysis. Jing et al. (2014) used field observation, x-ray analysis, and very high-resolution hyperspectral CASI and SASI data. In their research, they used techniques such as band ratios and MTMF techniques for mapping different minerals. Results showed that the mineral distribution mapping techniques with ASTER data were consistent and effective as validated by CASI, SASI mineral map, x-ray, and field spectra. In addition to the validation of satellite-based techniques for mineral mapping, the correlation between the techniques employed should be done. Pearson correlation coefficient has been widely used for checking the consistency of methods used (Gopinathan et al., 2020; Abay et al., 2022). Pearson correlation coefficient for two variables can be calculated using equation 1.

$$P(x, y) = \frac{\mathrm{cov}(x,y)}{\sigma x * \sigma y} \tag{1}$$

where cov is the covariance between the two variables whereas σx and σy represent the standard deviation of the x and y variables respectively. The consistency of the methods employed can be also determined by using random points of reliable numbers (Abay et al., 2022). Those random points are used to extract DN/reflectance values from respective remote sensing-based techniques used in the study. After extracting the values, the correlation between techniques can be established. Abay et al. (2022) have used existing geological and mineral polygons for verification of their results.

CHAPTER THREE

3. Materials and methods

3.1. Description of study area

The study area is located in the Waghimra zone of the Amhara region in Northeastern Ethiopia. Geographically it is situated between 38^{o} 48' 0"−39^{o} 18' 0" E Longitude and 12^{o} 26' 0"−12^{o} $54^{'}$ 0" N Longitude covering an area of 2009 km^{2} (Figure 3.1). The access to the Sekota district is a 614 km asphalted road from Addis Ababa to Korem town or a 602 km asphalted road from Djibouti to Korem Town. West of Korem town, a 90 km all-weather road leads to the town of Sekota. There is also a direct flight available from Addis Ababa to Lalibella town and the study area is located approximately 127 km north of Lalibela town Direct flight from Addis Ababa to Lalibella and 127 km North of Lalibella town is Sekota town. The area is characterized by rugged topography and elevation ranges from 1211 to 2716 m above MSL. There are three known iron occurrence blocks with visible iron crests at the surface and several unexplored localities having the same lithology and iron ore deposits in the various locations of the study area. These known occurrences are located at Sirrel Libanos, Shinaba, Akme Yohannes, and Gozakem Dastu localities. Sirrel iron ore site is located 14 km North West of Sekota town. The iron-ore mineralization occurs in two parts of this area. Shinaba iron ore mineralization is located 21 km North of Sekota town at the roadside. Iron ore mineralization at the Gozakem Dastu site is located approximately 9 km East to Southeast of Sekota town.

3.2. Drainage pattern

The study area has mainly a trellis type of drainage pattern in which smaller streams from steep mountainous sides join a major river running along the valley (Figure 3.2). Dendritic type pattern is also found in the Eastern part of Sekota town administration. Drainage pattern has geological implications, the area is characterized by tilted and later eroded sedimentary formations which pave the way to the formation of a trellis pattern. Major streams flow in Northwest, North, and Northeastern directions and later join a Tekeze river at different positions outside of the study area.

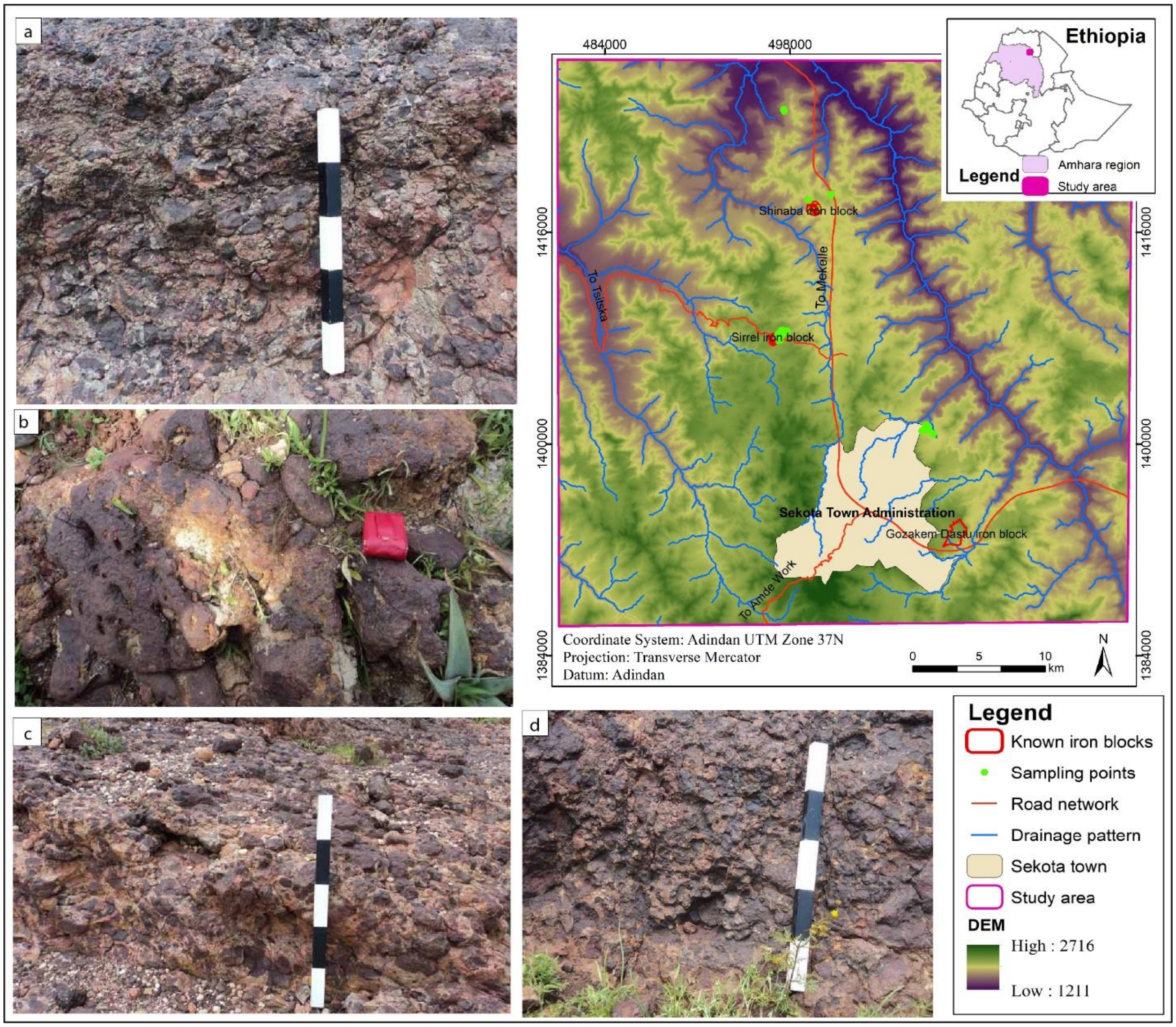

Figure 3. 1 Location map of the study area and image of iron ore mineralization at surface areas Shinaba (a), Sirrel (b), Akme Yohannes (c), and Gozakem Dastu (d) sites. Images were taken during local exploration work with ACS S.C.

3.3. Physiography

The area is characterized by rigid topography with parallel valleys running north to northeast. The elevation approximately ranges from 1250 m in valleys to 2716 m in mountainous areas (Figure 3.3). The ridges and hills are the dominant physiographic features in the study area. The highly elevated areas are located in the central and southern parts of the study area which are near to Sekota Town administration. Mesozoic and Tertiary volcanic rocks cover the majority of the hills and mountain ranges. It is characterized by physiographic features primarily composed of hills, cliffs, and mountain ridges that are divided by narrow flat terrains.

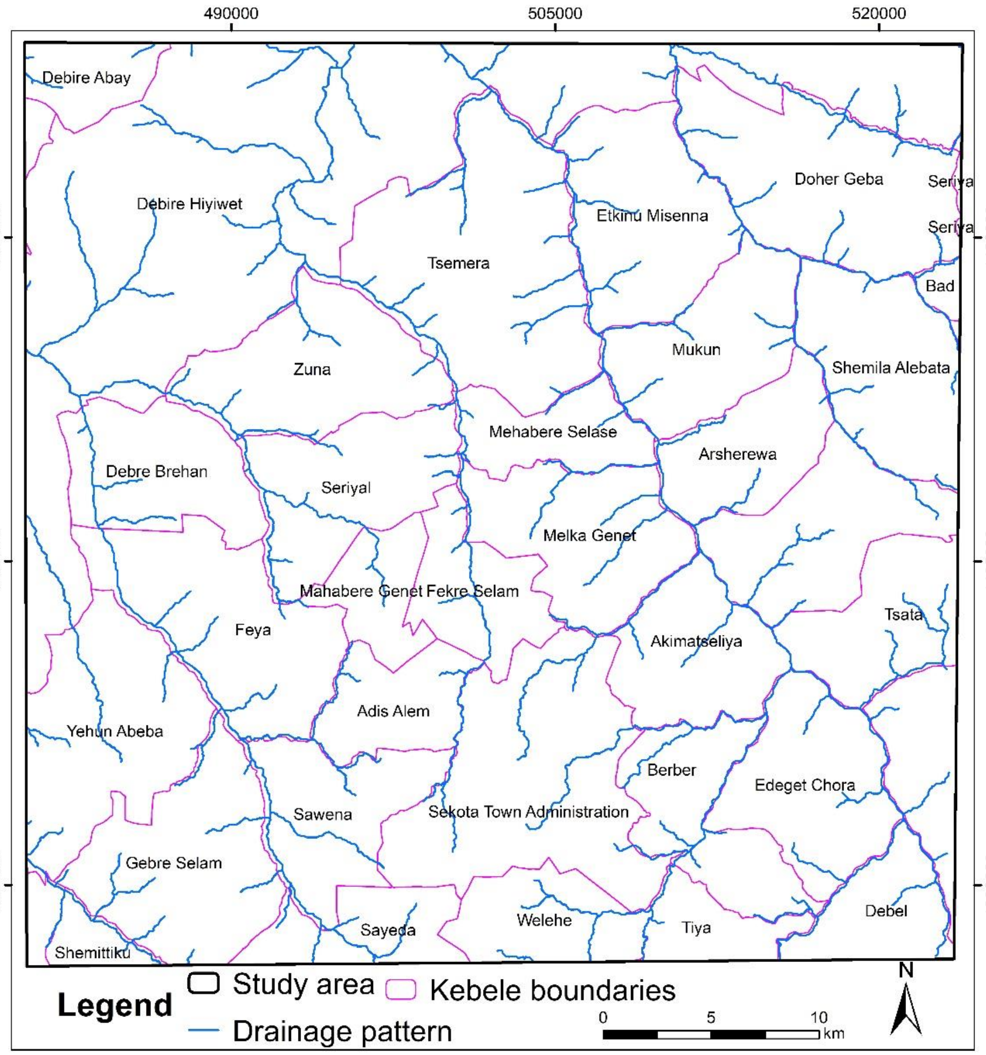

Figure 3. 2 Drainage map

3.4. Land-use and land-cover

According to Sentinel 2 10 m spatial resolution land use land cover data by impact Observatory and ESRI study area is characterized by five main land use land cover classes (Karra et al., 2022). The area has less vegetation and the dominant land cover in the area is bare land with or without grass. Most of the places are covered with exposed open rocks and soils. In this classification, exposed rock or soil, deserts and dunes, dry salt flats and pans, dried lake beds, and mines are examples of places that are classified as bare land that have little to no vegetation throughout the year. Examples of huge sand and desert areas are also included. The bare land covers 91 % of the total study area covering 1830 km^2 of area (Figure 3.4). Bare land is left open and a satellite base map was used. Other classes, agricultural land and built-up cover areas of 159.25 and 14.97 km^2

respectively (Table 3.1). Vegetation and water body cover is very small and they account for about 5.35 km^2. The absence of vegetation cover makes it favorable for the effective use of remote-sensing techniques for the detection of mineral resources from surface exposures.

Table 3. 1 Statistics and description of land-use land-cover classification

LULC classes	Area in (km^2)	Area in (%)
Waterbody	2.24	0.11
Vegetation	3.11	0.15
Agricultural land	159.25	7.92
Built-up	14.97	0.74
Bare land	1830.04	91.06

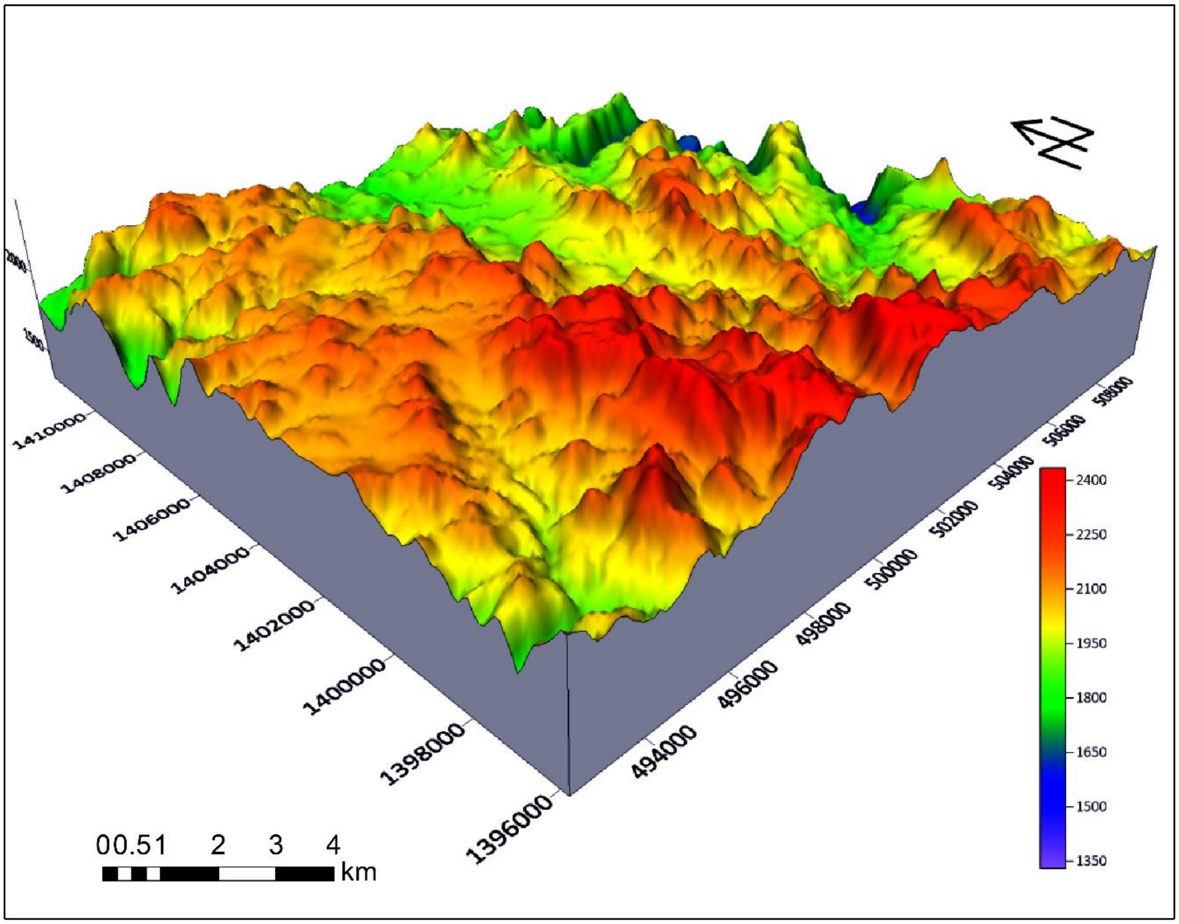

Figure 3. 3 Physiographic map

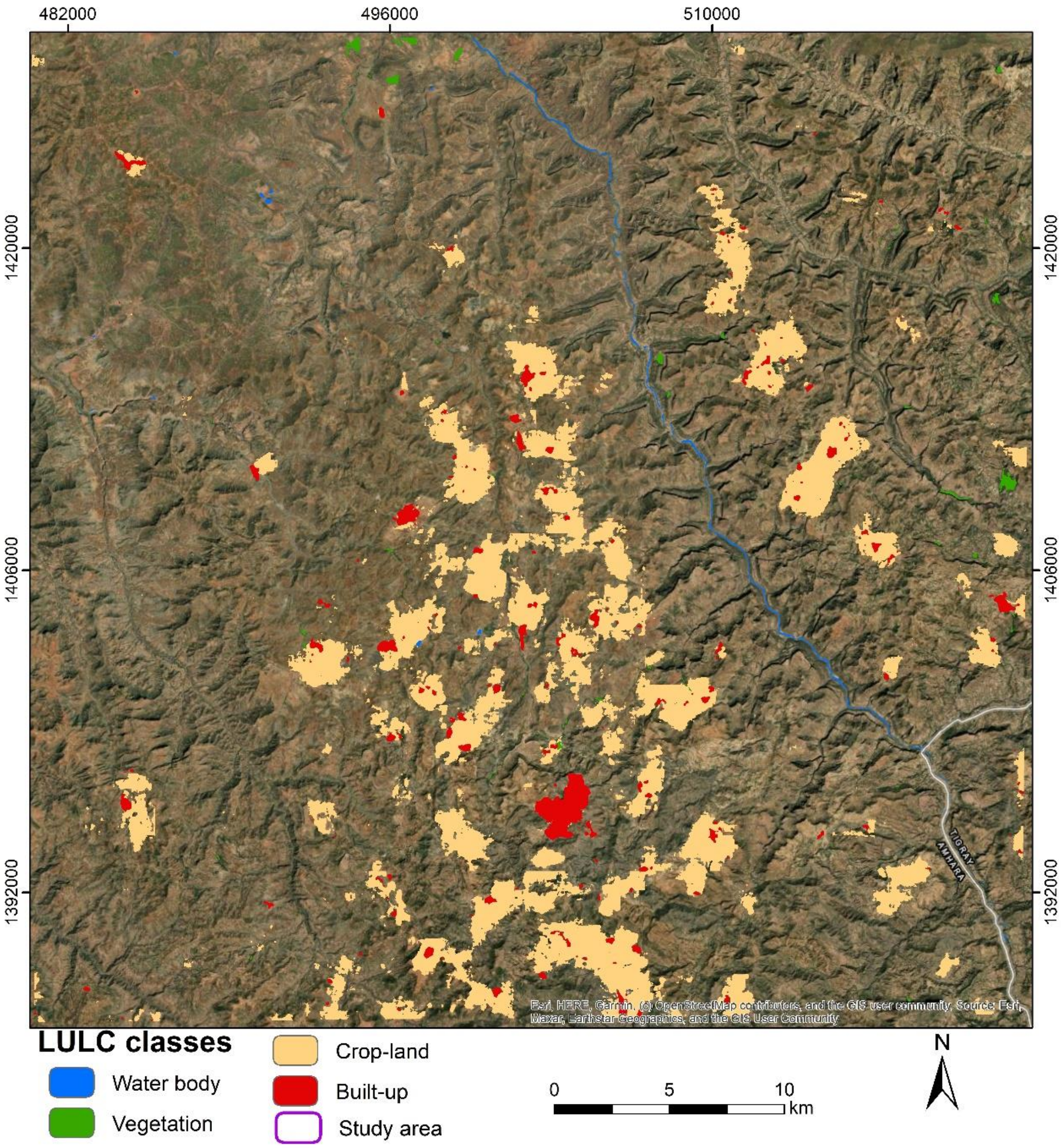

Figure 3. 4 Land-use land-cover map

3.5. Climate condition

Climate Hazards Center InfraRed Precipitation with Station data (CHIRPS) climate data was evaluated to see the climate condition of the area. According to this data, the area is characterized by a scarcity of rainfall, with only July and August getting greater than 200 mm of rainfall. The peak rainfall of 269 mm occurs in August. The highest temperature recorded was 32 °C in May, while the lowest temperature of 24°C occurred in August (Figure 3.5). Annual average rainfall and temperature are approximately 55m and 28.7 C^{o} respectively. The remote sensing data collection strategy in this research has considered this valuable weather condition to choose reliable months relevant for data collection to avoid coverage of the minerals on the surface by seasonal vegetation.

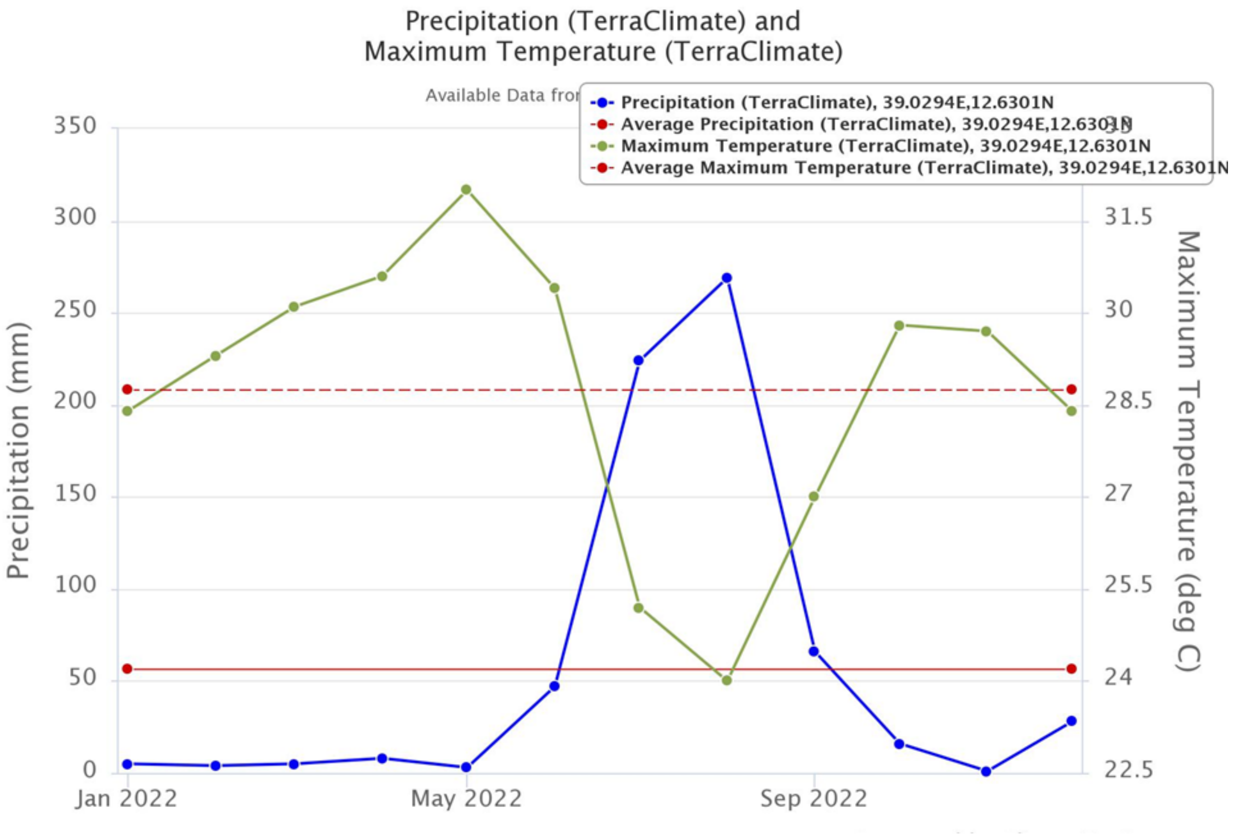

Figure 3. 5 Monthly average temperature and precipitation

3.6. Geological setting

The geology of Ethiopia consists of rocks of three main age groups: basement rocks of Neoproterozoic age, early Tertiary to Late Paleozoic sediments, sedimentary rocks, and corresponding Cenozoic volcanic rocks. Rifting that took place throughout the Cenozoic Era had a substantial impact on large parts of sedimentary succession according to geological studies conducted by the Ethiopian Institute of Geological Surveys (EIGS, 1999). The stratigraphic succession of Northern Ethiopia can be arranged in ten units, with the youngest at the top (Basalts of the Trap Series; Mekele Dolerites; Axum-Adua Plugs) and the oldest (Precambrian basement) at the bottom followed by Enticho Edaga Arbi glacials, Adigrat sandstone, Agula shales, Antalo limestone and Ambaradom formation (Sembroni et al., 2017). Sekota district is located in the Tekeze River Basin (TRB), which constitutes a wide variety of rocks, ranging in age from

Neoproterozoic foundation to more recent Quaternary deposits and it is characterized by complex geological structures (Hagos et al., 2015) (Figure 3.6).

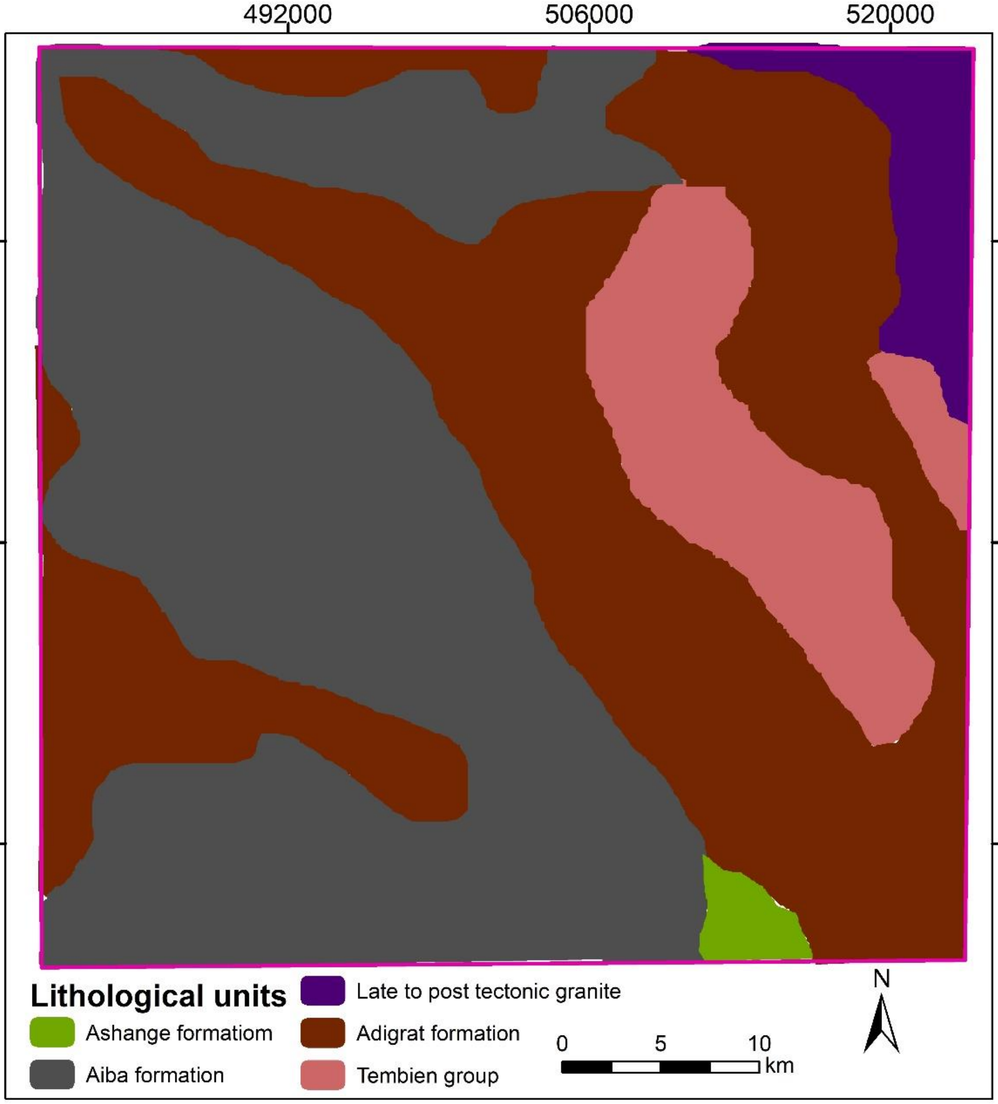

Figure 3. 6 Simplified geological map (After Hagos et al., 2015)

Out of these rocks, Mesozoic succession is dominant in our study area. The Adigrat Sandstone is a geological rock formation that is classified as Triassic to Collovian in age and was formed by fluviatile processes. Research conducted by Beyth (1973) has shown that the thickness of this sandstone varies significantly, ranging from 80 to 700 meters. The sandstone is predominantly characterized by its thick-bedded and compact nature, often exhibiting cross-bedding structures. In terms of color, it typically ranges from white or gray to red and possesses a fine to medium grain size with a well-organized particle distribution. Additionally, it is interspersed with layers of conglomerate, siltstone, shale, laterite, and occasionally carbonate bedsAdigrat sandstone is followed by Antalo Limestone, which is mostly composed of limestone, marl, and shale. Ambaradome sandstone sometimes called upper sandstone overlaid Adigrat sandstone.

Local field investigation with the Ethiopian Geological Institute small-scale geological map shows the study area is characterized by diverse geological formations including Mesozoic sedimentary and Cenozoic igneous rocks. It is a geologically under-explored area in the country except the sketch map produced by the Ethiopian Geological Institute at the scale of 1:250,000. The geological units were digitized from geological map sheets of Ifag and Maychew produced by the EGI (EGI, 2011). Ashange basalt, gray to light gray, deeply weathered flood basalt, with fine to medium texture containing minor tuffs covers about 253.18 km^2 of area, which is 29% of the study area (Figure 3.7). Lower and middle lava flows of tertiary age are dominant and cover most portions of the Western part having an approximate total area of 721.45 km^2 which accounts for 35.9% of the total area. They are stratified lower lava flows intercalated with scoria, rhyolites, and trachytic obsidian at the top part and lacustrine sediments containing coal seams at some places. Ambaradom sandstone and Adigrat sandstone have nearly the same area coverage accounting for 409 and 415 km^2 both covering 41 % of the study area. Texturally, Ambaradom sandstone is fine to coarse-grained, slightly tilted, and fractured with interbeds of conglomerates, which forms cliff topography in the study area. Adigrat sandstone is reddish and pink in color and fine-grained in texture, slightly weathered, with cross-bedded sandstone forming very high to gentle slope topography. A 209.71 km^2 area is covered by light yellowish with very fine to fine-grained limestone, intercalated with marl, horizontally layered bedding planes (Table 3.2).

Table 3. 2 Areal statistics of lithological units

Lithological units	Area	Percentage
Middle lava flow	121.21	6.03
Lower lava flow	600.24	29.87
Ashange basalt	253.18	12.60
Ambaradom sandstone	409.6	20.38
Antalo limestone	209.71	10.43
Adigrat sandstone	415.16	20.66

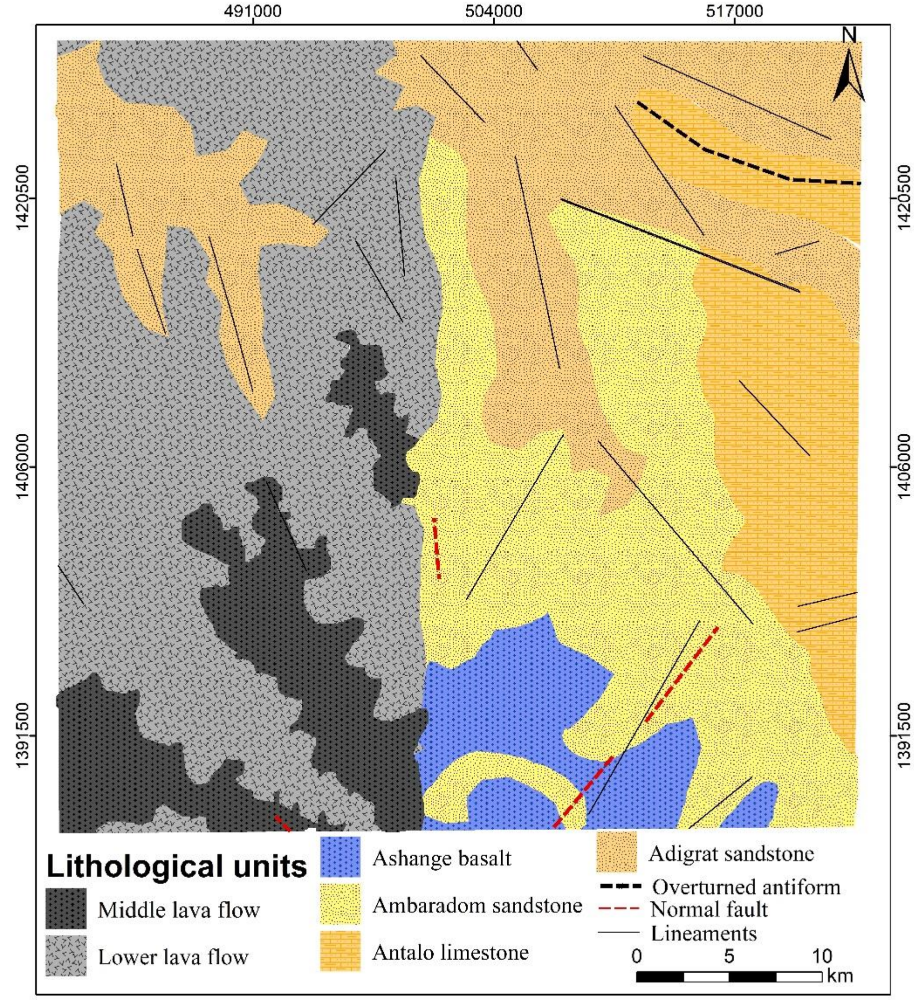

Figure 3. 7 Geological map (Source: EGI, 2012)

3.7. Data and methods

3.7.1. Data

This research has used different data including primary and secondary data from different sources. Cloud-free, ASTER level 1 data was downloaded from the National Aeronautics and Space Administration (NASA) Earth-data open access source (https://www.earthdata.nasa.gov/). ASTER is a multispectral imaging sensor on NASA's Terra satellite, launched in December 1999 by NASA, the Ministry of Economy, Trade and Industry (METI), and the Earth Remote Sensing Data Analysis Center (ERSDAC) of Japan. The ASTER L1T product is a precision terrain-corrected and sensor radiance-registered type that needs atmospheric correction to obtain surface reflectance. The study area is wide and is covered by four scenes of Sentinel–2. Manual mosaicking of these datasets in software is timeconsuming and the line of drop between scenes deteriorates data quality. As a result, the mosaicked Sentinel −2B level 2A product was exported from Google Earth Engine using code. Sentinel −2 satellite is a high-resolution multispectral imaging mission that has two identical constellations, Sentinel −2A and Sentinel 2B respectively. The ee.ImageCollection.median function in GEE was used to process and create new images from the collection of images, calculating the middle value (median) for each pixel across all matching bands within the collection to create a new image where each pixel represents the median of all corresponding pixel values in the original image collection (Appendix 5). Matching bands are identified by their names. Sentinel −2 level 2A data is surface reflectance data corrected for Rayleigh scattering that improves the effect of atmospheric gases like water vapor, carbon dioxide, and ozone. These remote sensing datasets were acquired in dry seasons to minimize the cloud effect and the coverage of surfaces by seasonal vegetation. The ASTER SWIR band was no longer used as of April 2008 due to anomalous saturation of values and anomalous striping in bands 5 through 9 caused by an increase in ASTER SWIR detector temperature. Due to this reason, an ASTER scene acquired in March−03−2008, and four Sentinel 2B data acquired from 03−02−2023 to 09−02−2023 were used in this study. Examination of metadata of the two datasets shows the cloud cover of 0.00% for ASTER and 0.00%−0.44% for Sentinel 2 data. In this research, VNIR and SWIR bands of ASTER and Sentinel 2B were utilized for remote sensing-based mapping of iron ore deposits.

In this research the geological map sheets viz. Ifag and Maychew compiled by the Ethiopian Geological Institute at the scale of 1: 250,00 were used to prepare a litho-structural map of the area. Geochemical analysis data obtained from the Ethiopian Ministry of Mines, Geological Institute Department was used to identify the type of iron ore mineralization. Iron occurrence maps (shapefiles) prepared in coordination with the Ethiopian Geological Institute and the private Access Capital Services Group have been used as supplementary for the evaluation of digital image processing techniques used for the detection of iron mineralization. A detailed field investigation was conducted to take samples from exposed iron blocks. Primary X-ray diffraction analysis was conducted for 10 samples taken from known iron surface exposures to validate and know the type of dominant iron deposits mineralogy phase in the area. Ten-meter resolution land uses land cover data of Sentinel2 produced by Impact Observatory in collaboration with ERSI and Microsoft was used in this study to see vegetation cover in the study area. Garmin global positioning system (GPS) has been also used to geo-locate sampling locations, and contacts between lithologies and visible geological structures. Environment for visualization of images (ENVI 5.3) and ArcGIS 10.8 version software packages were used for image processing and layout preparation respectively (Table 3.3).

Table 3. 3 Data and sources of data used

Data	Date of acquisition	Source
ASTER L1T	5-Mar-2008	https://www.earthdata.nasa.gov/
Sentinel 2B L2A	(2-9)-Feb-2023	European Union/ESA/Copernicus
SRTM DEM	9-Sep-2014	https://earthexplorer.usgs.gov/

Primary and existing data

Data	Source	Purpose
Geological map and existing iron ore map	Ethiopian Geological Institute (EGI)	For preparation of geological map and validation of remote sensing-based techniques
Geochemical analysis data	Ethiopian Geological Institute (EGI)	For identification of the type of iron ore mineral and verification of satellite-based techniques
X-ray analysis data	Analyzed in AAU, chemistry laboratory	For identification of the main iron ore mineral type and validation
Meteorological data	Climate Engine.org	For characterization of climatic condition
Land use land cover data	ESRI LULC	To see vegetation cover
Boundary shapefiles	Space Science & Geospatial Institute of Ethiopia (SSGIE)	For study area preparation

3.7.2. Methods

3.7.2.1. Data preprocessing

Radiometric and atmospheric correction was applied to ASTER L1T to retrieve surface reflectance and was resampled to the finest spatial resolution of 15 m. Sentinel−2 MSI level 2-A data are cloud-masked orthorectified top-of-atmosphere reflectance images as stated in the Sentinel 2 MSI product user handbook (ESA, 2015). Sentinel−2 MSI data has 13 bands in different spatial resolutions and all bands were resampled to the finest resolution (10m) while exporting the dataset from Google Earth Engine (GEE). The spatial and spectral sensitivity of the Sentinel −2 MSI sensor was summarized in (Table 3.4). ASTER L1T data is SWIR cross-talk corrected, radio-metrically and geometrically calibrated which has 3 bands in VNIR, 6 bands in SWIR, and 5 bands in TIR region (Table 3.5). For retrieval of surface reflectance, first, the VNIR and SWIR bands were radio-metrically corrected, resampled to 15-meter spatial resolution, and layer stacked. After the layer stacking, the atmospheric correction technique, FLASH (Fast Line-of-sight Atmospheric Analysis of Spectral Hypercubes) was applied in ENVI 5.3 software. FLAASH can correct wavelengths up to 3 µm in the visible, near-infrared, and shortwave infrared regions using first-principles atmospheric correction (Isaacs et al., 1987). Most hyperspectral and multispectral sensors are compatible with FLAASH. The ASTER first 9 bands were used in this study that encompasses 0.52−2.43 µm wavelength range and Sentinel−2 12 bands except band 10 which was designed for cirrus study. Sentinel bands encompass the 442.2−2185 nm wavelength range which is below the maximum limit (3 µm) of FLAASH.

Normalized Difference Vegetation Index (NDVI) was calculated for both ASTER and Sentinel 2 using equation 1 (Rouse et al., 1974).

$$\text{NDVI} = \frac{NIR-Red}{NIR+Red} \qquad (1)$$

In the case of Sentinel-2, the NIR band and red band correspond to band 8 and band 4 respectively whereas for ASTER the NIR band is represented by band 4 and the red band by band 2. Areas having NDVI values greater than 0.3 are considered vegetation and masked out from analysis. Masking of highly vegetated areas avoids misinterpretation that the spectral response of vegetation is similar in red bands of the electromagnetic spectrum.

Table 3. 4 Spectral and spatial performance characteristics of Sentinel 2B sensor

Bands	Central wavelength (nm)	Bandwidth (nm)	Spatial resolution (m)
Band 1 – coastal aerosol	442.2	21	60
Band 2 – blue	492.1	66	10
Band 3 – green	559	36	10
Band 4 – red	664.9	31	10
Band 5 – vegetation red edge	703.8	16	20
Band 6 – vegetation red edge	739.1	15	20
Band 7 – vegetation red edge	779.7	20	20
Band 8 – NIR	832.9	106	10
Band 8A – Narrow NIR	864	22	20
Band 9 – water vapor	943.2	21	60
Band 10 – SWIR – cirrus	1376.9	30	60
Band 11 – SWIR	1610.4	94	20
Band 12 – SWIR	2185.7	185	20

Table 3. 5 Spectral and spatial performance characteristics of ASTER sensor

Band	Spectral range (µm)	Spatial Resolution (m)	Band Explanation/Uses
1	0.52 - 0.60	15	Visible and Near-Infrared
2	0.63 - 0.69	15	Visible and Near-Infrared
3N	0.78 - 0.86	15	Visible and Near-Infrared
3B	0.78 - 0.86	15	Visible and Near-Infrared
4	1.60 - 1.700	30	Shortwave Infrared
5	2.145 - 2.185	30	Shortwave Infrared
6	2.185 - 2.225	30	Shortwave Infrared
7	2.235 - 2.285	30	Shortwave Infrared
8	2.295 - 2.365	30	Shortwave Infrared
9	2.360 - 2.430	30	Shortwave Infrared
10	8.125 - 8.475	90	Thermal Infrared
11	8.475 - 8.825	90	Thermal Infrared
12	8.925 - 9.275	90	Thermal Infrared
13	10.25 - 10.95	90	Thermal Infrared
14	10.95 - 11.65	90	Thermal Infrared

Source:https://lpdaac.usgs.gov/data/get-started-data/collection-overview/missions/asteroverview/

3.7.2.2. Band ratio

Band ratios are simple and effective methods in the detection and mapping of iron mineralization due to iron minerals' characteristic reflectance and absorption properties concerning different VNIR and SWIR wavelength positions in the electromagnetic spectrum. Iron mineralization mainly occurs in the two ore forms namely hematite (Fe_2O_3) and magnetite (Fe_3O_4). Other forms of iron ore that occur in nature include but are not limited to goethite (FeO2H), Jarosite (KFe_3 $(SO4)_2(OH)_6$), and limonite ($FeO(OH)\cdot nH_2O$). Hematite iron ore belongs to ferric iron oxide (Fe^{+3}) and exhibits very similar characteristics with other iron ores except magnetite in spectral response in the VNIR region of the electromagnetic spectrum (Figure 3.8). A detailed examination of the spectral response of these minerals shows that all forms of iron mineralization highly reflect the red band and absorb the blue bands of the VNIR region respectively can be effectively mapped using Sentinel 2 band ratio (b4/b2) (Van der Werff & Van der Meer, 2016). They have also characteristic absorption near 860 nm and 530 nm, and reflectance peaks near to red band and 750−760 nm (Fraeman et al., 2020). Depending on these characteristics, analogous sentinel 2 band ratios similar to band ratios of ASTER and Landsat 5 TM proposed by Sabins, (1999) were used for mapping ferric oxides (hematite type) and lateritic type iron ore mineralization. ASTER band2/band1 and ASTER b4/b5 band ratios have been widely and effectively used for mapping hematite-type iron ores (ferric-oxides) and lateritic-rich iron bearing zones respectively (Abay et al., 2022; Gopinathan et al., 2020; Shebl et al., 2023). Sentinel 2 MSI band4/band2 and band b11/b12 are analogues to ASTER b2/b1 and b4/b5 respectively and both ASTER and Sentinel band ratios were used for mapping hematite and lateritic iron mineralized zones in this study.

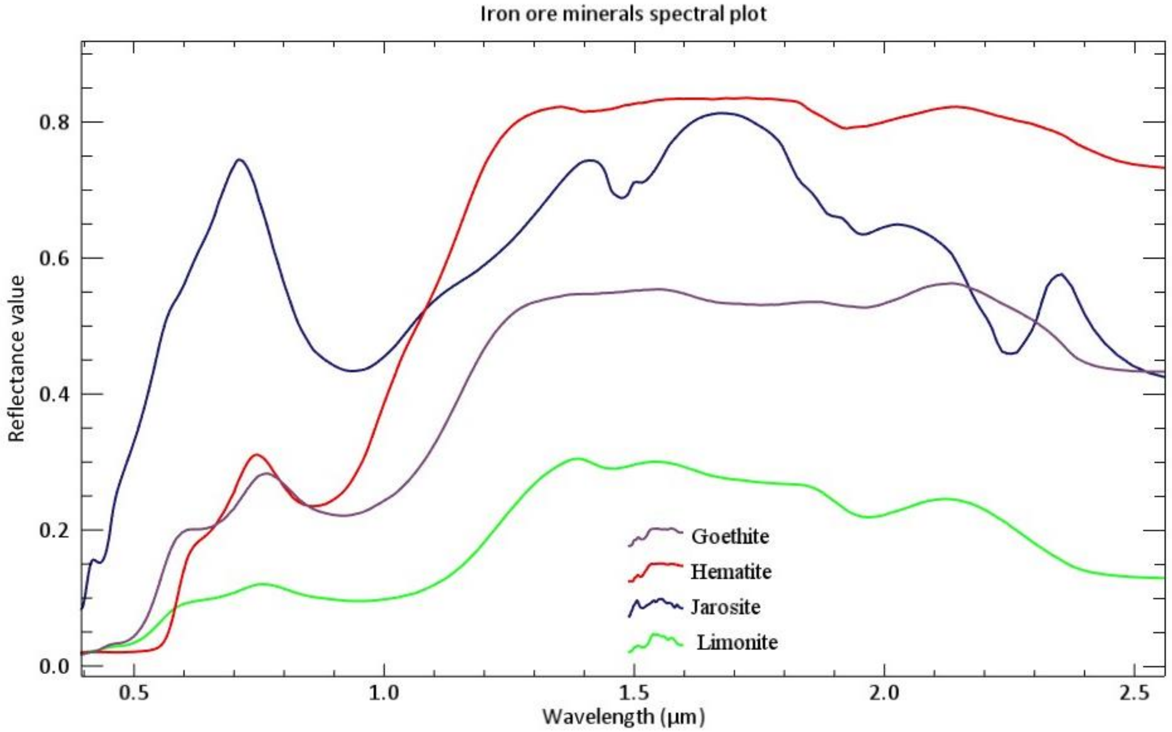

Figure 3. 8 USGS iron ore minerals spectral plot

3.7.2.3. Feature-oriented principal component analysis

The principal component analysis creates smaller uncorrelated datasets by removing the redundancy of spectral information in multiband datasets. Feature-oriented principal component analysis method evaluates the contribution of original bands to each principal component to select an effective principal component based on spectral responses of materials to different bands (Ghoneim et al., 2022; Traore et al., 2020). It is known that iron minerals highly reflect the red band and absorb the blue band in the electromagnetic spectrum. Through the analysis of the spectral signatures of the hematite-type iron mineralization, they have distinctive absorption at 490nm (b2), 860nm (b5), and 945nm (b10) of Sentinel 2 (El Kati et al., 2018; Van der Werff & Van der Meer, 2015). As mentioned above iron-bearing minerals also show reflective peaks/features near 0.72 μm and 0.74 μm which falls at band 6 of Sentinel 2. As a result, 1, 2, 3, and 4 bands of ASTER and b2, b4, b7, and b8a bands of Sentinel 2 were used in the principal component transformation process. The produced principal components (PCs) were evaluated based on eigenvector statistics. The selection of a diagnostic PCA for a certain iron mineral detection depends on eigenvalue loadings to determine the component that has spectral information of the intended mineral.

3.7.2.4. Endmember collection

ENVI software provides various methods for automatic endmember collection, including Spectral Hourglass and SMACC (Sequential Maximum Angle Convex Cone) (Gruninger et al., 2004). Spectral hourglass adopts a geometric approach based on simplex hulls to progressively isolate pure endmembers, while SMACC iteratively identifies endmembers based on their angular relationship with an existing cone. In this research, Endmember was collected automatically from both datasets using ENVI hourglass wizard. The process typically involves four key steps: Minimum Noise Fraction (MNF) transformation, pure pixel calculation, n-dimensional visualization and finally retrieving end members from images. MNF requires surface reflectance data. MNF transformation plays a vital role in determining inherent data dimensionality and enhancing data quality by separating noise from the data. Endmembers should be pure pixels representing a certain feature in the pixel. But, in most cases, pixels contain a linear mixture of different spectral signatures. Pixel purity index (PPI) calculation was used to find spectrally pure or extreme pixels in the images. The minimum and maximum iteration values in the ENVI PPI calculation are 50000 and 32, 767 respectively. In this research, 10000 PPI iterations and the threshold value of 2.5 was used. For manual extraction of endmembers from PPI, the extreme corners/edges are selected on the N-D visualization plot and exported. Automatic ENVI hourglass wizard which retrieves distinctive endmembers is used in this study. To select representative endmembers of iron ore mineral (hematite) spectral plots of endmembers were compared with resampled USGS mineral spectral library using the spectral feature fitting technique. 10 members were collected from images. These endmembers were compared with common iron ore minerals (hematite, goethite, and jarosite) spectra from the USGS spectral library.

3.7.2.5. Mixture-tuned matched filtering (MTMF)

Mapping specific mineral abundance from mixed spectral signatures presents a challenge for traditional pixel-level techniques like band ratios and PCA. In such scenarios, sub-pixel level mapping techniques, such as Mixture-Tuned Matched Filtering (MTMF), linear spectral unmixing, and Spectral Angle Mapper (SAM), become crucial. These techniques offer the ability to map the abundance of specific minerals within a pixel, even when their spectral signatures are mixed with others. Numerous researchers have employed these techniques, requiring prior knowledge of the target material's end members (Abay et al., 2022; Yousefi et al., 2018). By enhancing the spectral and spatial resolution of the images, the MTMF detects the abundance of a certain endmember in the pixel or images (Routh et al., 2018). It uses end-members collected from an image or reference spectrum to map the abundance of targets in an image. It produces matched filtering and infeasibility results for each end member. The floating-point value of the match represents how much the areas in the image resemble the end member. The match score is used to identify the abundance of a certain target, a high match score indicates a high resemblance/match with the member selected. The infeasibility result shows the correctness of MF in which a low infeasibility result indicates accurate abundance mapping of the end-members from the image. The detailed workflow of methods and techniques employed in this research are portrayed in the flowchart diagram (Figure 3.9).

3.7.2.6. Linear spectral unmixing

In this study, LSU is applied to ASTER and Sentinel 2 surface reflectance data for mapping the abundance of iron mineralization (hematite) at the sub-pixel level. Reflectance/radiance values of pixels of images contain a linear combination of different spectral signatures (Roberts et al., 2012). To map the abundance of each end-member in the pixel, the spectral unmixing technique was applied. Endmembers were collected from both images using ENVI’s spectral hourglass wizard. The number of end members to be collected should be not more than the number of bands of the sensor (ENVI, n.d). LSU utilizes the spectral properties of the endmembers and calculates the relative abundance of endmembers inside a pixel (Pour et al., 2023). The 9 bands of ASTER and 12 bands of Sentinel 2 were used in this study.

3.7.2.8. Anomaly areas (Fe-potential) delineation

To discriminate potential areas from transformed images using the techniques described above, thresholding techniques were applied. Thresholding is a statistical technique that allows to determine the quantitative information about the abundance of the target mineral. It is calculated using mean and standard deviation obtained from basic statistics values of transformed data using equation (2).

$$\text{Threshold value} = \text{Mean } (\bar{x}) + (\text{Z} - \text{score} * \text{Standard deviation}) \tag{2}$$

where the Z score is determined based on the confidence level of mapping. For instance, if the confidence level is 95%, 90% and 80% the respective Z-score is 1.96, 1.64, and 1.28, respectively.

3.7.2.9. Field survey, sampling, X-ray diffraction, and geochemical analysis

Field investigation has been conducted to identify different lithologies, and geological structures and take samples from exposed iron blocks. Due to accessibility problems, all of the iron occurrence blocks were not addressed. Sampling locations and contacts were accurately geographically located with Garmin's global positioning system (GPS). Samples taken from surface iron blocks (a total of 10 samples) were analyzed with X-ray diffraction at Addis Ababa University, chemistry department lab. Secondary geochemical analysis of major oxides including iron oxides conducted by the Ethiopian Geological Institute was also used to validate results obtained using remote sensing techniques.

3.7.2.10. Comparison, correlation, and validation of results

Correlation analysis of the results of different digital image processing techniques with ASTER and Sentinel 2 was done to explore the relationship and effectiveness of the techniques employed. The Pearson correlation coefficient was applied to identify the pattern and to explore the relationship between remote sensing-based techniques used in this study. To compute the correlation between techniques, random 1500 points were generated using the fishnet tool in ArcGIS. The Pearson correlation coefficient is a statistical measure used to quantify the strength and direction of a linear relationship between two continuous variables. Its values range from -1 to 1 and are interpreted as perfect negative and perfect positive correlation. A stronger correlation is shown by values closer to 1 or -1, whilst a weaker relationship is indicated by values closer to 0. The performance of remote sensing-based techniques with ASTER and Sentinel 2 data was evaluated using shapefiles, primary XRD analysis of the collected samples, and geochemical analysis data. Existing iron ore occurrence polygons were also used to validate techniques employed for mapping iron ore mineralized zones. Software packages used in this study were ENVI 5.3 version (Environment for visualization of images) for digital processing of remotely sensed data, Match 3! For mineral phase identification of powder diffraction data and ArcGIS 10.8 for layout preparation (Table 3.6)

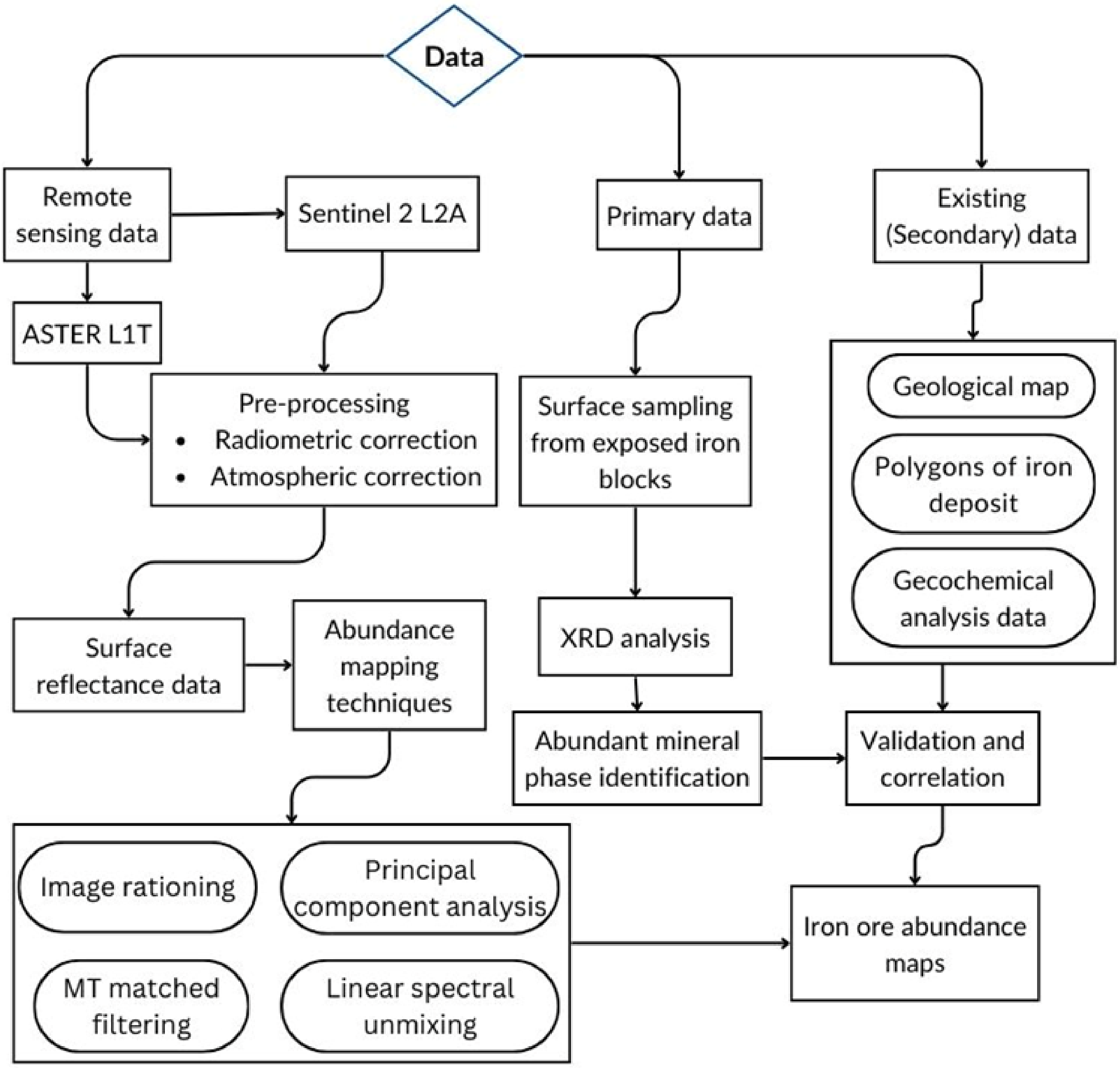

Figure 3. 9 Detailed methods flow chart

Table 3. 6 List of software used

Software	Purpose
Environment for Visualization of Images (ENVI 5.3)	Image processing and analysis
ArcGIS 10.8	Layout preparation
Global mapper 20	For gridding digital elevation model
Surfer 16	Physiographic map preparation
Match 3!	XRD analysis and mineral phase identification

CHAPTER FOUR

4. RESULTS

4.1. Vegetation and vegetation masking

The Normalized Difference Vegetation Index (NDVI) derived from Sentinel 2 and ASTER to map vegetation cover intensity range from –0.12−0.65 and −0.09−0.53 respectively (Figure 4.1 and Figure 4.2). Highly vegetated areas are shown in green color patches. They are high in high-altitude areas, especially at the eastern and southern ends. NDVI values greater than 0.3 in both sensor data are considered vegetated areas and masked out. The areal coverage of masked surfaces with NDVI values greater than 0.3 for ASTER data are 15 km^2 and 22 km^2 for the Sentinel 2 dataset respectively.

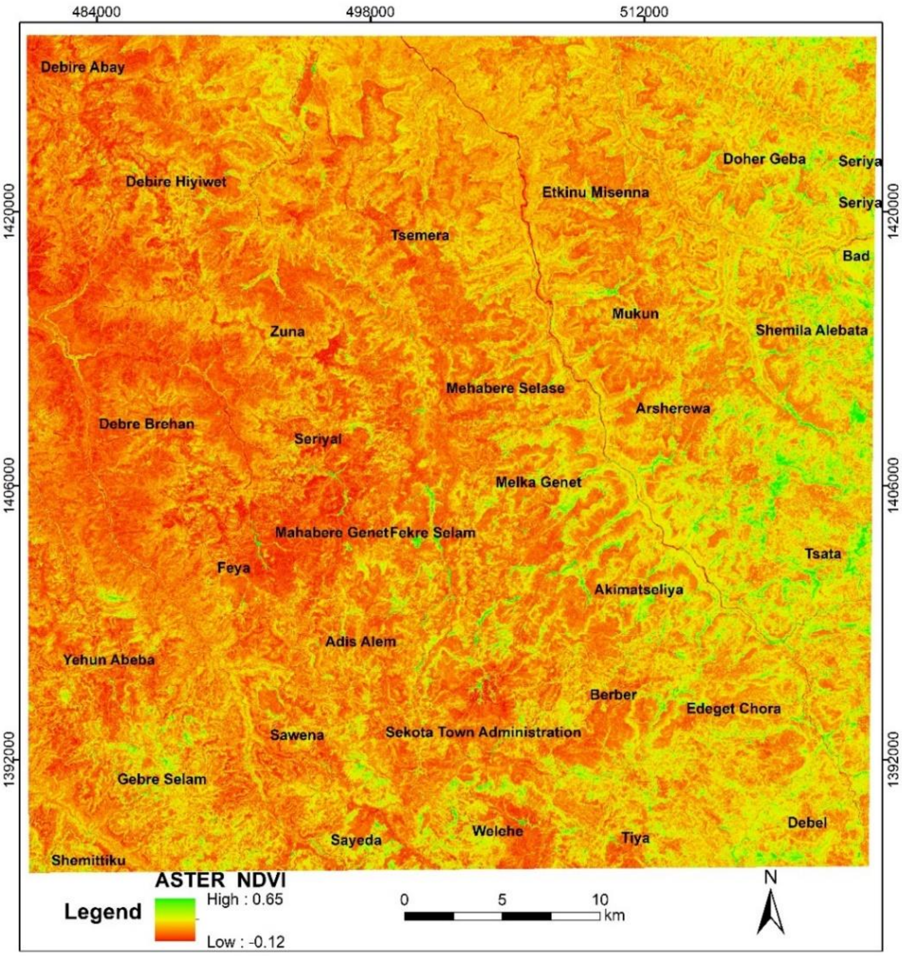

Figure 4. 1 NDVI map from ASTER

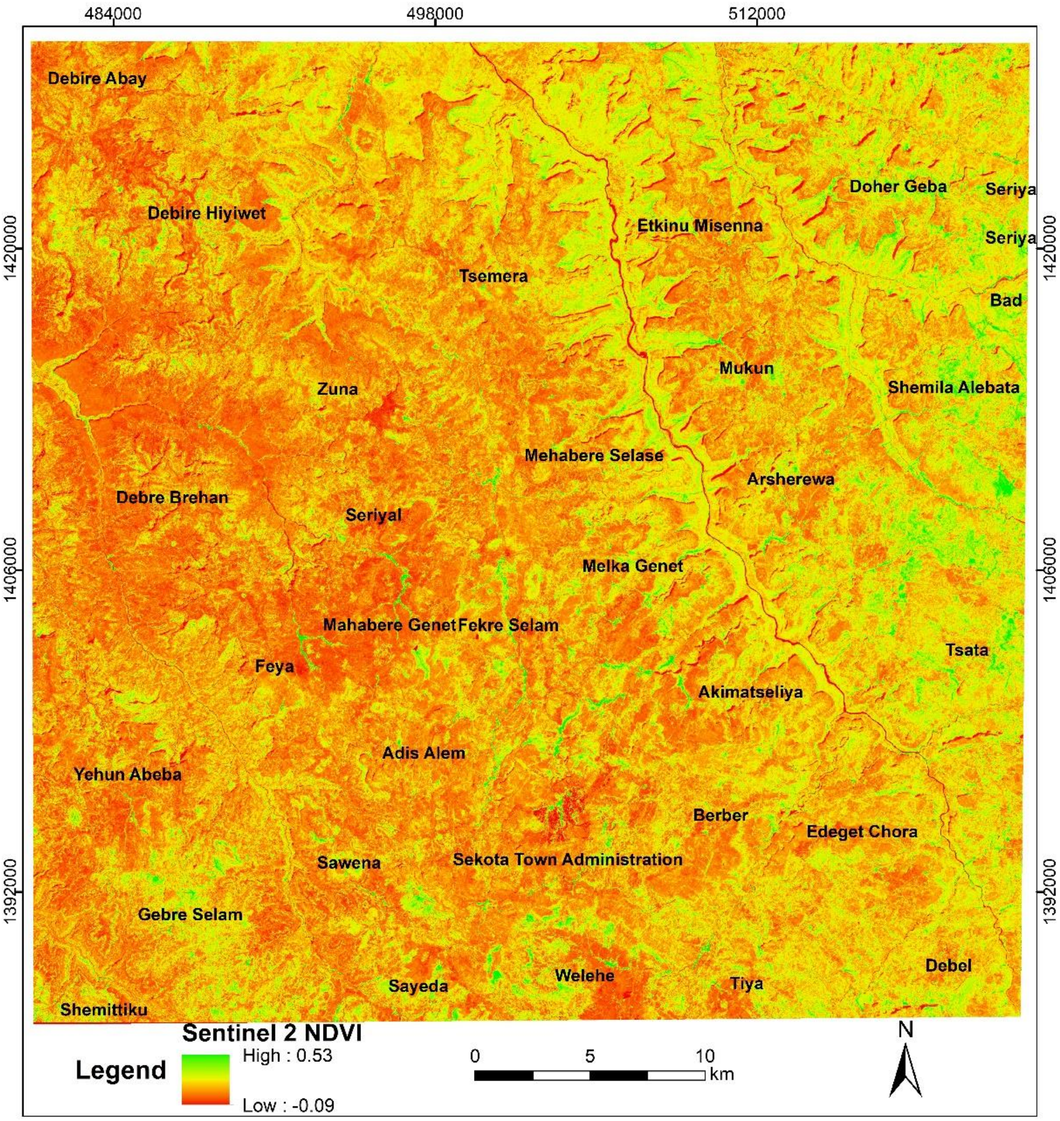

Figure 4. 2 NDVI map from Sentinel 2

The spectral response characteristics of vegetation and iron ore minerals exhibit high reflectance in the red edge, which is challenging for the detection of iron minerals from surface reflectance, particularly with iron band ratios. The areas with higher NDVI values (more than 0.3) were masked out from the analysis to avoid misinterpretations. The masked portions of images in both satellite datasets are very small. The areas having NDVI values greater than 0.3 accounts for a very small area cover (22 km^2 for Sentinel 2) which is 1.09% of the study area.

4.2. Iron mineralization abundance

4.2.1. Band ratios

The ASTER ASB/B1 and analogous Sentinel 2 S2B4/B2 band ratio delineated the distribution of hematite iron mineralized zones (ferric oxides) (Figure 4.3 and Figure 4.4) and ASTER ASB4/B5 and analogous Sentinel 2 S2B11/B12 band ratios detected lateritic iron mineralization in different locations of the study area. The abundance mapping used thresholding of fractional images of both band ratios at the confidence level of 95%.

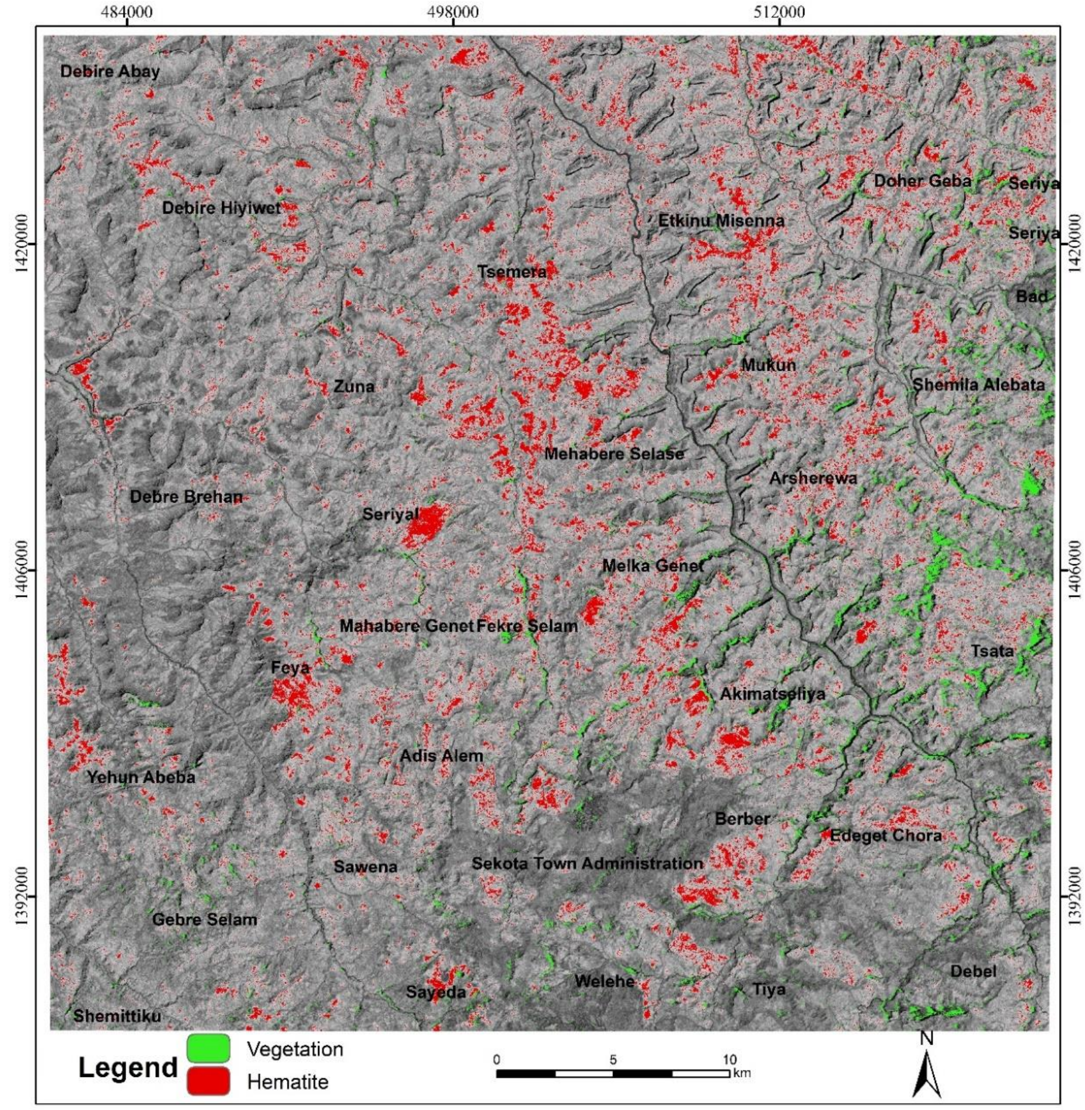

Figure 4. 3 Hematite abundance distribution map from ASTER band b2/b1 ratio.

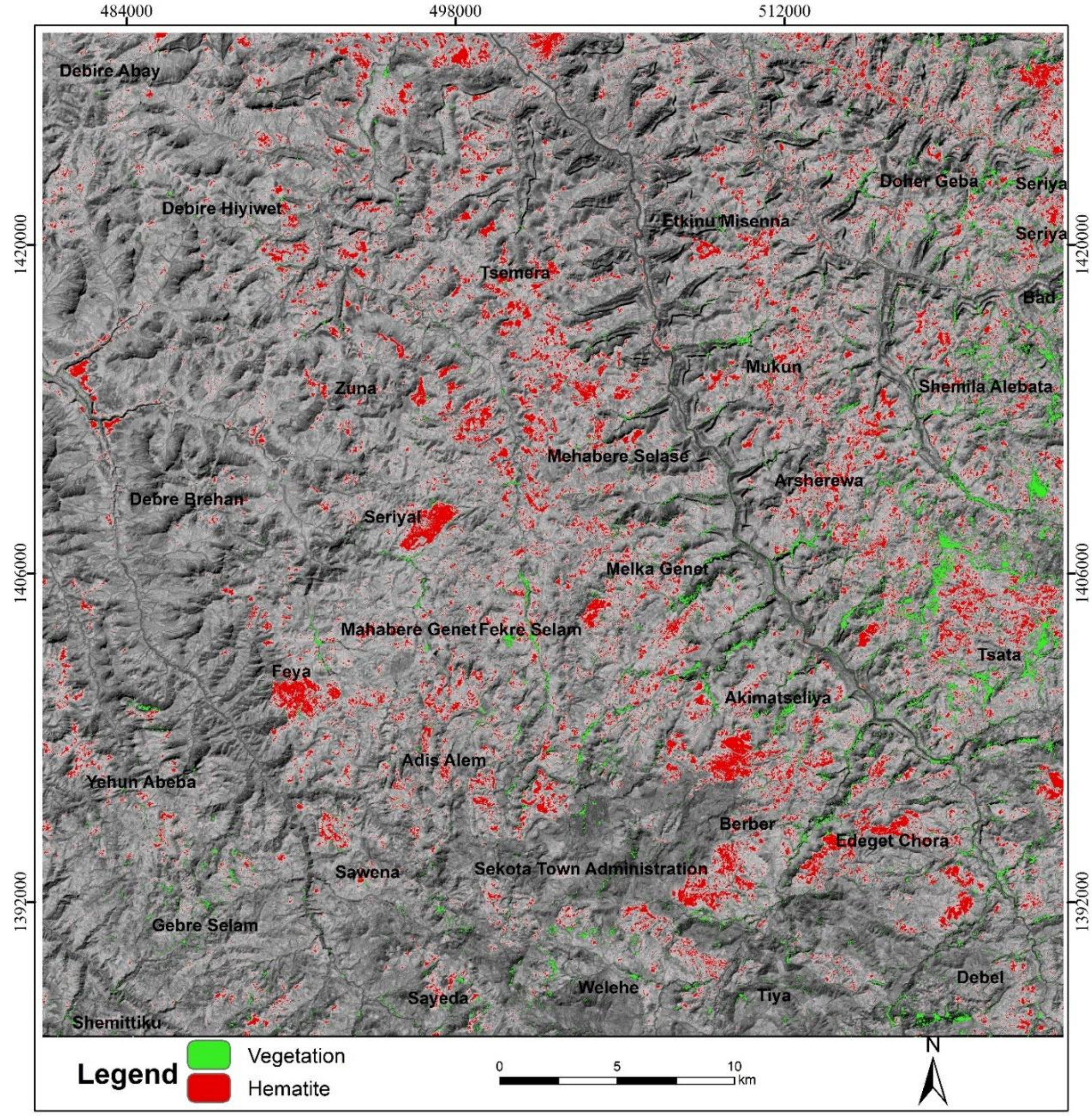

Figure 4. 4 Hematite abundance map from S2B4/B2 band ratio

The ASB2/B1 band ratio ranges from 0.70−1.72 and S2B4/B2 ratio ranges from 0.78−1.61 (Appendix 4). Threshold values of 1.35 and 1.23 were used for ASB2/B1 and S2B4/B2 band ratios respectively to delineate hematite anomalies. Hematite mineralized zones derived from band ratios of ASB2/B1 and S2B4/B2 cover an area of 102.5 and 97.68 km^2 respectively. The hematite abundance map delineated was draped over respective stretched band ratio fractional images of both sensors. High hematite mineralization was detected in the Southeast of Sekota town administration at Akimatseliya (known as Akma Yehonnes iron block), near North of Ediget Chora, at Berber, and in between Tsemera and Mahibere Selase. High hematite mineralization is also located at Seriyal (Known as the Sirrel iron block), at Feya area, Arsherewa, Mukun, Etkinu Missena, and Debire Hiywet area. S2B11/B12) and ASB4/B5) detected lateritic iron mineralization at gorges of rivers and valley slopes. Additionally, lateritic mineralization detected in the North of the Tsemera and Tsata area.

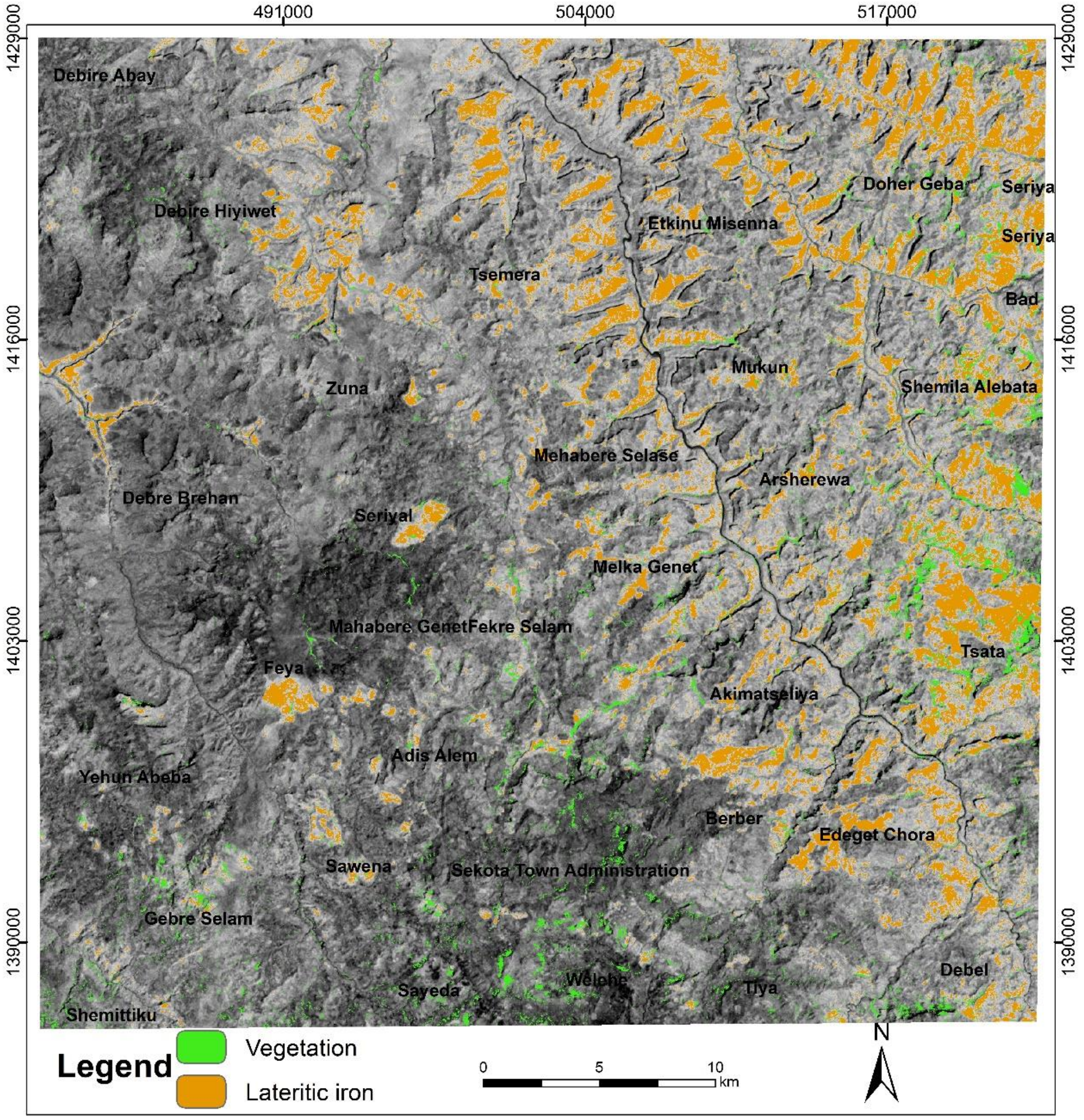

Figure 4. 5 Lateritic iron mineralization abundance from ASB4/B5

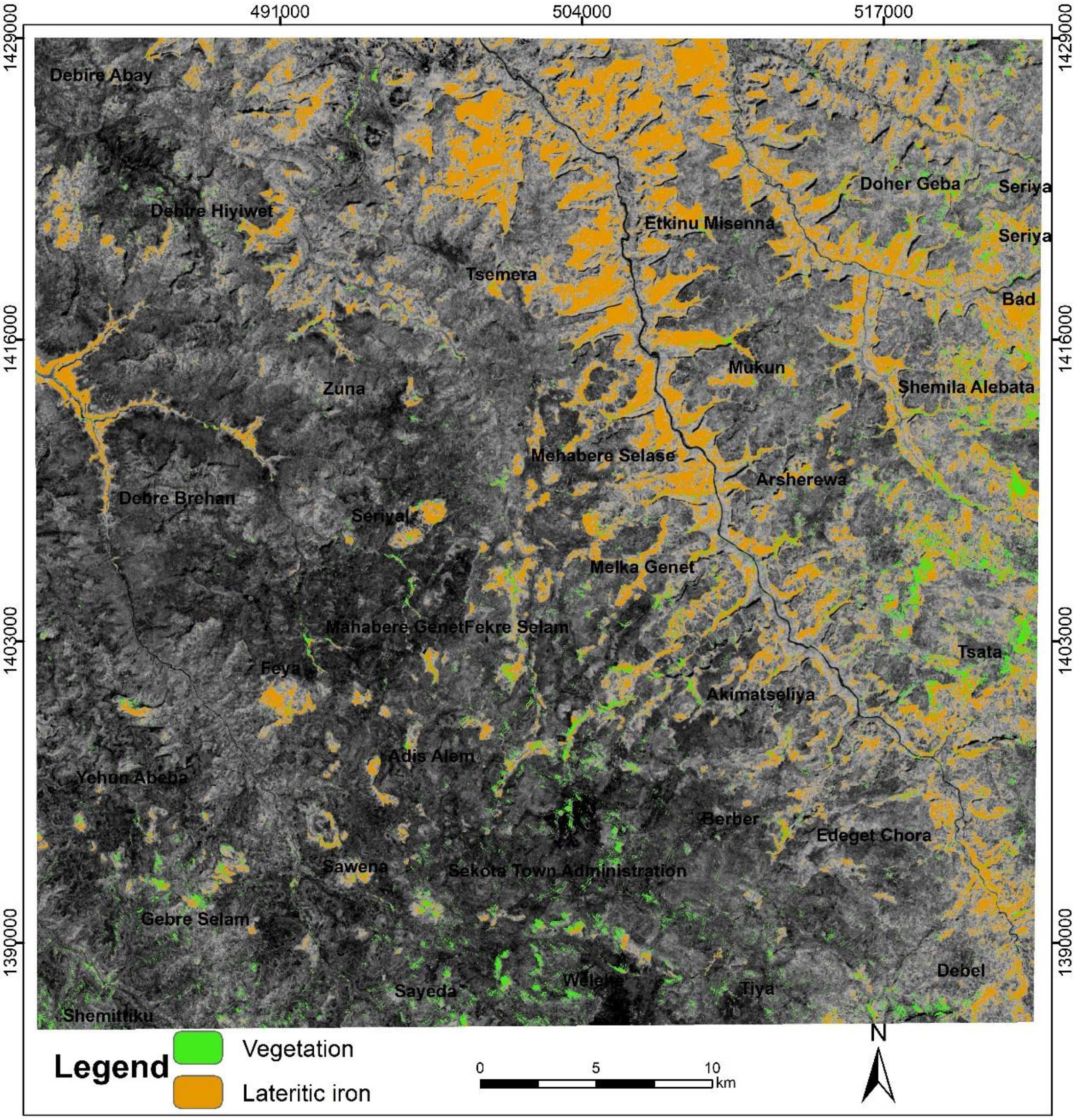

Figure 4. 6 Lateritic iron abundance map from Sentinel 2 band ratio b11/b12

Anomaly of lateritic mineralization distribution was quantified from band ratio maps generated from ASB4/B5 and S2B11/B12 which range from 0.73−2.08 and 0.97−1.63 respectively. Lateritic anomaly areas were delineated using a threshold value of 1.29 for the S2B11/B12 and 1.54 for the ASB4/B5 band ratio. The areal coverage of lateritic mineralization detected from S2B11/B12 ratio is 168.13 km^2 and that of ASB4/B5 is about 138.46 km^2. The threshold value used for determining iron mineralization anomalies area is the submission of mean and standard deviation found from basic statistics of band ratio results. The confidence level of mapping the abundance of iron mineralization is 95% for both hematite and lateritic mineralization mapping.

4.3. Feature-oriented principal component analysis

Analysis of spectral plots of hematite minerals from the USGS spectral library shows distinctive reflectance and absorption properties at specific wavelength ranges which coincides with different bands of satellite images. All spectral plots of hematite mineral have characteristic reflectance at 0.66−0.78 µm wavelength range and absorption at 0.400−0.545 µm and 0.828−0.894 µm wavelength ranges. This reflexive wavelength range coincides with the red band (band 2) of ASTER, and band 4 of Sentinel 2 respectively. The absorption wavelength range of 0.400−0.545 µm of hematite coincides with the blue bands (band 1 for ASTER and band 2 of Sentinel 2) of both satellite sensors. The PC 4 selected from generated PCA using the first four bands of ASTER and PC 3 of Sentinel 2 generated using b2, b4, b7, and b8a has similar information in the detection of hematite mineralization. PC that has information used to detect hematite iron mineralization is evaluated based on eigenvector loadings. The eigenvector loadings of four principal components (PCs) of both sensors calculated were evaluated (Table 4. 1 and Table 4.2). Eigenvector loadings ASTER PCA1 show positive loadings in all bands. This PC has no information about iron minerals. The ASTER PC2 has also positive loadings for the first three bands and negative values at band 4. This component also doesn't contain iron mineral reflectance and absorption characteristics. The ASTER PC3 has negative loadings except for band 3. This principal component also doesn't have iron minerals reflectance and absorption characteristics because it has similar eigenvector loadings in both reflectance and absorption bands. The ASTER PC4 contains contrasting eigenvector values, extreme negative eigenvector values in the absorption band (band 1), and extreme positive values in the reflectance band (band 2) of ASTER. At band 3 it has also a positive eigenvector value though it is very small and its contribution to be seen as a bright pixel is negligible. If the eigenvalue is positive at the reflexive band and negative at the absorption band the intended target is shown as bright pixels. If the eigenvalue is positive in the absorption band and negative in the reflexive band the target is highlighted as dark pixels. Consequently, hematite mineralized zones are seen as bright pixels in the PC4 image (Appendix 4). Thresholding was used to quantify the abundance of hematite mineralization at a 95% confidence level. PC4 of ASTER fractional image ranges from -81.15−42.56 and threshold value 6.99 is used in delineating hematite abundance. The hematite mineralization zones delineated from ASTER PC4 cover an area of 133.40 km^2.

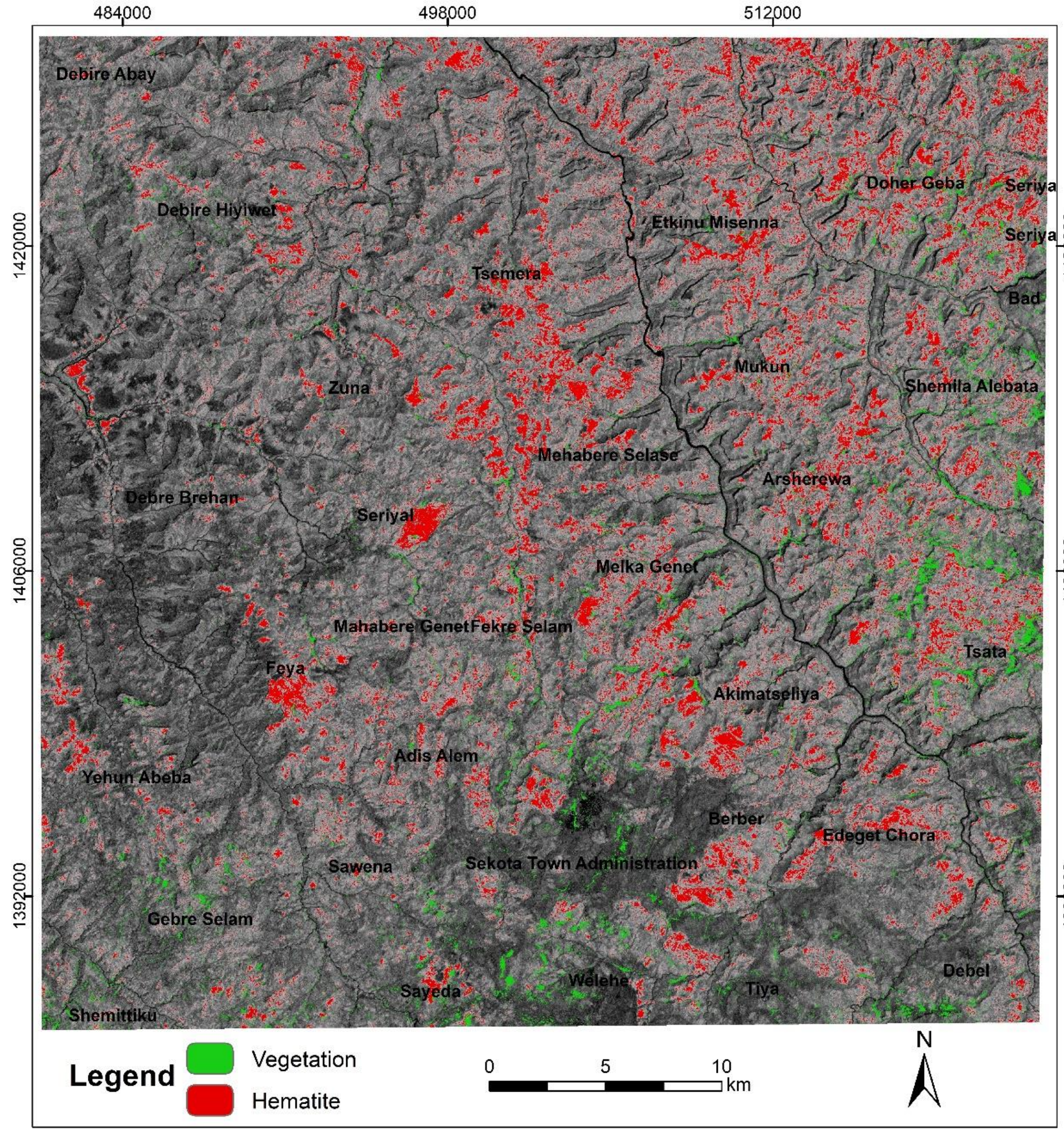

Figure 4. 7 Hematite iron abundance map from ASTER PC4

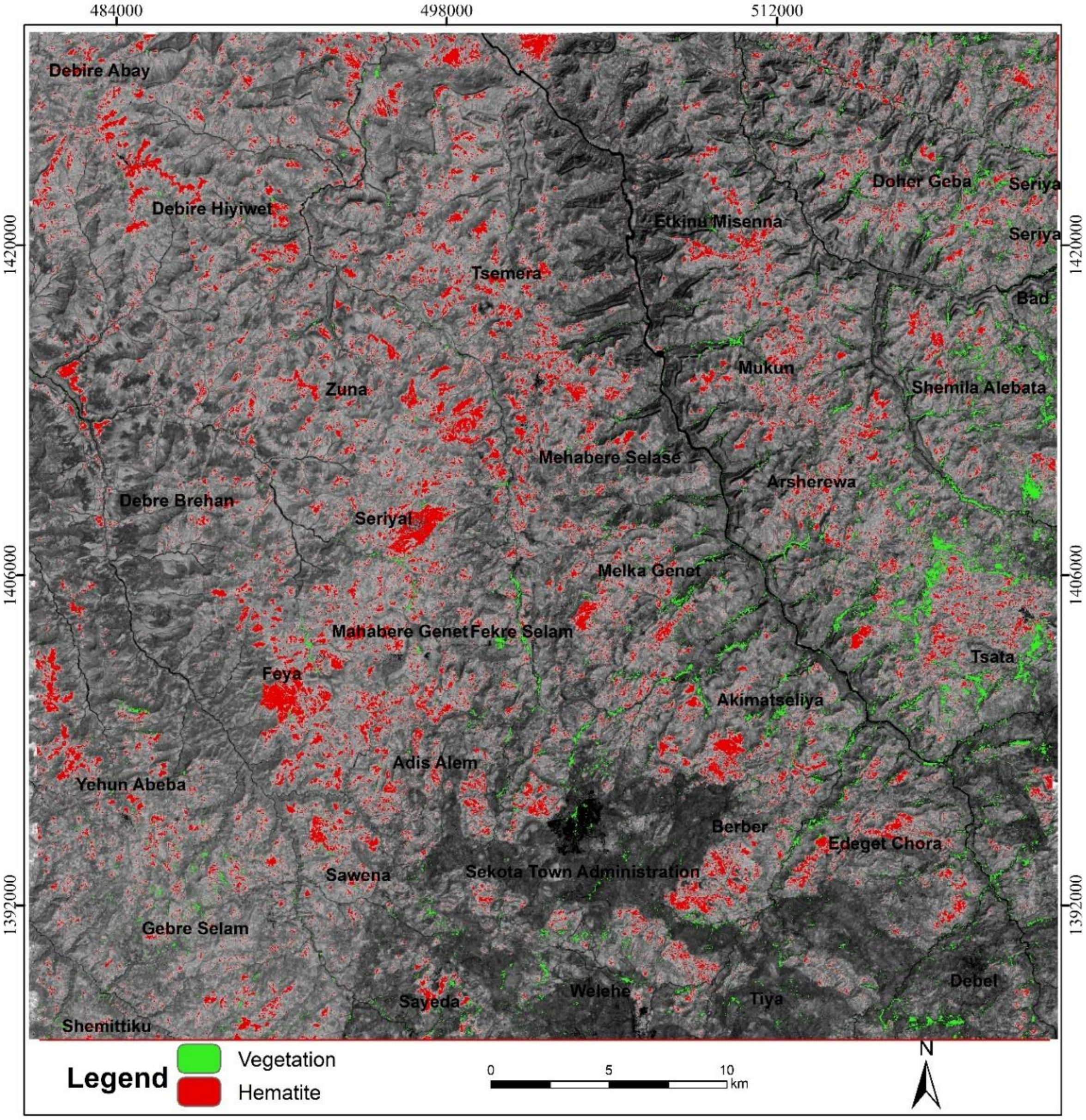

Figure 4. 8 Hematite abundance map from PC3 of Sentinel 2

Table 4. 1 Eigenvector loadings of principal components (PCs) generated from ASTER bands

Eigenvectors	Band 1	Band 2	Band 3	Band 4
PC1	0.34	0.44	0.59	0.58
PC2	0.25	0.32	0.42	−0.81
PC3	−0.36	−0.63	0.69	−0.004
PC4	−0.83	0.55	0.07	−0.002

Table 4. 2 Eigenvector loadings (values) of PCs generated from Sentinel 2 bands

Eigenvectors	band 2	band 4	band 7	band 8a
PC1	−0.23	−0.43	−0.59	−0.65
PC2	−0.38	−0.77	0.22	0.46
PC3	−0.89	0.44	0.04	−0.02
PC4	0.02	0.13	−0.78	0.61

Localities of Feya, Sirrel, the area between Tsemera and Mehebere Selase, below Berber and Akemetseliya, and between river gorges in the Debre Birhan area have a high abundance of iron mineralization. Similarly, the PC3 of PCA generated from Sentinel 2 bands b2, b4, b7, and b8a has demarcated hematite mineralized zones (Figure 4.8). Bright pixels in the PC3 show hematite ore deposits. The selection of principal components is done using loadings of eigenvectors of each PC's contribution to each band. The Sentinel 2 PC1 has nearly similar negative loadings concerning each band. It doesn't contain iron minerals reflectance and absorption features. The Sentinel 2 PC2 has negative loadings both in reflexive and absorptive bands of Sentinel 2 and it doesn't contain information used to map iron minerals. The PC3 contains opposing eigenvector values in band 2 and band 4 of Sentinel 2. Eigenvalues show negative in band 2 (absorptive band) and high positive loading in band 4 (high reflective band). The contribution of other bands to be seen as bright pixels is negligible. It has iron absorption and reflective feature and hematite mineralization is seen as a bright pixel in PC3. The PC3 of Sentinel 2 fractional image ranges from -847.79−742.87 and the threshold value of 171.65 is used to map the distribution of hematite abundance. Hematite mineralized zones extracted from PC3 of Sentinel 2 cover an area of about 110.70 km^2.

4.4. Sub-pixel abundance mapping

4.4.1. Endmember collected

The spectral plot of 10 endmembers from ASTER and Sentinel 2 images were collected (Figure 9) and one endmember was selected as representative of iron mineralized zones (hematite mineralization). The endmember collection procedure has resulted in minimum noise fraction (MNF) transform, pixel purity index (PPI) calculation, and n-d visualization of PPI. The MNF transformation segregated spectral bands in an image that had valuable information from spectral bands that were dominated by noise (Figure 4.9). Eigenvalues of ASTER MNF components show nearly similar values except for the first 6 components out of 10 MNF components and Sentinel

MNF eigenvalues have variable values except for the last four components/bands (Table 4.3). Pure pixels were identified in a scattered form calculated at 10,000 iterations over all pixels and then visualized with n-d visualization. Spectral analysis of endmembers selected for iron mineralized zones with resampled USGS hematite, goethite, and jarosite minerals has high spectral fitting (Figure 4.10). SFF match between the endmember spectra and USGS iron minerals) resampled spectra (hematite, goethite, and jarosite show a good correlation (Table 4.4).

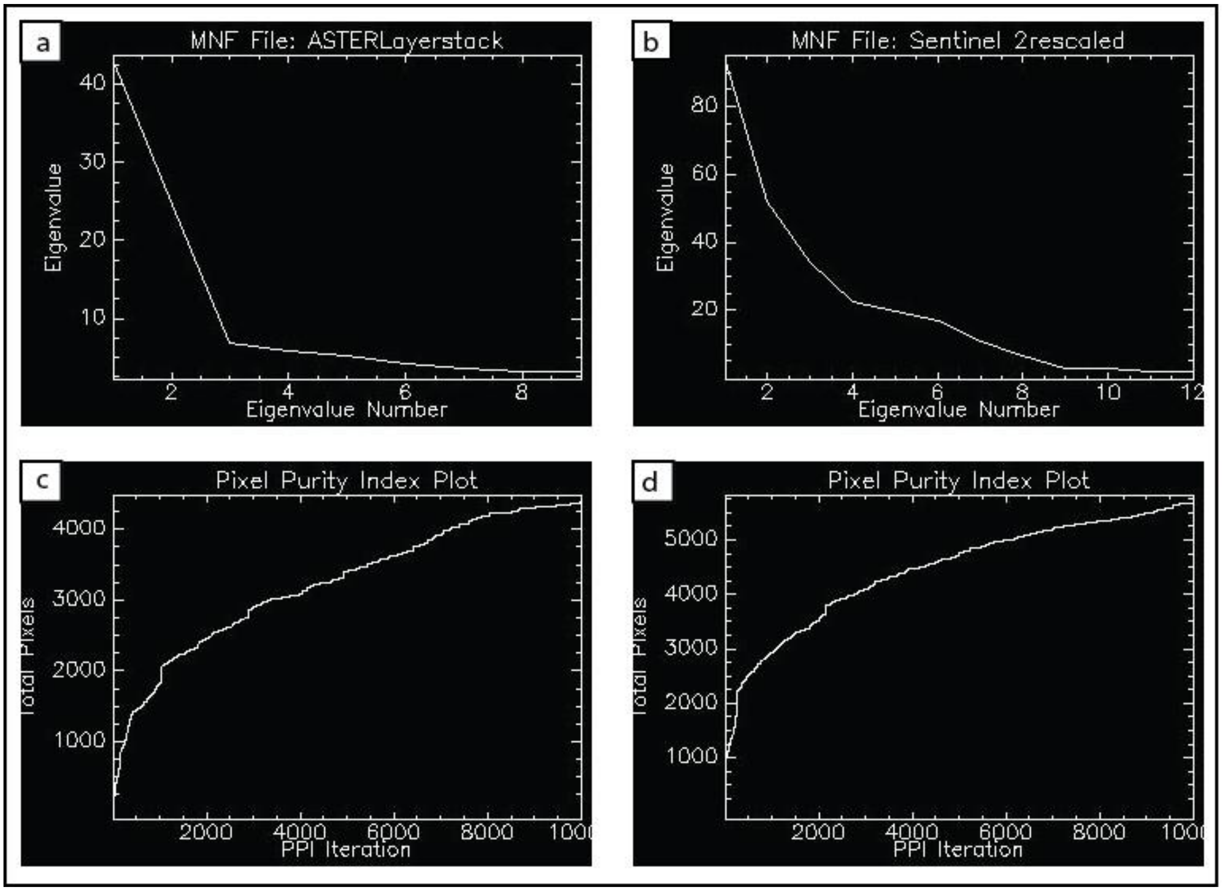

Figure 4. 9 Minimum noise fraction of ASTER (a), Sentinel 2 (b), and Pixel purity index plot of ASTER (c) and Sentinel 2 (d)

Table 4. 3 Minimum noise fraction eigenvalues

MNF bands	1	2	3	4	5	6	7	8	9	10	11	12
ASTER MNF eigenvalues	55.05	29.90	8.09	6.77	5.94	4.57	3.97	3.46	3.39			
Sentinel2 MNF eigenvalues	92.97	52.15	34.35	22.39	19.43	16.83	10.66	6.36	2.93		1.81	1.69

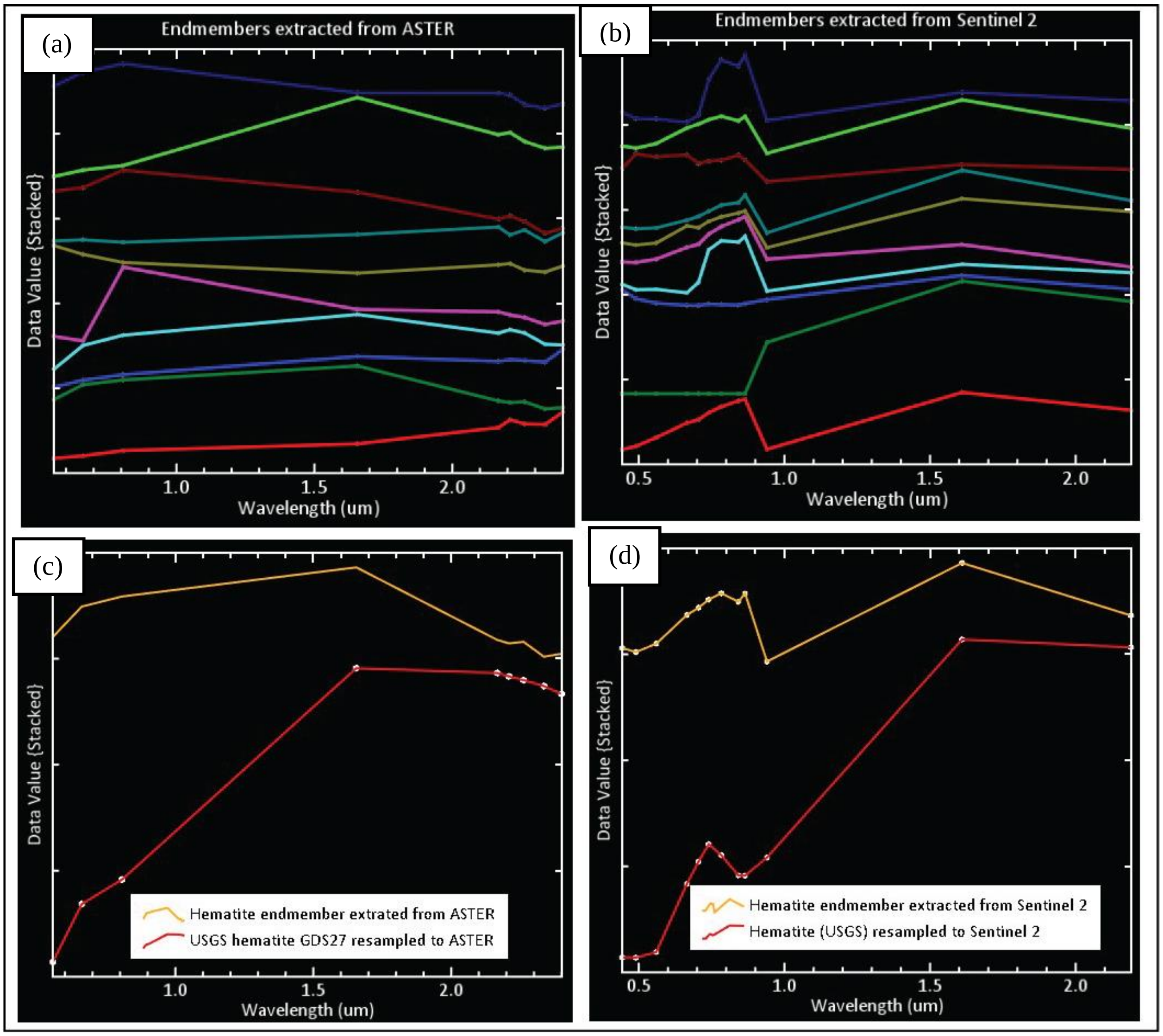

Figure 4. 10 Spectral plot of endmembers extracted from ASTER (a), Sentinel 2 (b), comparison of the spectral plot of USGS hematite with ASTER (c) and Sentinel 2 (d)

Table 4. 4 Spectral feature fit of endmember collected from images

Endmembers selected	SFF match (hematite)	SFF match (goethite)	SFF match (jarosite)
ASTER n-d class 2	0.74	0.603	0.52
Sentinel 2 n-d class 10	0.86	0.78	0.53

4.4.2. Mixtute tuned matched filtering and linear spectral unmixing

Iron mineralized zones (hematite mineralization potential areas) in mixture-tuned matched filtering (MTMF) and linear spectral unmixing (LSU) fractional images are seen as bright pixels.

The brightness indicates the strong match of the image spectrum with the hematite end member. The output of MTMF contains two separate rule images for each end member, MF score and infeasibility score. The fractional abundance image of the iron hematite in the MTMF was chosen using the endmember class assigned and ground truth data of well-studied iron blocks in the study area. MF score is a floating value ranging from 0 to 1, indicating a relative match of endmember's spectrum with pixels spectra, with 1 perfect match of endmember spectra with pixel spectra. The infeasibility score associated with each MF image is a measure of the feasibility of the match score in which lower values of infeasibility suggest much more reliability of match between end member and image spectra. 2D scatter plot of matched filtering image of selected endmember shows gretater match which is MF score of nearly above 0.5 value and infeasibility value 0 on both datasets which shows a great match of endmember with image spectrum (Figure 4.11). LSU gives an abundance of images for each end member and one RMS error. In the brightest areas in LSU the abundance image corresponds to a high abundance of the endmember, while darker areas indicate a low abundance of the endmember. 2D plot of linear spectral unmixing abundance image shows different pixels contain 45−100% of selected hematite enmember at nearly 0 RMS error. ASTER linear specral unmixing contains 50% of hematite endmeber selected. In both methods applied to both datasets higher math was located at Sirrel, Feya, Tsemera and Akme Yehonnes localities (Figure 4.12).

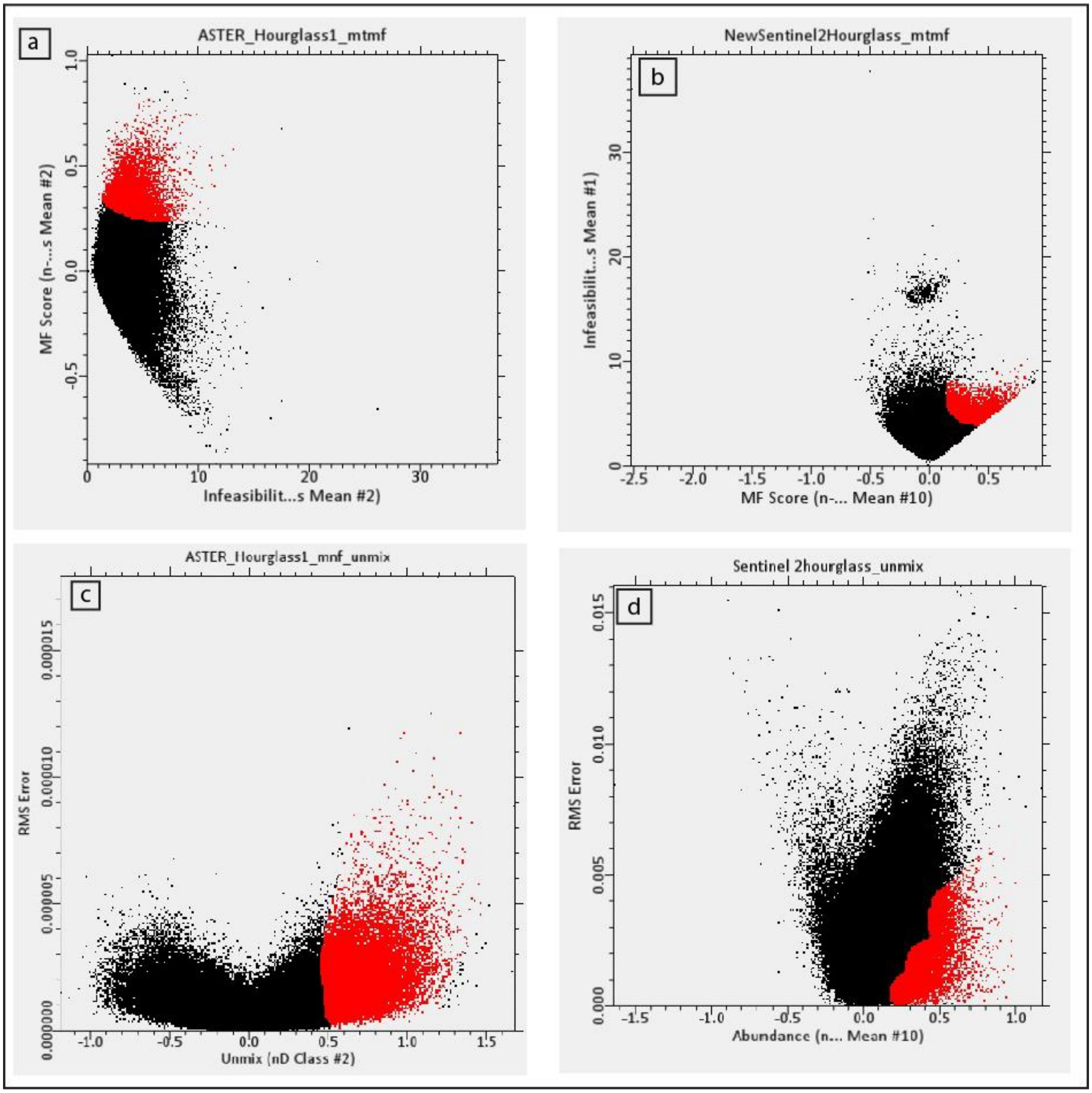

Figure 4. 11 2D scatter plot of MTMF ASTER (a), Sentinel 2 (b), and LSU of ASTER (c) and Sentinel 2 (d).

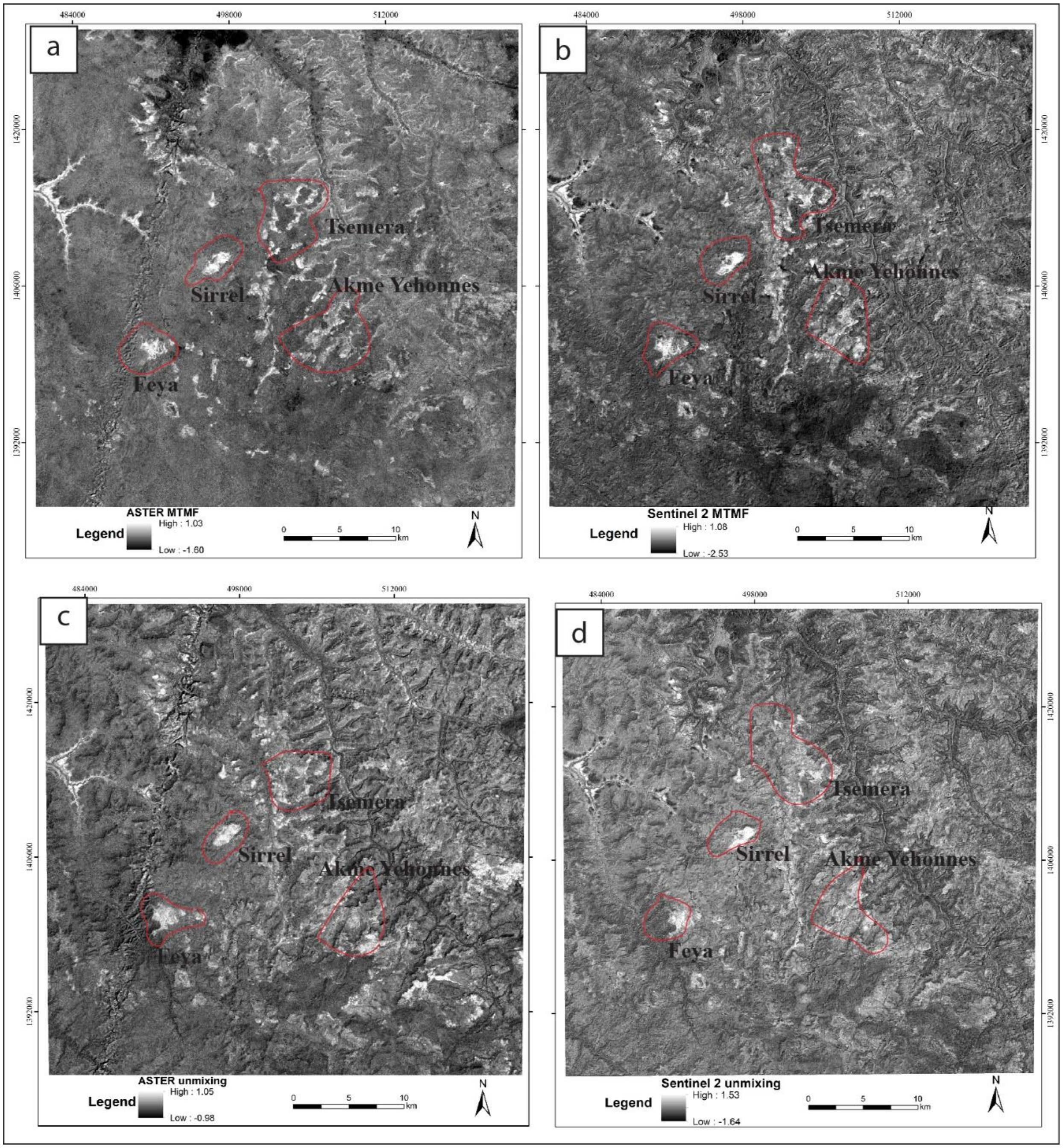

Figure 4. 12 Mixture tuned matched filtering fractional image of ASTER (a), Sentinel 2 (b), and linear spectral unmixing image of ASTER (c), and Sentinel 2(d)

4.5. XRD and geochemical analysis

X-ray powder diffraction analysis of 10 samples collected shows characteristic peaks at different 2theta angle values. The number of characteristic matching peaks ranges from 6 to 34 which resembles the diffraction pattern of hematite and quartz minerals. These peaks are calculated from raw powder diffraction data (Appendix 3). The diffraction pattern has high peaks at 2theta/degree values of 33.32 and 35.71 which is a distinctive characteristic of hematite mineral with a relative intensity of 1000. Other 2theta values, small peaks on the diffraction pattern that matched with hematite include; 24.26, 41.06, 49.71, and 54.34 (Figure 4.13, Figure 4.14 and Figure 4.15). The measure of the difference between original powder diffraction and Rietveld refinement/calculated pattern (weighted refinement R-factor (Rwp)) ranges from 3.1%−5.5%. The maximum figure of merit (FoM), match value is 0.86 for hematite and 0.77 for quartz/tridymite.

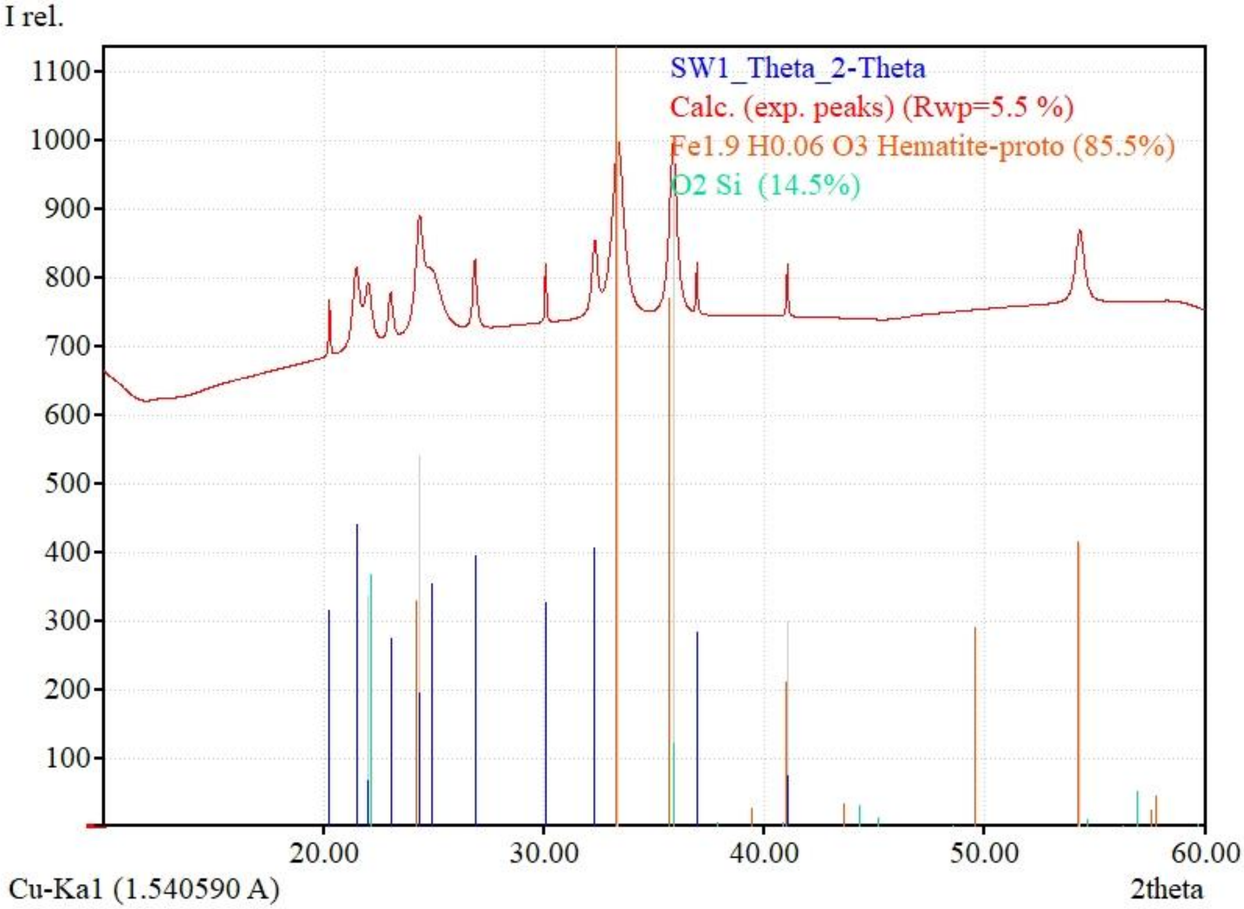

Figure 4. 13 Powder diffraction analysis of sample taken from Sirrel iron block

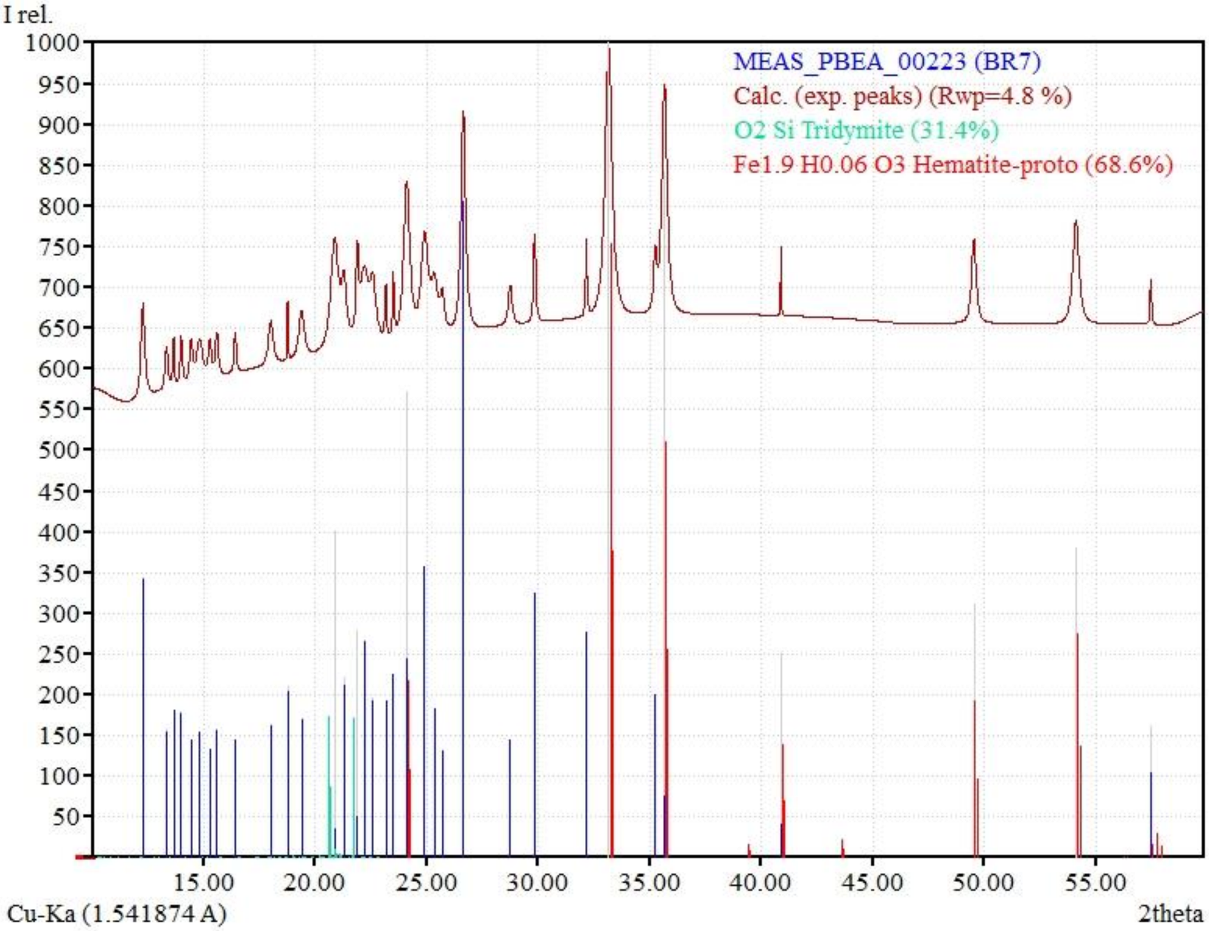

Figure 4. 14 Powder diffraction analysis of sample taken Shinaba locality

The sample obtained from Sirrel iron block show high amount hematite phase (85.5%) with small amount of quartz (14.5%) (Table 4.5). The figure of merit (FoM) of the hematite match in this sample is found 0.80 and 0.67 for quartz at a weighted refinement R-factor (Rwp) of 5.5%. Sample taken from Akime Yehonnes iron block also has a high amount of hematite phase, about 76.0% weight, and 24.0% of tridymite-type quartz phase. Sample with code BR7 taken from Shinaba iron block also shows a high hematite phase of 68.6% weight and a tridymite phase of 31.4% weight and the refinement R-factor (Rwp) is 4.8%. Shinaba sample has 68.6 % weight of hematite and 31.4% quartz and the Rwp was 5.4%. The figure of merit (FoM) of Sinaba and Akme Yehonnes sample were 0.79 and 0.86 respectively. Secondary geochemical analysis data provided by the Ethiopian Geological Institute also revealed the concentration of hematite-type iron ore mineralization in the different locations of the study area. the hematite composition ranges from 49.4 to 63.0 with a substantial amount of quartz mineral (SiO_2) and aluminum oxide (Al_2O_3) (Table 4.6).

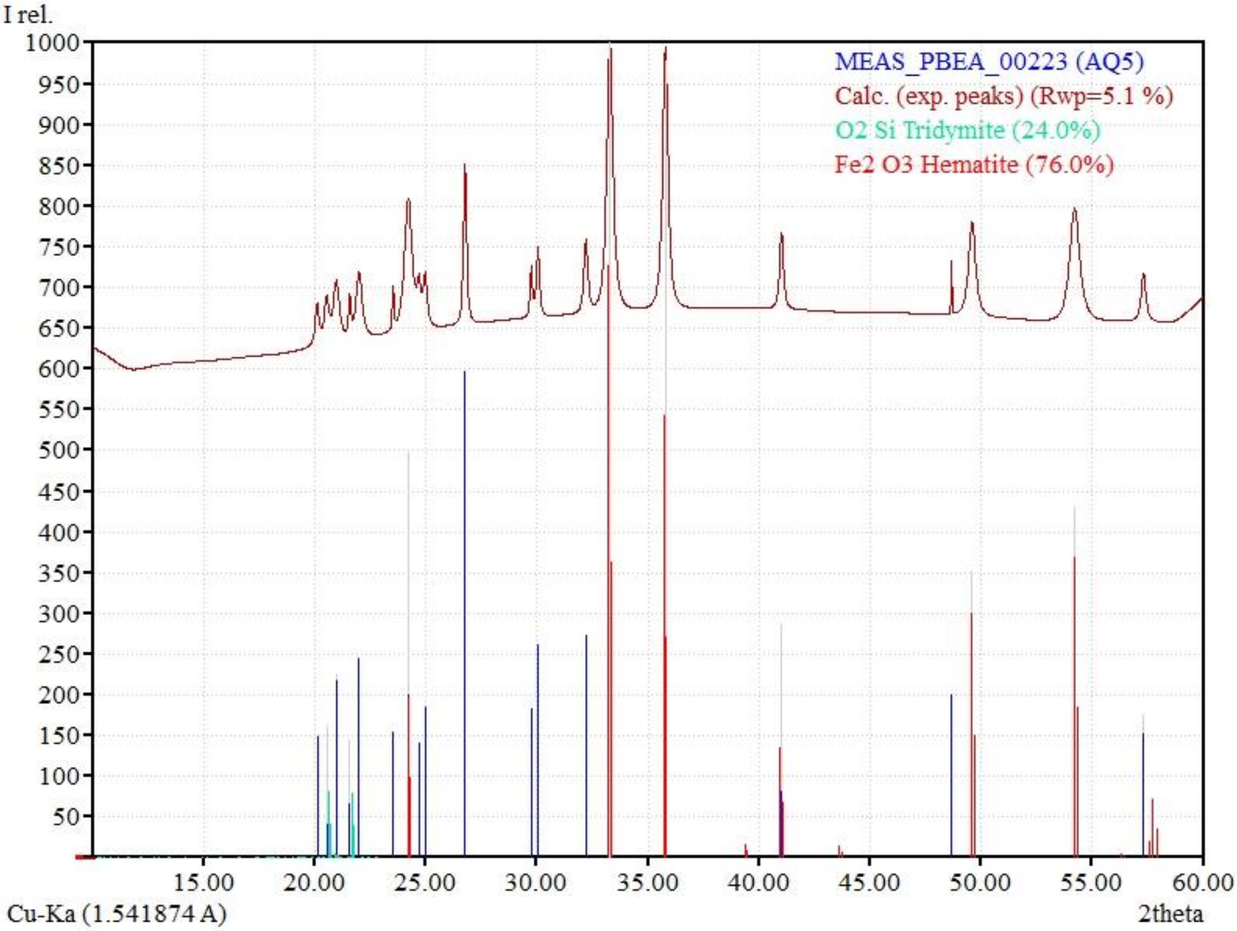

Figure 4. 15 Powder diffraction analysis of sample taken from Akme Yehonnes locality

Table 4. 5 Mineralogical phase (weight %) determined from XRD analysis

	Phase composition (%)			
S. code	Hematite	Quartz/Tridymite	Siderite	Rwp (%)
Aq5	76.0	24.0	−	5.1
BR7	68.6	31.4	−	4.8
DR5	57.8	42.2	−	4.5
JR1	36.9	63.1	−	3.3
RB1	70.5	−	29.5	4.9
SW1	85.5	14.5	−	5.5
TS1	50.4	49.6	−	5.4
WL4	38.8	61.2	−	4.7
SK3	53.7	46.4	−	5.0

Table 4. 6 Secondary geochemical analysis data provided by EGI. The sample codes Sk, Sn, and Lz represent Sirrel, Shinaba, and Akem Yehonnes iron occurrence blocks respectively.

S. code	SiO_2	Al_2O_3	Fe_2O_3	CaO	MgO	Na_2O	K_2O	MnO	P_2O_5	TiO_2	H_2O	LOI
Sk-1	32.42	11.1	49.9	<0.01	0.2	<0.01	<0.01	<0.01	0.14	0.23	0.49	5.8
Sk-2	29.96	10.6	54.2	<0.01	0.12	<0.01	<0.01	<0.01	0.17	0.23	0.48	5.2
Sk-3	27.98	10	55.0	<0.01	<0.01	<0.01	<0.01	<0.01	0.16	0.27	<0.01	6.1
Skb3s2	24.06	6.04	63.0	2.12	<0.01	<0.01	0.8	<0.01	0.18	0.49	0.85	3.6
Sn-b1s3	29.06	12.5	51.3	<0.01	<0.01	<0.01	<0.01	<0.01	0.08	0.29	0.53	6.5
Sn-b2s2	24.46	9.9	59.4	<0.01	<0.01	<0.01	<0.01	<0.01	0.21	0.25	0.84	4.9
Sn-b2s7	21.56	9.36	61.2	<0.01	<0.01	<0.01	<0.01	<0.01	0.21	0.29	0.3	6.4
Lz-b1-1	27.86	10.5	55.5	<0.01	<0.01	<0.01	<0.01	<0.01	0.26	0.33	0.45	5.0
Lz-b1-2	29.04	9.76	55.1	<0.01	<0.01	<0.01	<0.01	<0.01	0.33	0.36	0.6	5.0
Lz-b1-3	29.68	10.9	51.6	<0.01	<0.01	<0.01	<0.01	<0.01	0.36	0.27	0.32	6.0

4.6. Correlation and validation

Intercorrelation of methods employed and dataset showed moderate to very high positive correlation. ASTER PC4 and Sentinel 2 PC3 show a high positive correlation (r=0.85, 0.83) with hematite band ratios ASB2/B1 and S2B4/B2 respectively (Figure 4.16). Hematite abundance mapped with both principal components had 133.40 and 110.70 km^2 for ASTER PC4 and Sentinel PC3 respectively. The anomaly areas delineated from both PCs cover nearly the same area extent with a small variation of 22.7 km^2. Lateritic iron band ratios of ASTER and Sentinel 2 have also shown a high positive correlation (r=0.74). This is due to the band ratio being calculated utilizing bands from both sensors which have similar central wavelengths. ASTER band 4 (1.65 μm) and band 5 (2.165 μm) analogous to Sentinel band 11 (1.61 μm) and band 12 (2.190 μm) are located nearly at the same locations in the electromagnetic spectrum. Hematite band ratios of ASTER (ASB2B1) and Sentinel 2 (S2B4/B2) show a moderate positive correlation (r=0.36). Even though ASTER and Sentinel 2 band ratios used have given a comparable result in mapping iron ore deposits, the correlation becomes moderately positive correlation due to the difference in response of various materials to bands selected for band ratio calculation. The iron minerals absorb the blue band and reflect the red band of the electromagnetic spectrum. But, due to the position of the central wavelength of a blue band of ASTER (0.56 μm), and Sentinel 2 blue band (0.490 μm) red band (0.665 μm) makes the spectral response of materials other than iron deposit different. This creates variation in the trend of band ratio values which is the main cause for low correlation. Similarly, the principal components of both datasets showed a low positive correlation (r=0.39).

Subpixel mapping techniques showed a moderately high positive correlation in the case of MTMF and a low positive correlation concerning linear spectral unmixing. ASTER and Sentinel 2 show a moderate positive correlation(r=0.52) in the case of mixture-tuned matched filtering. ASTER and Sentinel 2 unmixing showed a medium show moderate positive correlation (r=0.41) and ASTER unmixing and MTMF had also a moderate positive correlation (r=0.37). In this research, the intercorrelation of methods and the same methods on different sensors had moderate to high positive correlation. Most of the hematite mineralization zones detected with both data belong to Adigrat and Ambaraom sandstone.

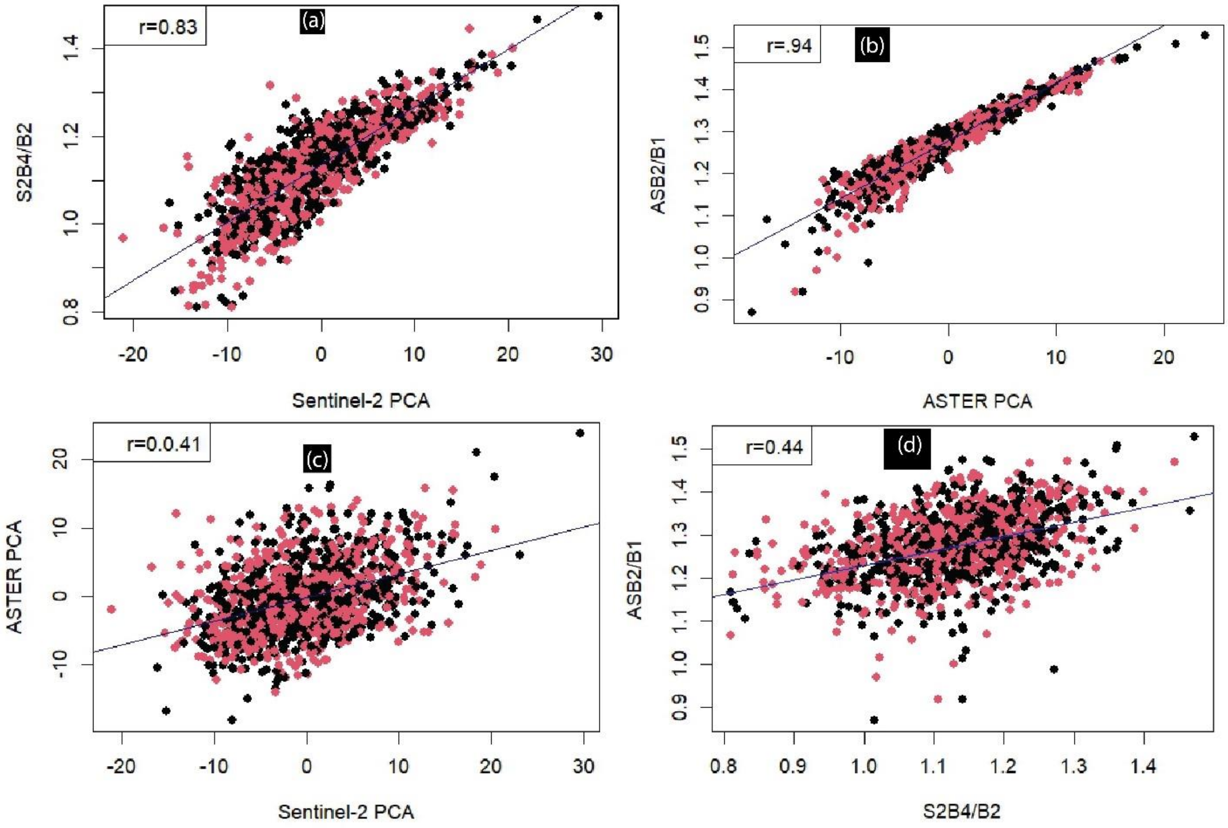

Figure 4. 16 Graph showing the correlation between pixel-based hematite abundance mapping methods for ASTER and Sentinel-2 data

The Access Capital SC. (2012) iron ore exploration map (iron mineralization polygons) fits hematite abundance of pixel and sub-pixel level mapping techniques both in ASTER and Sentinel 2 data (Figure 4.18 and Figure 4.19). Three existing polygons hematite deposit map perfectly matches with identified hematite anomalies zones mapped using band ratios, principal component analysis, mixture tuned matched filtering, and linear spectral unmixing. Filed observation of surface exposed iron crests are at different localities overlay the mapped hematite zones. Field observation of Sirrel iron-ore block found iron mineralization in two parts located between the coordinates’ latitude 496550−497800 E and longitude 1407650−1409300 N and covers surface over an area of 1,000 meters by 300 meters in the southern part and an area of 800 meters by 100 meters in the northern part. Shinaba iron ore mineralization is exposed and covers approximately an area of 1,200 meters by 1,800 meters.

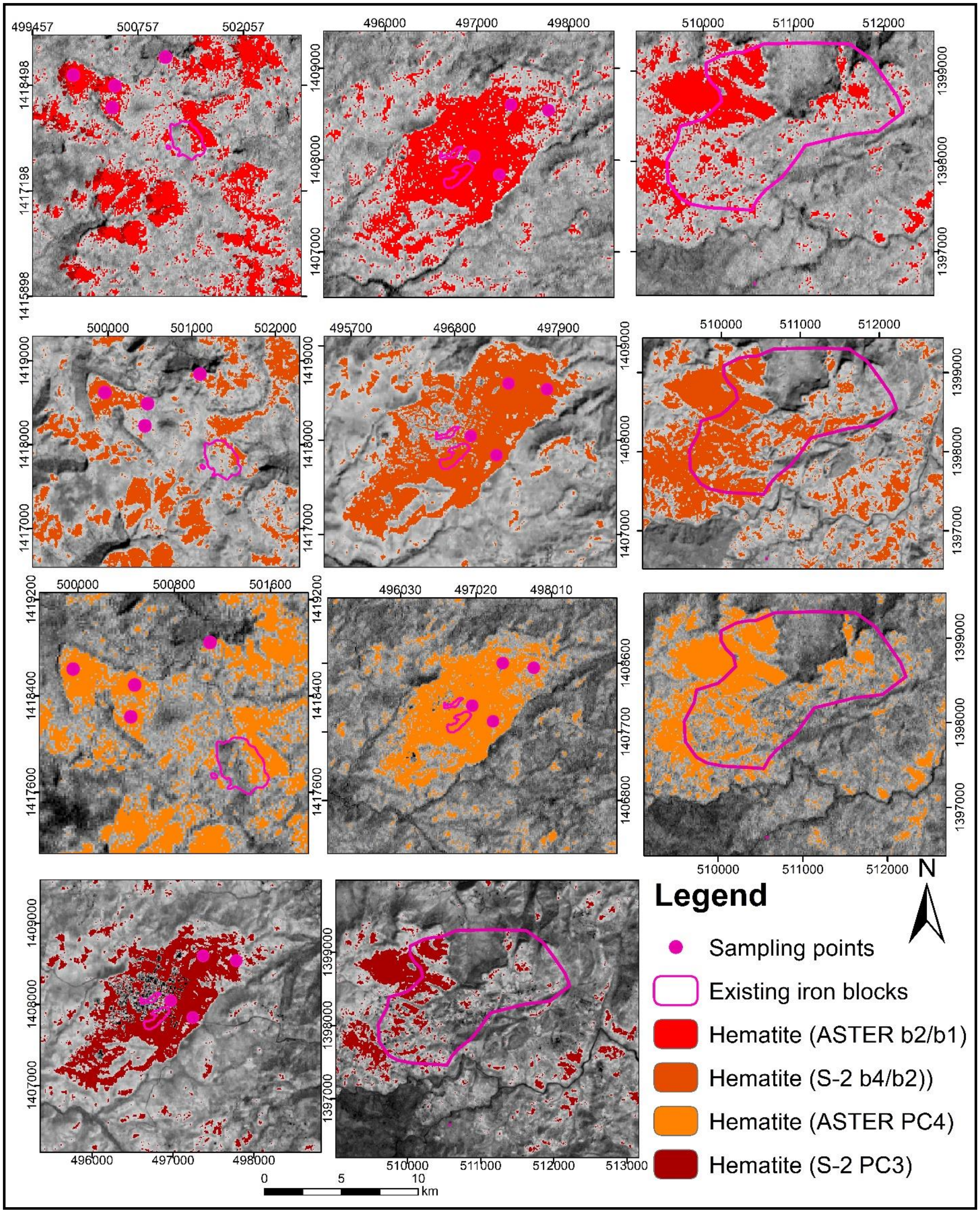

Figure 4. 17 Validation of band ratio and PCA mapping techniques with known iron polygons

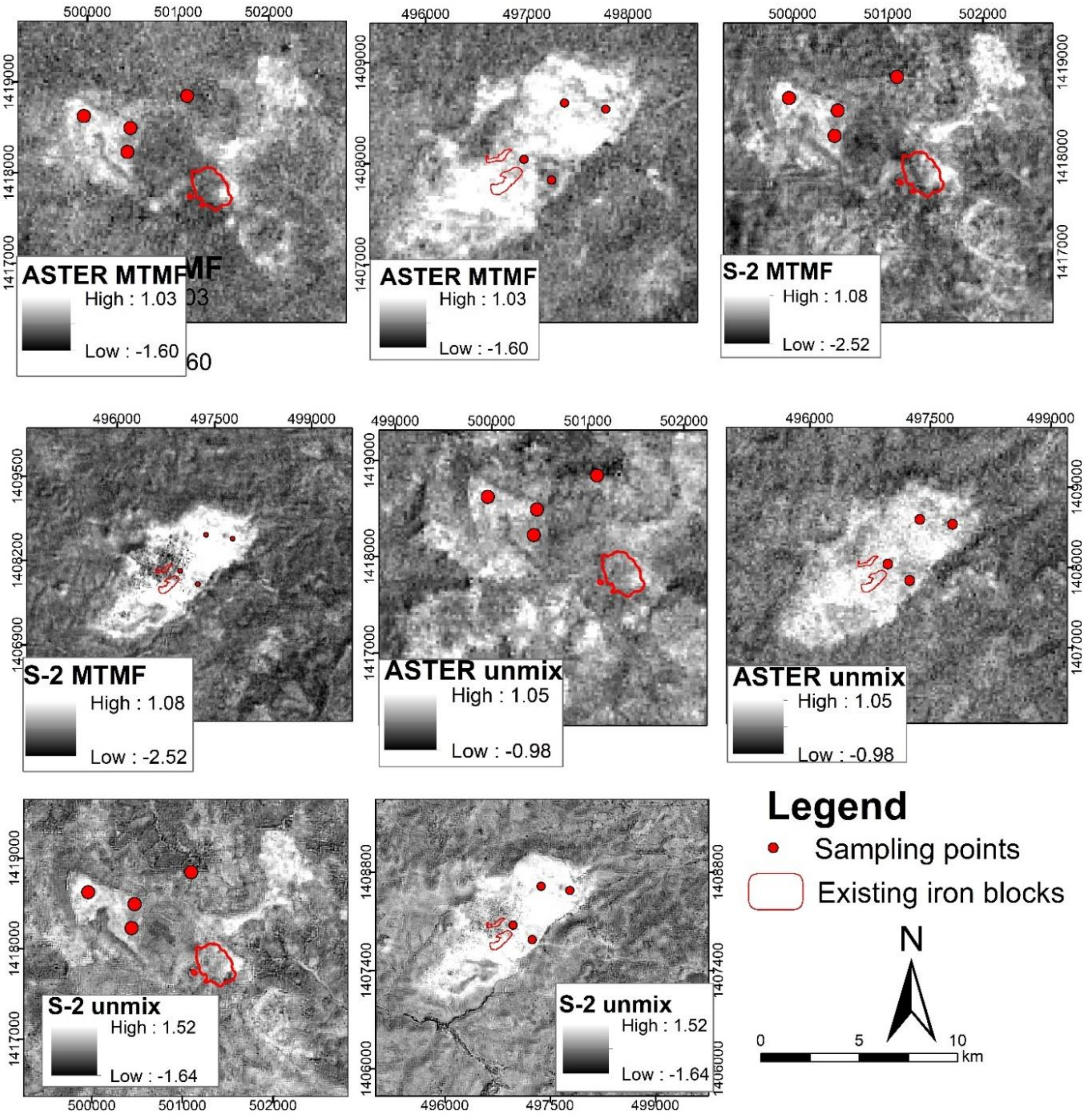

Figure 4. 18 Validation of sub-pixel mapping techniques

Iron ore mineralization at the Gozakem Dastu site located approximately 9 km East to South East of Sekota town and the observed iron-ore mineralization is located between the coordinates 511700−512850 E and longitude 1393000−1395300 N. Sampling points were overlaid on hematite anomaly and had high amount of hematite phase (30.0−85.5.0% of hematite) in powder diffraction and (49.4−63.0 % of Fe_2O_3) in geochemical analysis.

CHAPTER FIVE

5. Discussion

5.1. NDVI and vegetation masking

The reflectance characteristics of vegetation are similar to iron oxides in the SWIR and NIR infrared regions of the electromagnetic spectrum. Healthy vegetation highly absorbs wavelengths around 0.45 and 0.67 µm and highly reflects wavelength range between 0.68 and 0.75 m which is commonly called red edge. Similarly, iron oxides have characteristic absorption characteristics in blue and reflectance in red wavelength ranges of the electromagnetic spectrum. This may cause misinterpretation of results. In this study vegetation index, and natural difference vegetation index (NDVI) were used to identify potential vegetated areas .

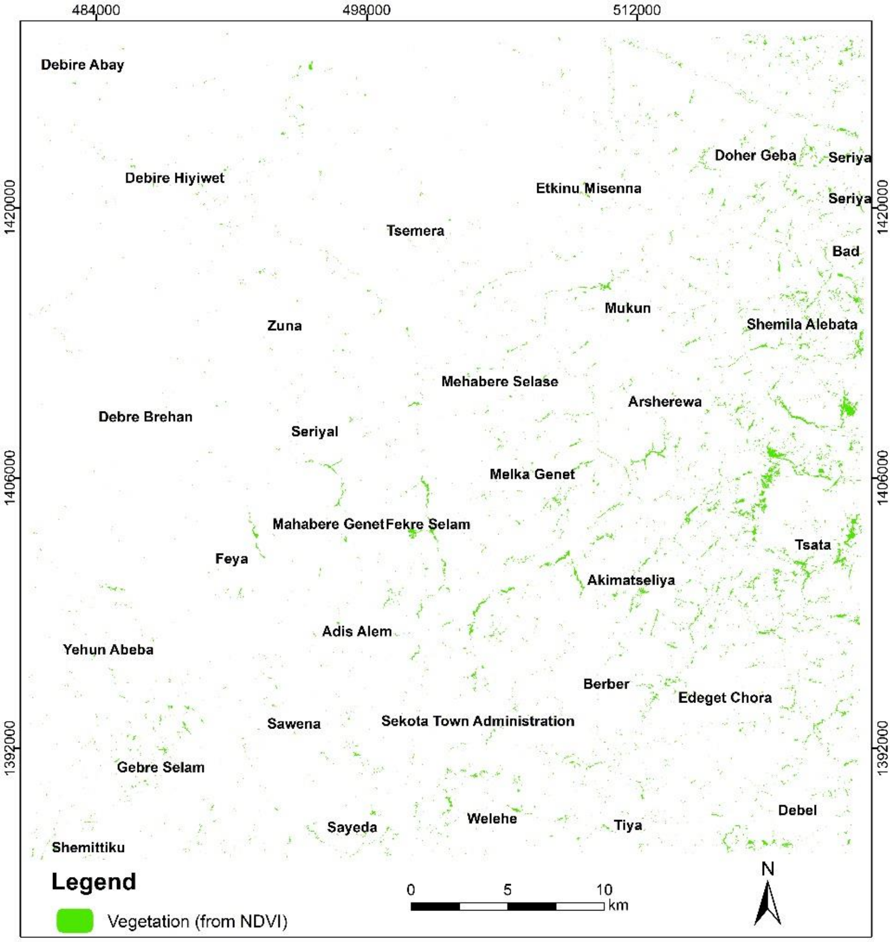

Figure 5. 1 Vegetation mapping from NDVI

To identify potential vegetation cover researchers researchers used ASTER NDVI values greater than 0.4 values should be masked out as vegetation from analysis (Abay et al., 2022), Gopinathan et al., 2020). In this study areas having NDVI values greater than 0.3 for both ASTER and Sentinel 2 were considered vegetation coverage and were masked out. This avoids misinterpretation that might come from vegetation spectra. The areas having NDVI values greater than 0.3 value are very small accounting for 22 km2 of area, which is a good indication that most reflectance comes from surface exposed rocks and soils.

5.2. Band rationing

ASB2/B1 band ratio is a fast and effective technique in mapping ferric iron oxides (hematite-type iron mineralization) and it is used by different researchers in many parts of the world (Gopinathan et al., 2020; Abay et al., 2022). The analogous Sentinel 2 band ratio (S2B4/B2) used in this research has similar results. The central wavelength positions of ASB2/B1 are 0.66 and 0.56 μm which is analogous to Sentinel band 4 (0.665 μm) and band 2 (0.490 μm).

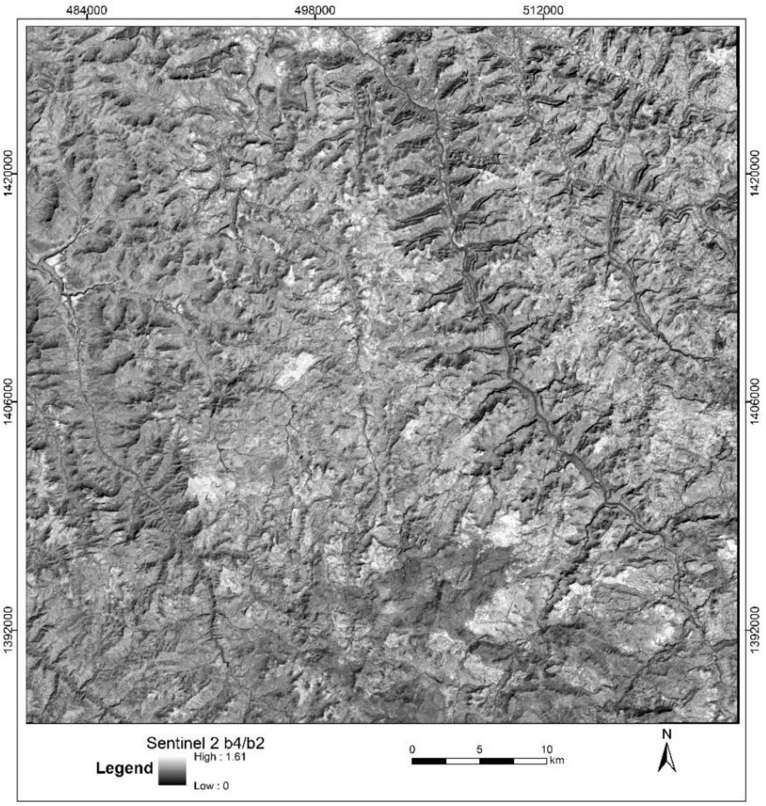

Figure 5. 2 Sentinel 2 band ratio (b4/b2)

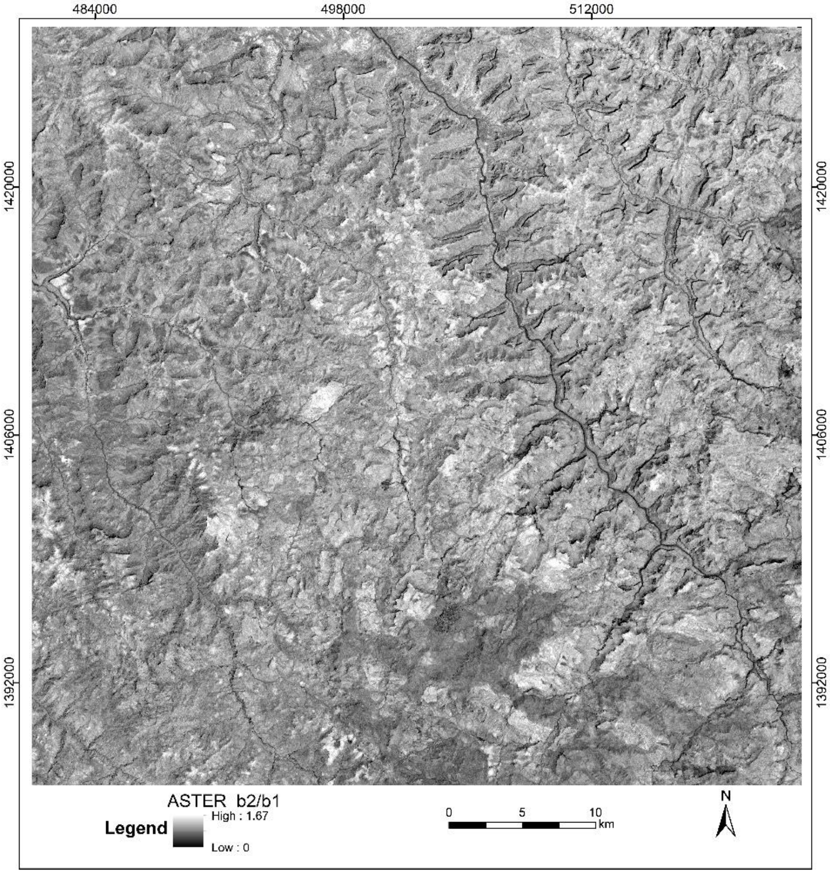

Figure 5. 3 ASTER band ratios

The ASB2/B1 and analogous S2B4/B2 were effective in and detected in many parts of the study area. The S2B4/B2 band ratio result is better in locating hematite mineralization precisely. ASTER lateritic band ratio lateritic iron delineated by ASb4/b5 and S2B4/B2 also showed the presence of iron mineralization at river gorges and valley slopes. To identify anomalies areas threshold values were computed using mean and standard deviation statistically. This technique was used by Abay et al (2022) and Ghoneim et al., (2022). Hematite anomalies zones delineated by both ASB2/B1 and S2B4/B2 band ratios showed high hematite phase, 36.9−85% of hematite (Fe_2O_3) composition in powder diffraction analysis, and (49.4−63.0 Fe2O3) in geochemical analysis. Intercorrelation of the two band ratios found Pearson's correlation coefficient of r=0.36 for hematite band ratios and 0.74 for lateritic iron band ratios. The hematite band ratios have a moderate positive correlation. The two band ratios have produced almost similar results in delineation of hematite abundance zones but low correlation is caused by different features reflectance other than iron deposits. The correlation points were randomly generated and are mostly out of hematite outcrops on the surface of the Earth. Those features have different responses to the bands used in this rationing.

5.3. Feature-oriented PCA

The first four bands of ASTER are characteristic bands in which the iron minerals' distinctive high absorption and reflectance features are found. Due to this reason, these bands were suited to calculate principal component analysis by different researchers (Ghoneim et al., 2022; Traore et al., 2020). Sentinel 2 bands b2, b4, b7, and b8a were also used in this research in PCA calculation. Bands 2 and 4 of Sentinel 2 are analogous to ASTER bands 1 and 2. The Sentinel 2 bands were selected depending on the position of bands in the electromagnetic spectrum. The wavelength position of band 3 (0.82 µm) and band 4 (1.65 µm) is comparable to the selected bands of Sentinel, band 7 (0.78 µm), and band 8a (0.865 µm). The contribution of original bands to each principal component was evaluated to select the component that highlights iron mineralization as used by (Ghoneim et al., 2022; Traore et al., 2020). The target can be detected as black or bright pixels depending on the contribution of original bands and eigenvalues. If ASTER PC 4 had contrasting values in absorption and reflexive bands of ASTER. It had −0.83 in band 1 of and 0.55 in band 2 of ASTER. Band 3 and four had insignificant values which are near to 0 which is 0.07 in band 3 and −0.002 in band 4). In this case, iron mineralized zones are shown in bright pixels. Similarly, PC3 of Sentinel 2 had contrasting eigenvalues in band 2 (−0.89) and 0.44 in band 4 of Sentinel 2 (Table 4.2). If the principal component has large negative eigenvalue loading in the absorption band and high positive eigenvalue loadings in the reflexive band, the target is highlighted in bright pixels (Gupta et al., 2013 Crosta et al., 2003). Hematite anomalies were delineated by statistical thresholding in which slicing of fractional images by using threshold values as Abay et al., (2022) did. The threshold values used were 6.99 and 171.65 for ASTER PC4 and Sentinel 2 PC3 respectively. Intercorrelation between the ASTE PC4 and Sentinel 2 PC3 showed a low positive correlation (r=0.34). The correlation of ASTER PC4 and Sentinel 2 PC3 with band ratios showed a very high positive correlation (r=0.85 and 0.83) respectively.

5.4. Sub-pixel abundance mapping

Sub-pixel level abundance mapping requires endmembers/reference spectra to map abundance of the endmember in the image. The use of reference spectra collected under different illumination conditions compared to satellite data poses a problem with abundance mapping. High spectral and spatial resolution remote sensing detests allow the collection of endmembers per pixel using different algorithms. The endmember collection from images requires several steps to follow as Abay eta al. (2022) used. First, the data noise should be reduced by noise reduction techniques. In the minimum noise reduction, the first 9 bands of ASTER and 12 bands of Sentinel bands were used except band 10 which is designed for cloud cirrus studies. After band 4, the last bands of ASTER exhibited nearly identical MNF eigenvalues which ranged from 5.94−.3.39 and Sentinel 2 MNF eigenvalues were unique except last 2 bands (band 11 and band 12). This means they don't have unique spectral information and they should be ignored in pixel purity index calculation and n-d visualization as used by Boardman et al. (1995). Consequently, this research has used only those bands that had unique eigenvalues. Pure pixels are shown in white color in PPI images (Figure 5.4 and Figure 5. 5).

Figure 5. 4 ASTER PPI

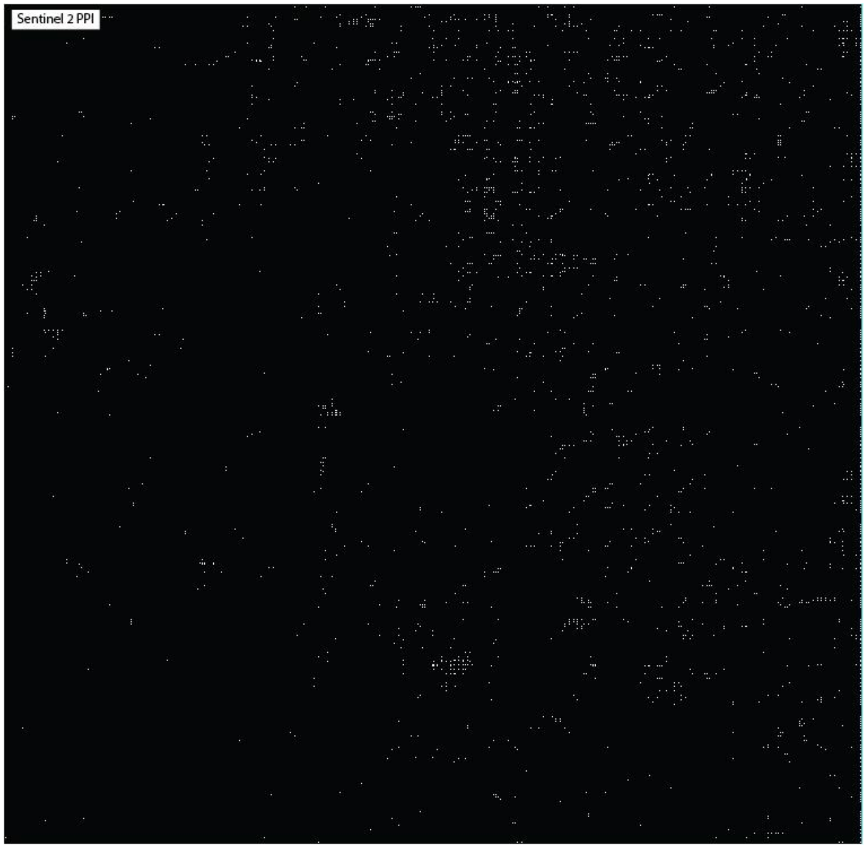

Figure 5. 5 Sentinel 2 PPI

There were numerous purer pixels identified which is good for identifying endmembers. After noise reduction, ENVI automatic endmember extraction retrieved 10 endmembers per pixel for both datasets. The USGS resampled iron minerals should be compared with endmembers extracted to see spectral feature fitting. Endmember class 2 of ASTER and class 10 of Sentinel 2 best fit with USGS resampled iron minerals. Sentinel 2 and ASTER endmembers showed SFF of 0.86 and 0.74 with USGS resampled hematite. The selection of end members was done in this manner. Then subpixel abundance mapping techniques were applied.

Mixture-tuned matched filtering (MTMF) shows matched scores and infeasibility for mapped targets. Hematite mineralized zones are shown as bright pixels in matched scores. The match score for both ASTER and Sentinel 2 MTMF is nearly 0.5 and greater and very negligible infeasibility score near zero. The matched score value near 1 means a high match of the image spectra with the selected hematite end member. Linear spectral unmixing results are comparable to both datasets. In the brightest pixels of LSU, the abundance image reflects a high presence of the end member, whereas darker regions indicate a low presence of the end member.

The results of the Spectral Angle Mapper (SAM) classification applied to ASTER and Sentinel-2 data found negligible areal coverage for the hematite endmember class (Figure). This result is due to the way SAM treats the end member spectra used for classification. SAM computes the angle between the entire spectral profile of a pixel and the entire spectral profile of a reference end member. In this case, the end members for hematite were chosen directly from the image spectra and there were no pixel spectra that matched the end member. The maximum difference degree allowed was 0.1. However, natural materials rarely exhibit a perfect spectral signature across all wavelengths. Since SAM considers the whole spectrum of the chosen end member, pixels with small spectral variations even if there were hematite in the image won't be classified as belonging to that class. This resulted hematite class mapped by SAM being very small in areal coverage observed in the results.

Powder diffraction analysis data is used to determine minerlogical phases while geochemical analysis of smaple shows major and minro oxides. Every crystalline mineral (or solid) has a unique set of interplanar spacing and relative intensities that forms a distinct X-ray diffraction (XRD) pattern. This XRD pattern serves as a fingerprint that can be used to identify the specific crystalline material (Sharma et al., 2012).. The quality of the XRD phase identification was quantified using the figure of merit (FoM). Every sample had a Figure of Merit (FoM) that was higher than the suggested cutoff of 0.66%, namely 0.7 %. The refinement R-factor (Rwp), in addition to the Figure of Merit (FoM), is another quantitative indicator of how well the XRD phase identification was done. The Rwp number should ideally be less than 13%. For our samples, the refinement R-factor (Rwp) ranges from 4.8% to 5.5%, suggesting a satisfactory match between the calculated and observed patterns. This is far less than the 10% generally commonly accepted cutoff point for refinement R-factor (Rwp).

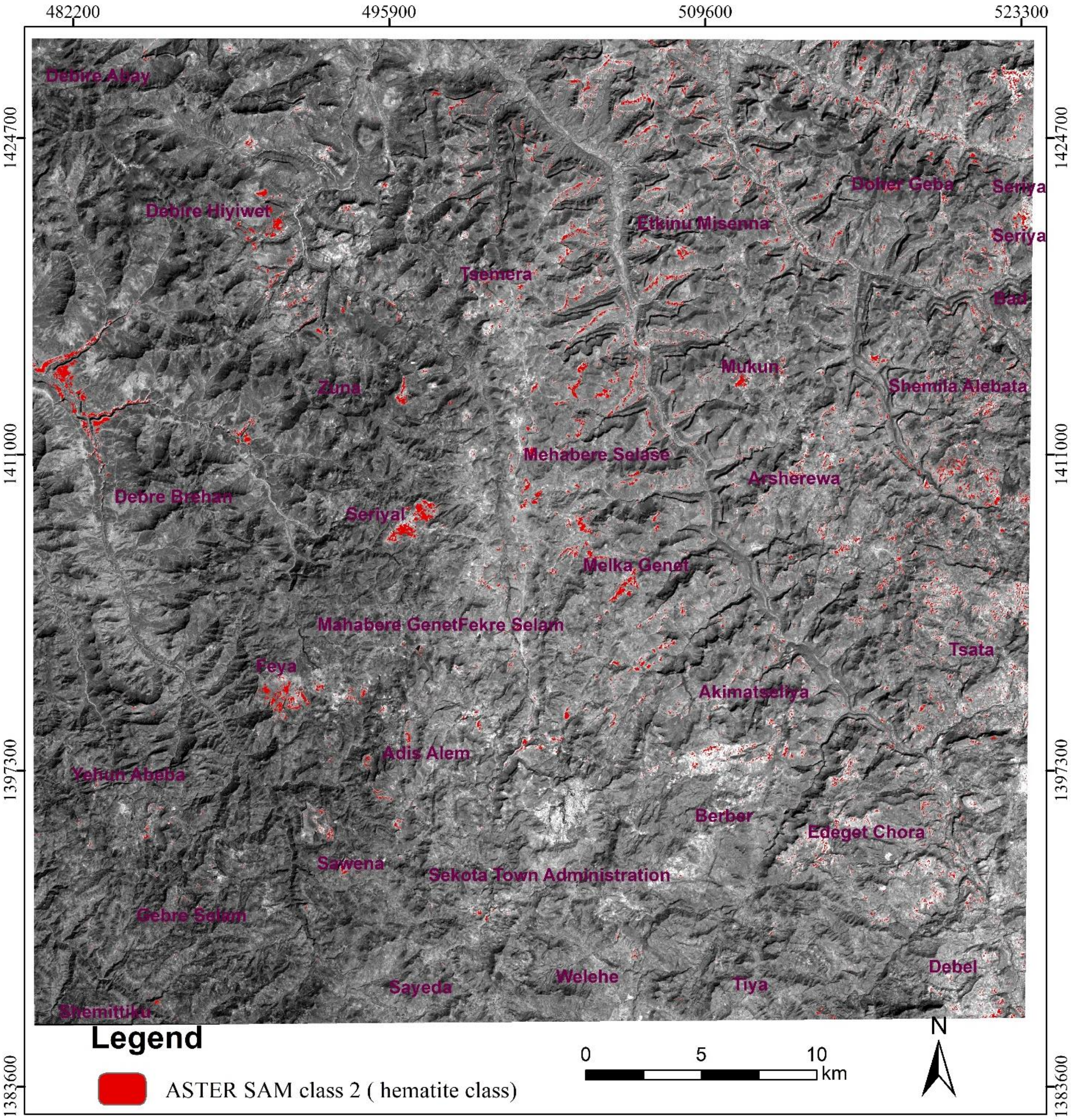

Figure 5. 6 ASTER spectral angle mapper hematite class draped over band of ASTER

CHAPTER SIX

6. Conclusion and recommendations

6.1. Conclusion

This study conducted remote sensing-based data, x-ray powder diffraction, and geochemical analysis to map the distribution of iron ore deposits, especially hematite mineralized zones in the Sekota district of Waghirma zone, Amhara region, Northern Ethiopia. It utilized ASTER and Sentinel 2 remote sensing datasets to map the abundance of hematite. The absence of thick vegetation cover and the presence of exposed bedrock covering 70% of the study area allowed the effective use of remote sensing techniques for mineral mapping. ASB2/B1 and S2B4/B2 band ratio, ASTER PC4, and Sentinel 2 PC3 effectively mapped the abundance of hematite iron deposits in different parts of the study area. Besides the hematite (ferric iron oxides) band ratio, lateritic iron band ratio (ASB4/B5) and S2B11/B12 were used and identified enriched lateritic iron localities. Sentinel 2 sensor has many bands in the VNIR and SWIR region of the electromagnetic spectrum and is very useful for choosing the band that is the characteristic position for minerals mapping.

Sup-pixel pixel mapping techniques like mixture-tuned matched filtering and linear spectral unmixing techniques were effectively utilized and mapped precisely the distribution of hematite minerals in the area. Remote sensing datasets that have spatial and spectral resolution like ASTER and Sentinel 2 can be effectively used for endmember collection. Hematite endmember collected from both remote sensing data has a high spectral feature fit with USGS resampled iron minerals. Mixture-tuned matched filtering and linear spectral feature techniques produced hematite matches in small areas of coverage. Inter-correlation of techniques and data used showed low to very high positive correlation. As the result of this research showed, the remote sensing datasets that have reasonable spectral and spatial resolution and appropriate preprocessing and mapping techniques employed, it is possible to demarcate potential mineralized zones if the vegetation cover is poor. Iron ore deposits can be mapped with remote sensing data because most iron minerals have distinctive reflectance and absorption characteristics in the VNIR and AWIR regions of the electromagnetic spectrum. The effectiveness methods used were validated with field, XRD, and geochemical data. Thus, the methods employed were cost-effective and fast prospecting techniques that could be used for other types of mineral mapping in the country.

6.2. Recommendations

This research revealed the presence of hematite iron deposits in many locations using free (public-domain) multispectral images. To map precise locations of iron deposits usage of high resolution like hyperspectral imageries is recommended. We further recommend onsite detail exploration including intensive sampling, trenching, drilling, and geochemical analysis to estimate the grade of iron and know the extent of the reserve. Since the country is dependent on imported iron government should invest to conduct a detailed thorough exploration to obtain a clear picture of the local potential of iron and initiate private companies to take part in the exploration, and development of the iron resource.

References

Abay, H. H., Legesse, D., Venkata Suryabhagavan, K., & Atnafu, B. (2022). Mapping of ferric (Fe3+) and ferrous (Fe2+) iron oxides distribution using ASTER and Landsat 8 OLI data, in Negash Lateritic iron deposit, Northern Ethiopia. *Geology, Ecology, and Landscapes*, 1-18.

Adiri, Z., Lhissou, R., El Harti, A., Jellouli, A., & Chakouri, M. (2020). Recent advances in the use of public domain satellite imagery for mineral exploration: A review of Landsat-8 and Sentinel-2 applications. *Ore Geology Reviews*, *117*, 103332.

Baid, S., Tabit, A., Algouti, A., Algouti, A., Nafouri, I., Souddi, S., Aboulfaraj, A., Ezzahzi, S., & Elghouat, A. (2023). Lithological discrimination and mineralogical mapping using Landsat-8 OLI and ASTER remote sensing data: Igoudrane region, Jbel Saghro, Anti Atlas, Morocco. *Heliyon*, *9*(7).

Bajwa, R. S., Ahsan, N., & Ahmad, S. R. (2020). A Review of Landsat False Color Composite Images for Lithological Mapping of Pre-Cambrian to Recent Rocks: A Case Study of Pail/Padhrar Area in Punjab Province, Pakistan. *Journal of the Indian Society of Remote Sensing*, *48*, 721-728.

Behnia, P. (2007). Applying Mineral Mapping on Hyperspectral Data Using Spectral Feature Fitting Method Case Study: Abtorsh Area, Iran. 12th Conference of Int. Association for Mathematical Geology

Beyth, M., & Beyth, M. (1973, January 1). The Paleozoic-Mesozoic sedimentary basin of the Mekele Outlier; northern Ethiopia. EurekaMag. https://eurekamag.com/research/018/286/018286275.php

Beiranvand Pour, A., & Hashim, M. (2014). ASTER, ALI, and Hyperion sensors data for lithological mapping and ore minerals exploration. *SpringerPlus*, *3*, 1-19.

Bishop, J. L., Michalski, J. R., & Carter, J. (2017). Remote detection of clay minerals. In *Developments in clay science* (Vol. 8, pp. 482-514). Elsevier.

Bishta, A. Z., & Sonbul, A. R. (2021). Rock unit discriminations using image processing technique of Ablah area, Arabian shield, Saudi Arabia. *Journal of the Indian Society of Remote Sensing*, *49*(8), 1965-1984.

Boardman, J. W., Kruse, F. A., & Green, R. O. (1995, January 23). Mapping target signatures via partial unmixing of AVIRIS data. NASA Technical Reports Server (NTRS). https://ntrs.nasa.gov/citations/19950027316

Chattoraj, S., Sharma, R., Kumar, C., Champati ray, P., & Sengar, V. (2020). Identification and characterization of hydrothermally altered minerals using surface and space-based reflectance spectroscopy, in parts of south-eastern Rajasthan, India. *SN Applied Sciences*, *2*, 1-9.

Worash Getaneh, (2002). Geochemistry provenance and depositional tectonic setting of the Adigrat Sandstone northern Ethiopia. Journal of African Earth Sciences, 35(2), 185–198. https://doi.org/10.1016/s0899-5362(02)00126-4

Chen, X., Warner, T. A., & Campagna, D. J. (2010). Integrating visible, near-infrared and short-wave infrared hyperspectral and multispectral thermal imagery for geological mapping at Cuprite, Nevada: A rule-based system. *International journal of Remote sensing*, *31*(7), 1733-1752.

Clark, R., & Swayze, G. (1995). Automated spectral analysis: Mapping minerals, amorphous materials, environmental materials, vegetation, water, ice and snow, and other materials: The USGS Tricorder Algorithm. Abstracts of the Lunar and Planetary Science Conference, volume 26, page 255,(1995),

Content, C. (2017). Sekota Mining Plc to extract Iron Ore in Wag Himra Zone. *Horn Affairs*.

Crosta, A., De Souza Filho, C., Azevedo, F., & Brodie, C. (2003). Targeting key alteration minerals in epithermal deposits in Patagonia, Argentina, using ASTER imagery and principal component analysis. *International journal of Remote sensing*, *24*(21), 4233-4240.

Dadon, A., Ben-Dor, E., Beyth, M., & Karnieli, A. (2011). Examination of spaceborne imaging spectroscopy data utility for stratigraphic and lithologic mapping. *Journal of Applied Remote Sensing*, *5*(1), 053507-053507-053514.

Du, Q., Ren, H., & Chang, C. (2003). A comparative study for orthogonal subspace projection and constrained energy minimization. IEEE Transactions on Geoscience and Remote Sensing, 41(6), 1525–1529. https://doi.org/10.1109/tgrs.2003.813704

EG Sciences. (2022). *Geological satellite mapping and remote sensing*. https://egsciences.com/service/geological-satellite-mapping-and-remote-sensing/

EIGS., (1999). Explanation of the geological map of Ethiopia : scale 1:2,000,000 : 2nd edition | WorldCat.org. (1999). https://search.worldcat.org/title/Explanation-of-the-geological-map-of-Ethiopia-:-scale-1:2000000-:-2nd-edition/oclc/61123335

El Kati, I., Nakhcha, C., El Bakhchouch, O., & Tabyaoui, H. (2018). Application of Aster and Sentinel-2A Images for geological mapping in arid regions: The Safsafate Area in the Neogen Guercif basin, Northern Morocco. *Int. J. Adv. Remote Sens. GIS*, *7*, 2782-2792.

Endale, A. (2022). Ethiopia to substitute metal imports in five years. *The Reporter*

ESA. (2015). Sentinel 2 Handbook. https://sentinels.copernicus.eu/web/sentinel/user-guides/document-library/-/asset_publisher/xlslt4309D5h/content/sentinel-2-user-handbook

Ethiopian Geological Institute, (2011). Geological mapsheet of Ifat and Maychew

Fan, Y., Wang, H., Yang, X., Zhang, G., Li, Z., Tan, F., Zhang, S., & Wang, W. (2021). Application of high-resolution remote sensing technology for the iron ore deposits of the West Kunlun Mountains in China. Geologia Croatica, 74(1), 57–72. https://doi.org/10.4154/gc.2021.03

Fatima, K., Khan Khattak, M. U., Kausar, A. B., Toqeer, M., Haider, N., & Rehman, A. U. (2017). Minerals identification and mapping using ASTER satellite image. *Journal of Applied Remote Sensing*, *11*(4), 046006-046006.

Fraeman, A. A., Johnson, J. R., Arvidson, R. E., Rice, M. S., Wellington, D., Morris, R. V., Fox, V., Horgan, B. H. N., Jacob, S. R., & Salvatore, M. R. (2020). Synergistic ground and orbital observations of iron oxides on Mt. Sharp and Vera Rubin ridge. *Journal of Geophysical Research: Planets*, *125*(9), e2019JE006294.

Gad, S., & Kusky, T. (2007). ASTER spectral ratioing for lithological mapping in the Arabian–Nubian shield, the Neoproterozoic Wadi Kid area, Sinai, Egypt. *Gondwana research*, *11*(3), 326-335.

Gani, N. D., & Abdelsalam, M. G. (2006). Remote sensing analysis of the Gorge of the Nile, Ethiopia with emphasis on Dejen–Gohatsion region. *Journal of African Earth Sciences*, *44*(2), 135-150.

Ge, W., Cheng, Q., Tang, Y., Jing, L., & Gao, C. (2018b). Lithological classification using Sentinel-2A data in the Shibanjing ophiolite complex in Inner Mongolia, China. *Remote Sensing*, *10*(4), 638.

Ghoneim, S. M., Salem, S. M., El-Wahid, K. H. A., Anwar, M., Hegab, M. A. E.-R., Soliman, N. M., & Ali, H. F. (2022). Application of remote sensing techniques to identify iron ore deposits in the Central Eastern Desert, Egypt: a case study at Wadi Karim and Gabal El-Hadid areas. *Arabian Journal of Geosciences*, *15*(20), 1596.

Gopinathan, P., Parthiban, S., Magendran, T., Al-Quraishi, A. M. F., Singh, A. K., & Singh, P. K. (2020). Mapping of ferric (Fe3+) and ferrous (Fe2+) iron oxides distribution using band ratio techniques with ASTER data and geochemistry of Kanjamalai and Godumalai, Tamil Nadu, south India. *Remote Sensing Applications: Society and Environment*, *18*, 100306.

Gruninger, J., Ratkowski, A. J., & Hoke, M. L. (2004b). The sequential maximum angle convex cone (SMACC) endmember model. Proceedings of SPIE. https://doi.org/10.1117/12.543794

Guha, S., Govil, H., Tripathi, M. K., & Besoya, M. (2018). Evaluating crosta technique for alteration mineral mapping in Malanjkhand copper mines, India. The International Archives of the Photogrammetry, Remote Sensing and Spatial Information Sciences, XLII–5, 251–254. https://doi.org/10.5194/isprs-archives-xlii-5-251-2018

Gupta, R. P., Tiwari, R. K., Saini, V., & Srivastava, N. (2013). A simplified approach for interpreting principal component images. Advances in Remote Sensing, 02(02), 111–119. https://doi.org/10.4236/ars.2013.22015

Hagos, E., Kebede, S., & Alene, M. (2015b). REVIEW OF HYDROGEOLOGY OF TEKEZE RIVER BASIN: IMPLICATIONS FOR RURAL AND URBAN WATER SUPPLY IN THE REGION. http://ejol.aau.edu.et/index.php/SINET/article/view/7121

Hajibapir, G., Lotfi, M., Zarifi, A. Z., & Nezafati, N. (2014). Application of Different Image Processing Techniques on Aster and ETM+ Images for Exploration of Hydrothermal Alteration Associated with Copper Mineralizations Mapping Kehdolan Area (Eastern Azarbaijan Province-Iran). Open Journal of Geology, 04(11), 582–597. https://doi.org/10.4236/ojg.2014.411043

Honarmand, M., Ranjbar, H., & Shahabpour, J. (2012). Application of principal component analysis and spectral angle mapper in the mapping of hydrothermal alteration in the Jebal–Barez Area, Southeastern Iran. *Resource Geology*, *62*(2), 119-139.

Hùng, T. L. (2020). Hydrothermal Minerals Mapping using based on Remotely Sensed Data from Sentinel 2 Sattelite: a Case Study in Vinh Phuc Province, Northern Vietnam. Gornye Nauki I Tehnologii, 4(4), 309–317. https://doi.org/10.17073/2500-0632-2019-4-309-317

Isaacs, R. G., Wang, W. C., Worsham, R. D., & Goldenberg, S. (1987). Multiple scattering lowtran and fascode models. Applied Optics, 26(7), 1272. https://doi.org/10.1364/ao.26.001272

Jain, R., & Sharma, R. U. (2018). Mapping of mineral zones using the spectral feature fitting method in Jahazpur belt, Rajasthan, India. *Internat. Res. Jour. Engg. Tech.,(IRJET)*, *5*, 562-567.

Jing, C., Bokun, Y., Runsheng, W., Feng, T., Yingjun, Z., Dechang, L., Suming, Y., & Wei, S. (2014). Regional-scale mineral mapping using ASTER VNIR/SWIR data and validation of reflectance and mineral map products using airborne hyperspectral CASI/SASI data. *International Journal of Applied Earth Observation and Geoinformation*, *33*, 127-141.

Jolliffe, I. T., & Cadima, J. (2016). Principal component analysis: a review and recent developments. *Philosophical Transactions of the Royal Society A: Mathematical, Physical and Engineering Sciences*, *374*(2065), 20150202.

Karra, Kontgis, et al. (2021). Global land use/land cover with Sentinel-2 and deep learning. IEEE International Geoscience and Remote Sensing Symposium

Kayet, N., Pathak, K., Chakrabarty, A., & Sahoo, S. (2018). Mapping the distribution of iron ore minerals and spatial correlation with environmental variables in hilltop mining areas. *Environmental Earth Sciences*, *77*, 1-14.

Khalifa, A., Çakır, Z., Kaya, Ş., & Gabr, S. (2020). ASTER spectral band ratios for lithological mapping: a case study for measuring geological offset along the Erkenek Segment of the East Anatolian Fault Zone, Turkey. *Arabian Journal of Geosciences*, *13*, 1-8.

Kruse, F. A., & Perry, S. B. (2013). Mineral mapping using simulated WorldView-3 Short-Wave-Infrared imagery. Remote Sensing, 5(6), 2688–2703. https://doi.org/10.3390/rs5062688

Lanfranchi, R. A., Cruz, S. C. P., & Rocha, W. F. (2021). Application of remote sensing and reflectance spectroscopy to explore iron-enriched domains in the north region of the intracontinental sector of the Araçuaí West Congo Orogen. Ore Geology Reviews, 128, 103916. https://doi.org/10.1016/j.oregeorev.2020.103916

Lillesand, T., Kiefer, R. W., & Chipman, J. (2015). *Remote sensing and image interpretation*. John Wiley & Sons.

Lupa, M., Adamek, K., Leśniak, A., & Pršek, J. (2023). Application of satellite remote sensing methods in mineral prospecting in Kosovo, area of Selac. Gospodarka Surowcami Mineralnymi. https://doi.org/10.24425/gsm.2020.132554

Marzouki, A., & Dridri, A. (2022). Lithological discrimination and lineaments extraction using Landsat 8 & ASTER data, a case study of Jbel Saghro (Moroccan Anti-Atlas).

Meima, J. A., & Rammlmair, D. (2020). Investigation of compositional variations in chromitite ore with imaging Laser Induced Breakdown Spectroscopy and Spectral Angle Mapper classification algorithm. *Chemical Geology*, *532*, 119376.

Noori, L., Pour, A. B., Askari, G., Taghipour, N., Pradhan, B., Lee, C., & Honarmand, M. (2019). Comparison of different algorithms to map hydrothermal alteration zones using ASTER remote sensing data for polymetallic Vein-Type Ore exploration: Toroud–Chahshirin Magmatic Belt (TCMB), North Iran. Remote Sensing, 11(5), 495. https://doi.org/10.3390/rs11050495

Okada, K. (2022). Breakthrough technologies for mineral exploration. *Mineral Economics*, *35*(3-4), 429-454.

Ombiro, S. O., Olatunji, A. S., Mathu, E. M., & Ajayi, T. R. (2021). Integration of geophysics and remote sensing techniques in mapping zones mineralised with disseminated gold and sulphide minerals in Lolgorien, Narok County, Kenya. *Tanzania Journal of Science*, *47*(2), 754-768.

Osinowo, O. O., Gomy, A., & Isseini, M. (2021). Mapping hydrothermal alteration mineral deposits from Landsat 8 satellite data in Pala, Mayo Kebbi Region, Southwestern Chad. *Scientific African*, *11*, e00687.

Oskouei, M. M. (2010). Independent component analysis of Hyperion data to map alteration zones. *Journal of photogrammetry, remote sensing and geoinformation processing (PFG)*, *3*, 179-189.

Ourhzif, Z., Algouti, A., & Hadach, F. (2019). Lithological mapping using landsat 8 oli and aster multispectral data in imini-ounilla district south high atlas of marrakech. *The International Archives of the Photogrammetry, Remote Sensing and Spatial Information Sciences*, *42*, 1255-1262.

Pan, Z., Huang, J., & Wang, F. (2013). Multi range spectral feature fitting for hyperspectral imagery in extracting oilseed rape planting area. *International Journal of Applied Earth Observation and Geoinformation*, *25*, 21-29.

Peyghambari, S., & Zhang, Y. (2021). Hyperspectral remote sensing in lithological mapping, mineral exploration, and environmental geology: an updated review. *Journal of Applied Remote Sensing*, *15*(3), 031501-031501.

Pour, A. B., Park, T. S., Park, Y., Hong, J. K., & Pradhan, B. (2019). Application of Constrained Energy Minimization (CEM) algorithm to ASTER data for alteration mineral mapping. IEE Geoscience and Remote Sensing Symposium. https://doi.org/10.1109/igarss.2019.8900375

Pour, A. B., Ranjbar, H., Sekandari, M., El-Wahed, M. A., Hossain, M. S., Hashim, M., Yousefi, M., Zoheir, B., Wambo, J. D. T., & Muslim, A. M. (2023). Remote sensing for mineral exploration. In Elsevier eBooks (pp. 17–149). https://doi.org/10.1016/b978-0-323-95608-6.00002-0

Raggiunti, M., Keir, D., & Pagli, C. (2021). Mapping hydrothermal alteration at the Fentale-Dofan magmatic segment of the Main Ethiopian Rift. *Frontiers in Earth Science*, 712.

Rani, N., Ahirwar, S. K., Anoop, V., & Krishnamurthy, K. (2023). Mineral Mapping through Advanced Airborne Hyperspectral Remote Sensing Techniques.

Rouse, J. W., Jr, Haas, R. H., Schell, J. A., & Deering, D. W. (1974, January 1). Monitoring vegetation systems in the Great Plains with ERTS. NASA Technical Reports Server (NTRS). https://ntrs.nasa.gov/citations/19740022614

Saibi, H., Bersi, M., Mia, M. B., Saadi, N. M., Al Bloushi, K. M. S., & Avakian, R. W. (2018). Applications of remote sensing in geoscience. *Recent Advances and Applications in Remote Sensing*, *181*.

Sembroni, A., Molin, P., Dramis, F., & Bekele, A. (2017). Geology of the Tekeze River basin (Northern Ethiopia). Journal of Maps, 13(2), 621–631. https://doi.org/10.1080/17445647.2017.1351907

Seid, A., & Suryanarayana, T. (2021). Identification of Lithology and Structures in Serdo, Afar, Ethiopia Using Remote Sensing and Gis Techniques.

Shaik, I., Begum, S., Nagamani, P., & Kayet, N. (2021). Characterization and mapping of hematite ore mineral classes using hyperspectral remote sensing technique: a case study from Bailadila iron ore mining region. *SN Applied Sciences*, *3*, 1-13.

Sharma, R., Bisen, D.P., Shukla, U., & Sharma, B. (2012). X-ray diffraction: a powerful method of characterizing nanomaterials. Recent Research in Science and Technology, 4, 77-79

Shebl, A., Abdellatif, M., Badawi, M. A., Dawoud, M. M., Fahil, A. S., & Csámer, Á. (2023). Towards better delineation of hydrothermal alterations via multi-sensor remote sensing and airborne geophysical data. *Scientific Reports*, *13*(1). https://doi.org/10.1038/s41598-023-34531-y

Shirazi, A., Hezarkhani, A., Shirazy, A., & Shahrood, I. (2018). Remote sensing studies for mapping of iron oxide regions, South of Kerman, Iran. *International Journal of Science and Engineering Applications*, *7*(4), 45-51.

Shirazy, A., Shirazi, A., & Nazerian, H. (2021). Application of remote sensing in earth sciences–a review. *International Journal of Science and Engineering Applications*, *10*(5), 45-51.

Shirmard, H., Farahbakhsh, E., Beiranvand Pour, A., Muslim, A. M., Müller, R. D., & Chandra, R. (2020). Integration of selective dimensionality reduction techniques for mineral exploration using ASTER satellite data. *Remote Sensing*, *12*(8), 1261.

Shume, A. (2019). *Major Resource Bases and Constraints for development of Waghemira zone: A Short Synopsis*

Sun, Y., Tian, S., & Di, B. (2017). Extracting mineral alteration information using WorldView-3 data. Geoscience Frontiers, 8(5), 1051–1062. https://doi.org/10.1016/j.gsf.2016.10.008

Tadesse, S., Milesi, J.-P., & Deschamps, Y. (2003). Geology and mineral potential of Ethiopia: a note on geology and mineral map of Ethiopia. *Journal of African Earth Sciences*, *36*(4), 273-313.

Traore, M., Çan, T., & Tekin, S. (2020). Discrimination of iron deposits using feature oriented principal component selection and band ratio methods: Eastern Taurus/TURKEY. *International Journal of Environment and Geoinformatics*, *7*(2), 147-156.

Van Der Meer, F. (2004). Analysis of spectral absorption features in hyperspectral imagery. *International Journal of Applied Earth Observation and Geoinformation*, *5*(1), 55-68.

Van der Werff, H., & Van der Meer, F. (2015). Sentinel-2 for mapping iron absorption feature parameters. *Remote Sensing*, *7*(10), 12635-12653.

Van der Werff, H., & Van der Meer, F. (2016). Sentinel-2A MSI and Landsat 8 OLI provide data continuity for geological remote sensing. *Remote Sensing*, *8*(11), 883.

Vignesh, K. M., & Kiran, Y. (2020). Comparative analysis of mineral mapping for hyperspectral and multispectral imagery. *Arabian Journal of Geosciences*, *13*(4), 160.

Waktola Merera, M. T. U. M. A. L. I. K. E. M. a. A. S. (2021). Geological Mapping and Economic mineralization prospectivity by Remote Sensing and GIS-based Integration around Keleltu Say Area, West Guji Zone, southern Ethiopia. *Zenodo (CERN European Organization for Nuclear Research)*, *8*(12).

Wu, C., Dai, J., Zhou, A., He, L., Tian, B., Lin, W., Zhao, T., & Bai, L. (2023). Mapping alteration zones in the Southern section of Yulong copper belt, Tibet using multi-source remote sensing data. *Frontiers in Earth Science*, *11*, 1164131.

Yang, J., & Cheng, Q. (2015). A comparative study of independent component analysis with principal component analysis in geological objects identification, Part I: Simulations. *Journal of Geochemical Exploration*, *149*, 127-135.

Yousefi, S. J., Ranjbar, H., Alirezaei, S., & Dargahi, S. (2018). Application of mixture tuned matched filtering on ASTER data for hydrothermal alteration mapping related. . . ResearchGate. https://www.researchgate.net/publication/327830230_Application_of_mixture_tuned_matched_filtering_on_ASTER_data_for_hydrothermal_alteration_mapping_related_to_porphyry_Cu_deposits_in_Jabal-Barez_Ranges_Kerman_Copper_Belt_Iran

Zadeh, M. H., Tangestani, M. H., Roldan, F. V., & Yusta, I. (2013). Mineral exploration and alteration zone mapping using mixture tuned matched filtering approach on ASTER data at the central part of Dehaj-Sarduiyeh copper belt, SE Iran. *IEEE Journal of Selected Topics in Applied Earth Observations and Remote Sensing*, *7*(1), 284-289.

Zhang, X., & Li, P. (2014). Lithological mapping from hyperspectral data by improved use of spectral angle mapper. *International Journal of Applied Earth Observation and Geoinformation*, *31,* 95-109

Appendices

Appendix 1: Known iron ore occurrence maps (Source: Access Capital Services SC, 2012)

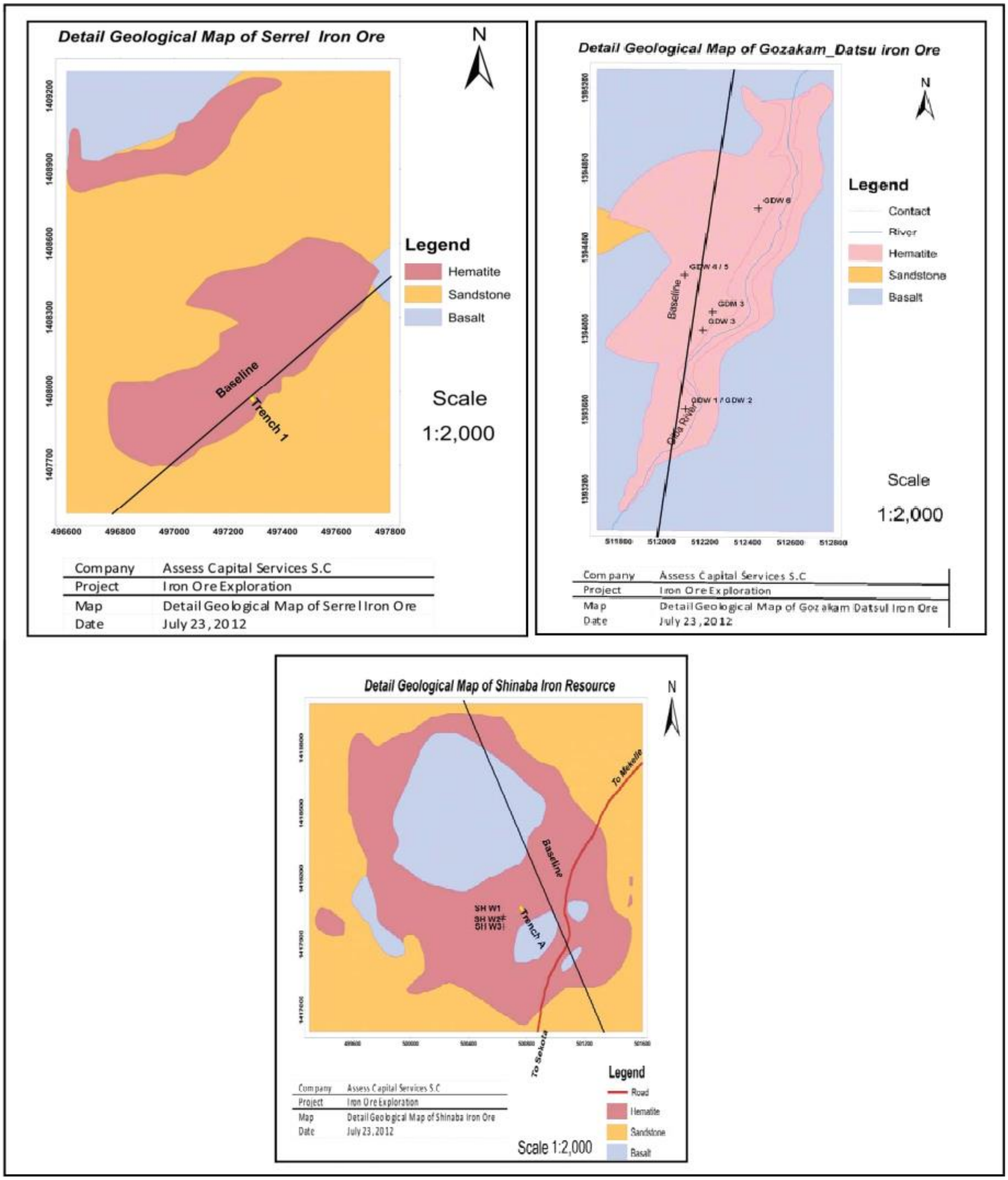

Appendix 2: Secondary geochemical analysis data (Source: Ethiopian Geological Institute)

GEOLOGICAL SURVEY OF ETHIOPIA | Doc.Number: GLD/F5.10.2 | Version No: 1

GEOCHEMICAL LABORATORY DIRECTORATE | Page 1 of 1

Document Title: **Complete Silicate Analysis Report** | Effective date: May, 2017

Issue Date: -30/09/2020

Customer Name: - Wubante Fikadu (GSE)

Request No.- GLD/RQ/04(C)/20

Report No:- GLD/RN/607/20

Sample type:- Rock Sample

Sample Preparation: - 200 Mesh

Date Submitted: - 09/07/2020

Number of Sample:- Therty Four (34)

Analytical Result: In percent (%) Element to be determined Major Oxides & Minor Oxides

Analytical Method: LiBO, FUSION, HF attack, GRAVIMETERIC, COLORIMETRIC and AAS

Collector's code	SiO_2	Al_2O_3	Fe_2O_3	CaO	MgO	Na_2O	K_2O	MnO	P_2O_5	TiO_2	H_2O	LOI
Sn-b1-s1	31.10	11.06	49.08	<0.01	<0.01	<0.01	1.60	<0.01	0.04	0.18	0.52	7.68
Sn-b1-s2	41.24	7.70	42.08	<0.01	<0.01	<0.01	<0.01	<0.01	0.71	0.35	0.74	5.85
Sn-b1-s3	29.06	12.52	51.32	<0.01	<0.01	<0.01	<0.01	<0.01	0.08	0.29	0.53	6.50
Sn-b1-s4	79.92	3.52	10.04	0.96	<0.01	<0.01	<0.01	<0.01	0.10	0.29	1.47	4.33
Sn-b1-s5	32.12	12.10	49.16	<0.01	<0.01	<0.01	<0.01	<0.01	0.14	0.27	0.47	6.28
Sn-b1-s6	65.82	4.40	25.32	0.44	<0.01	0.28	<0.01	<0.01	0.02	0.26	0.40	3.13
Sn-b1-s7	30.46	13.76	48.56	<0.01	<0.01	<0.01	<0.01	<0.01	0.13	0.30	0.38	6.46
Sn-b1-s8	30.50	11.60	50.56	<0.01	<0.01	<0.01	<0.01	<0.01	0.02	0.33	0.61	7.11
Sn b1-s9	30.34	7.98	55.56	<0.01	<0.01	<0.01	<0.01	<0.01	0.07	0.24	0.46	5.64
Sn-b1-s10	28.02	8.26	49.52	<0.01	<0.01	<0.01	2.00	0.04	0.39	2.40	2.12	5.56
Sn-b1-s11	29.08	10.26	53.28	<0.01	<0.01	<0.01	<0.01	<0.01	0.08	0.27	0.42	6.05
Sn-b2-s1	29.82	11.14	51.84	<0.01	<0.01	<0.01	<0.01	<0.01	0.07	0.30	0.72	5.50
Sn-b2-s2	24.46	9.90	58.40	<0.01	<0.01	<0.01	<0.01	<0.01	0.21	0.25	0.84	4.90
Sn-b2-s3	65.52	18.56	7.76	<0.01	<0.01	<0.01	<0.01	<0.01	0.36	0.22	0.34	8.71
Sn-b2-s4	75.60	13.78	6.28	<0.01	<0.01	<0.01	<0.01	<0.01	0.14	0.43	0.29	6.43
Sn-b2-s5	42.00	9.56	44.08	<0.01	<0.01	<0.01	<0.01	<0.01	0.15	0.28	0.54	3.98
Sn-b2-s6	34.46	11.28	46.44	<0.01	<0.01	<0.01	<0.01	<0.01	0.15	0.28	0.25	6.34
Sn-b2-s7	21.56	9.36	61.24	<0.01	<0.01	<0.01	<0.01	<0.01	0.21	0.23	0.30	6.42

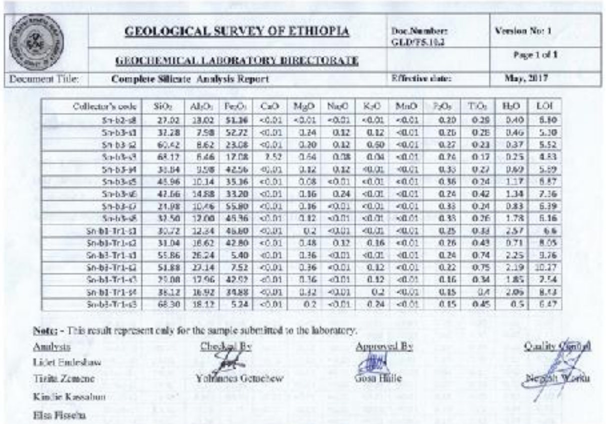

GEOLOGICAL SURVEY OF ETHIOPIA | Doc.Number: GLD/F5.10.2 | Version No: 1

GEOCHEMICAL LABORATORY DIRECTORATE | Page 1 of 1

Document Title: **Complete Silicate Analysis Report** | Effective date: May, 2017

Collector's code	SiO_2	Al_2O_3	Fe_2O_3	CaO	MgO	Na_2O	K_2O	MnO	P_2O_5	TiO_2	H_2O	LOI
Sn-b2-s8	27.02	13.02	51.36	<0.01	<0.01	<0.01	<0.01	<0.01	0.20	0.29	0.40	6.80
Sn-b3-s1	32.28	7.98	52.72	<0.01	0.24	0.12	0.12	<0.01	0.26	0.28	0.46	5.30
Sn b3 s2	60.42	8.62	23.08	<0.01	0.20	0.12	0.60	<0.01	0.27	0.23	0.37	5.52
Sn-b3-s3	68.12	6.46	17.08	2.52	0.64	0.08	0.04	<0.01	0.76	0.17	0.25	4.53
Sn-b3-s4	30.84	9.58	42.56	<0.01	0.12	0.12	<0.01	<0.01	0.33	0.27	0.69	5.59
Sn-b3-s5	45.96	10.14	35.36	<0.01	0.08	<0.01	<0.01	<0.01	0.36	0.24	1.17	6.87
Sn-b3-s6	47.66	14.88	33.20	<0.01	0.16	0.24	<0.01	<0.01	0.24	0.42	1.34	7.36
Sn-b3-s7	21.98	10.46	55.80	<0.01	0.16	<0.01	<0.01	<0.01	0.33	0.24	0.83	6.39
Sn-b3-s8	32.50	12.00	45.96	<0.01	0.12	<0.01	<0.01	<0.01	0.33	0.26	1.78	6.16
Sn-b1-Tr1-s1	30.72	12.34	46.80	<0.01	0.2	<0.01	<0.01	<0.01	0.25	0.33	2.57	6.6
Sn-b1-Tr1-s2	31.04	16.62	42.80	<0.01	0.48	0.12	0.16	<0.01	0.26	0.43	0.71	8.05
Sn-b3-Tr1-s1	55.86	26.24	5.40	<0.01	0.36	<0.01	<0.01	<0.01	0.24	0.74	2.25	9.76
Sn-b3-Tr1-s2	51.88	27.14	7.52	<0.01	0.36	<0.01	0.12	<0.01	0.22	0.75	2.19	10.27
Sn-b1-Tr1-s3	29.08	17.96	42.92	<0.01	0.16	<0.01	0.12	<0.01	0.16	0.34	1.85	7.54
Sn-b1-Tr1-s4	38.12	16.92	34.88	<0.01	0.32	<0.01	0.2	<0.01	0.15	0.4	2.06	8.53
Sn-b3-Tr1-s3	68.30	18.12	5.24	<0.01	0.2	<0.01	0.24	<0.01	0.15	0.45	0.5	6.47

Note: - This result represent only for the sample submitted to the laboratory.

Analysts	Checked By	Approved By	Quality Control
Lidet Endeshaw			
Tirita Zemene	Yohannes Getachew	Gosa Haile	Negash Worku
Kindie Kassahun			
Elsa Fisseha			

GEOLOGICAL SURVEY OF ETHIOPIA | Doc.Number: GLD/F5.10.2 | Version No: 1

GEOCHEMICAL LABORATORY DIRECTORATE | Page 1 of 1

Document Title: **Complete Silicate Analysis Report** | Effective date: May, 2017

Issue Date: -30/09/2020

Customer Name: - Wubante Fikadu (GSE)

Request No:- GLD/RQ/04(B)/20

Report No:- GLD/RN/606/20

Sample type:- Rock Sample

Sample Preparation: - 200 Mesh

Date Submitted: - 06/07/2020

Number of Sample:- Seventeen (17)

Analytical Result: In percent (%) Element to be determined Major Oxides & Minor Oxides

Analytical Method: LiBO, FUSION, HF attack, GRAVIMETERIC, COLORIMETRIC and AAS

Collector's code	SiO_2	Al_2O_3	Fe_2O_3	CaO	MgO	Na_2O	K_2O	MnO	P_2O_5	TiO_2	H_2O	LOI
Mi-b1-s1	48.74	5.64	42.20	<0.01	<0.01	<0.01	<0.01	<0.01	0.30	0.23	0.30	3.55
Mi-b1-s2	33.00	10.14	49.36	<0.01	<0.01	<0.01	<0.01	0.04	0.18	0.25	1.03	5.44
Mi-b1-s3	73.42	<0.01	22.92	<0.01	<0.01	<0.01	<0.01	0.04	0.13	0.25	0.53	1.37
Mi-b1-s4	42.36	14.38	35.08	0.64	<0.01	<0.01	<0.01	<0.01	0.21	0.24	0.53	6.43
Mi-b1-s5	58.26	1.46	38.36	0.36	<0.01	<0.01	<0.01	<0.01	0.29	0.14	0.35	2.39
Mi-b1-s6	33.34	10.06	50.44	0.28	<0.01	<0.01	<0.01	<0.01	0.19	0.23	0.71	4.96
Mi-b1-s7	34.96	10.66	46.74	0.58	<0.01	<0.01	<0.01	<0.01	0.21	0.21	0.67	5.71
Mi-b1-s8	38.12	13.94	42.80	<0.01	<0.01	<0.01	<0.01	<0.01	0.18	0.15	0.90	5.08
Mi-b1-s9	33.16	10.22	50.10	0.24	<0.01	<0.01	<0.01	<0.01	0.21	0.15	1.17	5.46
Mi-b1-s10	36.78	10.66	45.32	0.52	<0.01	<0.01	<0.01	<0.01	0.27	0.18	0.97	5.62
Mi-b1-Tr1-S1	68.76	15.44	5.88	1.44	<0.01	<0.01	<0.01	<0.01	0.41	0.43	1.01	6.58
Mi-b1-Tr2-S1	42.40	13.56	34.36	0.76	<0.01	<0.01	<0.01	<0.01	0.24	0.29	1.27	6.36
Mi-b1 Tr2-S2	37.74	19.20	31.80	<0.01	<0.01	<0.01	<0.01	<0.01	0.31	0.33	2.94	7.34

GEOLOGICAL SURVEY OF ETHIOPIA | Doc.Number: GLD/F5.10.2 | Version No: 1

GEOCHEMICAL LABORATORY DIRECTORATE | Page 1 of 1

Document Title: **Complete Silicate Analysis Report** | Effective date: May, 2017

Issue Date: -30/09/2020

Customer Name: - Wubante Fikadu (GSE)

Request No:- GLD/RQ/04(D)/20

Report No:- GLD/RN/608/20

Sample type:- Rock Sample

Sample Preparation: - 200 Mesh

Date Submitted: - 09/07/2020

Number of Sample:- Twenty Two (22)

Analytical Result: In percent (%) Element to be determined Major Oxides & Minor Oxides

Analytical Method: LiBO, FUSION, HF attack, GRAVIMETERIC, COLORIMETRIC and AAS

Collector's code	SiO_2	Al_2O_3	Fe_2O_3	CaO	MgO	Na_2O	K_2O	MnO	P_2O_5	TiO_2	H_2O	LOI
sk-s1	32.42	11.08	49.88	<0.01	0.20	<0.01	<0.01	<0.01	0.14	0.23	0.49	5.76
sk-s2	29.56	10.56	54.20	<0.01	0.12	<0.01	<0.01	<0.01	0.17	0.23	0.48	5.21
sk-s3	27.98	10.04	55.00	<0.01	<0.01	<0.01	<0.01	<0.01	0.36	0.27	<0.01	6.14
sk-s4	32.48	9.90	51.04	<0.01	<0.01	<0.01	<0.01	<0.01	0.36	0.24	0.16	5.85
sk-s5	24.60	17.28	50.40	<0.01	<0.01	<0.01	<0.01	<0.01	0.37	0.3	0.43	5.61
sk-s6	40.02	9.00	45.68	<0.01	0.12	<0.01	<0.01	<0.01	0.2	0.23	0.28	3.4
sk-s7	42.90	12.62	38.88	<0.01	<0.01	<0.01	<0.01	<0.01	0.57	0.36	0.29	5.42
sk-s8	43.12	19.74	26.96	0.64	0.24	<0.01	<0.01	<0.01	0.3	0.32	0.72	7.75
sk-b1-Tr1-s1	51.92	10.56	27.64	<0.01	0.16	<0.01	<0.01	<0.01	0.25	0.4	0.64	7.9
sk-b1-Tr1-s2	28.48	11.14	53.44	<0.01	0.2	0.08	<0.01	<0.01	0.19	0.24	0.46	5.14
sk-b1-Tr1-s3	27.60	7.96	57.40	<0.01	0.32	0.32	<0.01	<0.01	0.17	0.22	0.77	5.04
sk-b1-Tr1-s4	38.74	22.04	26.12	2.04	<0.01	<0.01	0.88	<0.01	0.26	0.30	0.73	8.61
sk-b3-s1	20.54	13.22	45.60	2.12	<0.01	<0.01	0.80	<0.01	0.36	0.17	0.41	7.37

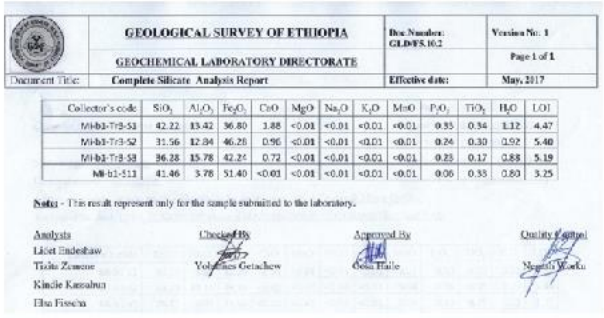

GEOLOGICAL SURVEY OF ETHIOPIA | Doc.Number: GLD/F5.10.2 | Version No: 1

GEOCHEMICAL LABORATORY DIRECTORATE | Page 1 of 1

Document Title: **Complete Silicate Analysis Report** | Effective date: May, 2017

Collector's code	SiO_2	Al_2O_3	Fe_2O_3	CaO	MgO	Na_2O	K_2O	MnO	P_2O_5	TiO_2	H_2O	LOI
Mi-b1-Tr3-S1	42.22	13.42	36.80	1.88	<0.01	<0.01	<0.01	<0.01	0.35	0.34	1.12	4.47
Mi-b1-Tr3-S2	31.56	12.84	46.28	0.96	<0.01	<0.01	<0.01	<0.01	0.24	0.30	0.92	5.40
Mi-b1-Tr3-S3	36.28	15.78	42.24	0.72	<0.01	<0.01	<0.01	<0.01	0.23	0.17	0.88	5.19
Mi-b1-S11	41.46	3.78	51.40	<0.01	<0.01	<0.01	<0.01	<0.01	0.06	0.35	0.80	3.25

Note: - This result represent only for the sample submitted to the laboratory.

Analysts	Checked By	Approved By	Quality Control
Lidet Endeshaw			
Tizita Zemene	Yohannes Getachew	Gosa Haile	Negash Worku
Kindie Kassahun			
Elsa Fisseha			

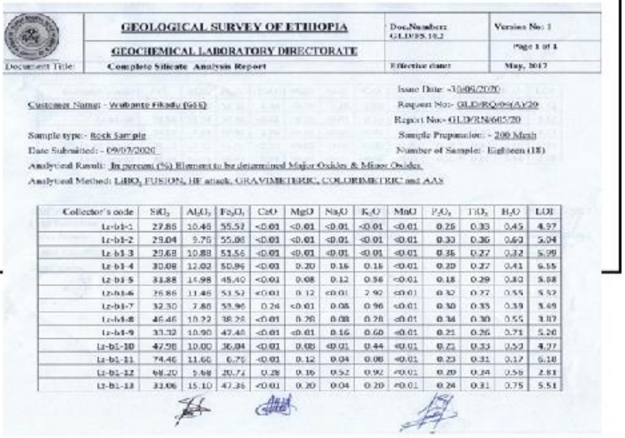

GEOLOGICAL SURVEY OF ETHIOPIA | Doc.Number: GLD/F5.10.2 | Version No: 1

GEOCHEMICAL LABORATORY DIRECTORATE | Page 1 of 1

Document Title: **Complete Silicate Analysis Report** | Effective date: May, 2017

Issue Date: -30/06/2020

Customer Name: - Wubante Fikadu (GSE)

Request No:- GLD/RQ/04(A)/20

Report No:- GLD/RN/605/20

Sample type:- Rock Sample

Sample Preparation: - 200 Mesh

Date Submitted: - 09/07/2020

Number of Sample:- Eighteen (18)

Analytical Result: In percent (%) Element to be determined Major Oxides & Minor Oxides

Analytical Method: $LiBO_2$ FUSION, HF attack, GRAVIMETERIC, COLORIMETRIC and AAS

Collector's code	SiO_2	Al_2O_3	Fe_2O_3	CaO	MgO	Na_2O	K_2O	MnO	P_2O_5	TiO_2	H_2O	LOI
Lz-b1-1	27.86	10.46	55.52	<0.01	<0.01	<0.01	<0.01	<0.01	0.26	0.33	0.45	4.97
Lz-b1-2	29.04	9.76	55.08	<0.01	<0.01	<0.01	<0.01	<0.01	0.30	0.36	0.63	5.04
Lz-b1-3	29.68	10.88	53.56	<0.01	<0.01	<0.01	<0.01	<0.01	0.36	0.27	0.32	5.99
Lz-b1-4	30.08	12.02	50.96	<0.01	0.20	0.16	0.16	<0.01	0.20	0.27	0.41	6.55
Lz-b1-5	31.88	14.98	45.40	<0.01	0.08	0.12	0.56	<0.01	0.18	0.29	0.80	5.88
Lz-b1-6	26.86	11.46	51.52	<0.01	0.12	<0.01	2.92	<0.01	0.32	0.27	0.55	5.52
Lz-b1-7	32.30	7.86	53.96	0.24	<0.01	0.08	0.96	<0.01	0.30	0.35	0.39	3.49
Lz-b1-8	46.46	10.22	38.28	<0.01	0.28	0.08	0.28	<0.01	0.34	0.30	0.55	3.87
Lz-b1-9	33.32	10.90	47.48	<0.01	<0.01	0.16	0.60	<0.01	0.21	0.26	0.71	5.20
Lz-b1-10	47.98	10.00	36.04	<0.01	0.08	<0.01	0.44	<0.01	0.21	0.33	0.53	4.37
Lz-b1-11	74.46	11.60	6.76	<0.01	0.12	0.04	0.08	<0.01	0.23	0.31	0.17	6.18
Lz-b1-12	68.20	5.68	20.72	0.28	0.16	0.52	0.92	<0.01	0.20	0.24	0.56	2.81
Lz-b1-13	33.06	15.10	47.36	<0.01	0.20	0.04	0.20	<0.01	0.24	0.31	0.75	5.51

Appendix 3: XRD raw data and refined/calculated peaks

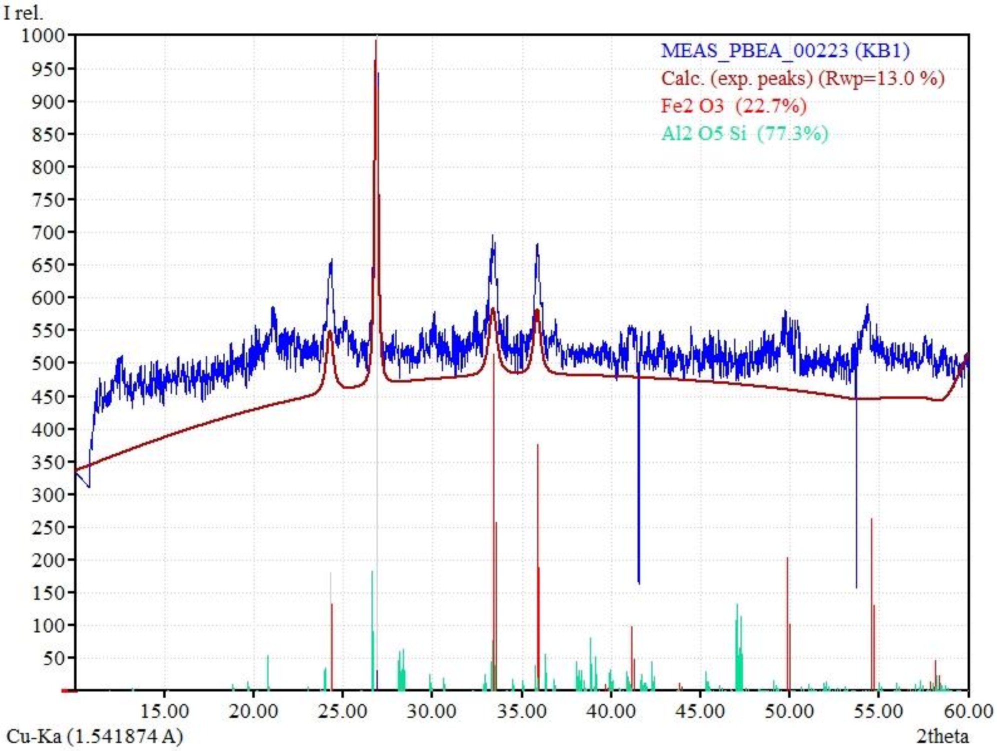

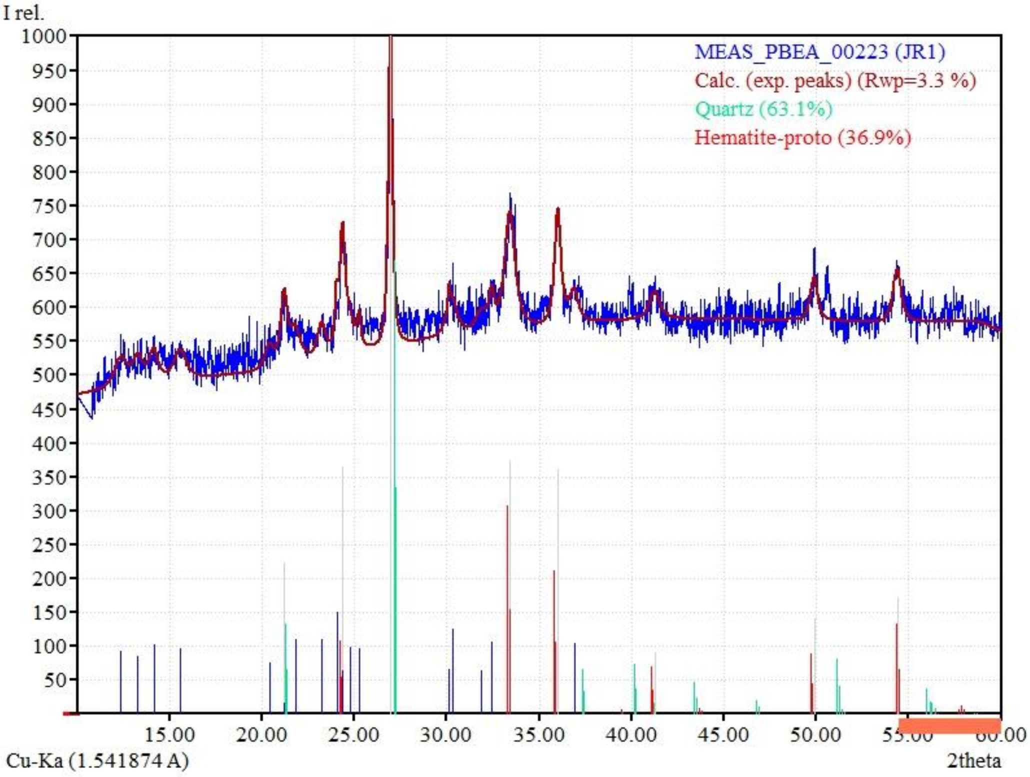

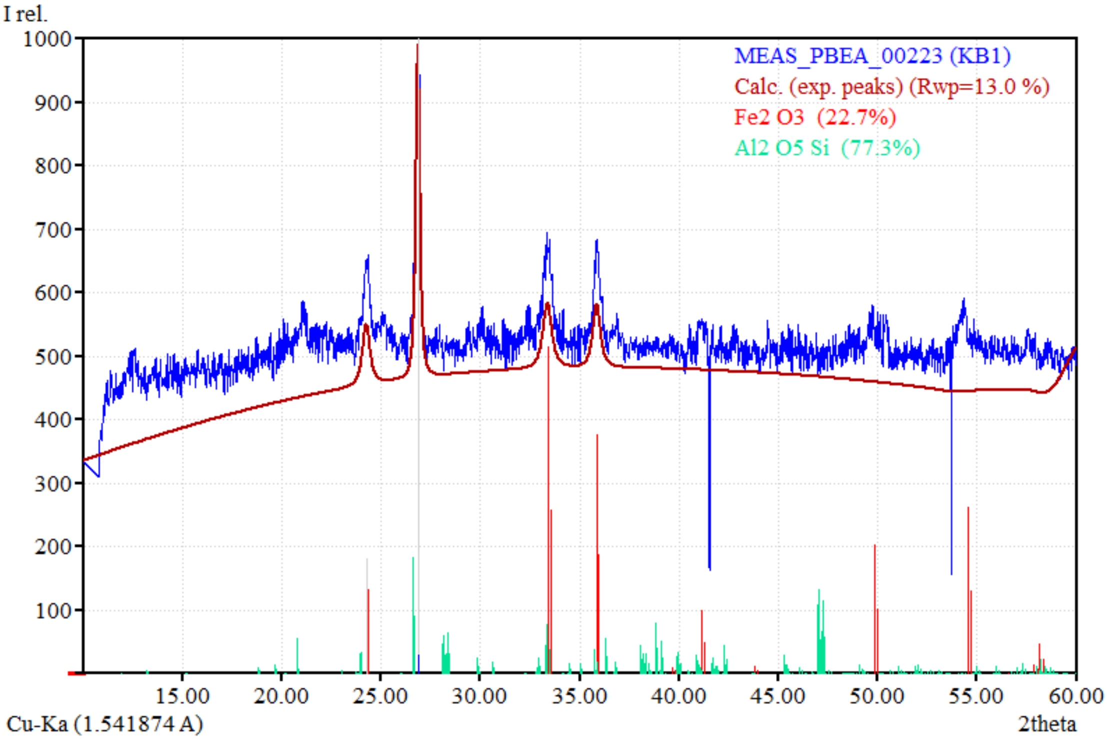
I rel.
1000
900
800
700
600
500
400
300
200
100
15.00
20.00
25.00
30.00
35.00
40.00
45.00
50.00
55.00
60.00
Cu-Ka (1.541874 A)
2theta
MEAS_PBEA_00223 (KB1)
Calc. (exp. peaks) (Rwp=13.0 %)
Fe2 O3 (22.7%)
Al2 O5 Si (77.3%)

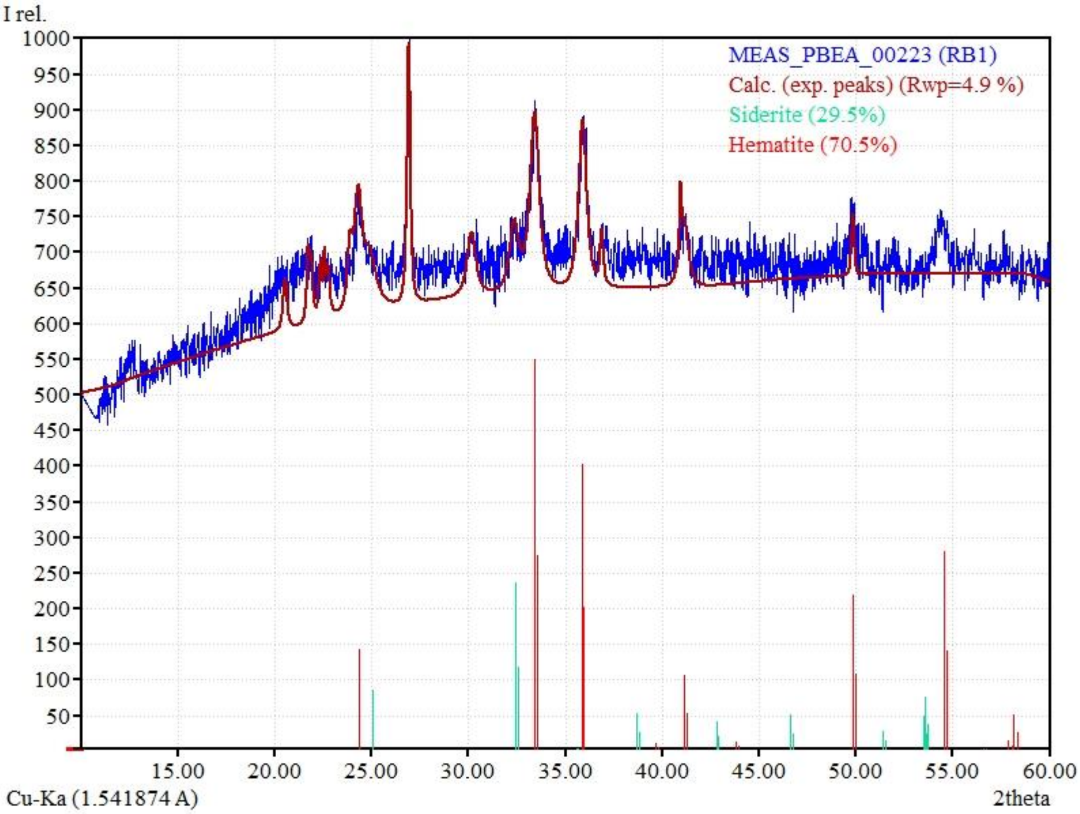
I rel.
1000
950
900
850
800
750
700
650
600
550
500
450
400
350
300
250
200
150
100
50
15.00
20.00
25.00
30.00
35.00
40.00
45.00
50.00
55.00
60.00
Cu-Ka (1.541874 A)
2theta
MEAS_PBEA_00223 (RB1)
Calc. (exp. peaks) (Rwp=4.9 %)
Siderite (29.5%)
Hematite (70.5%)

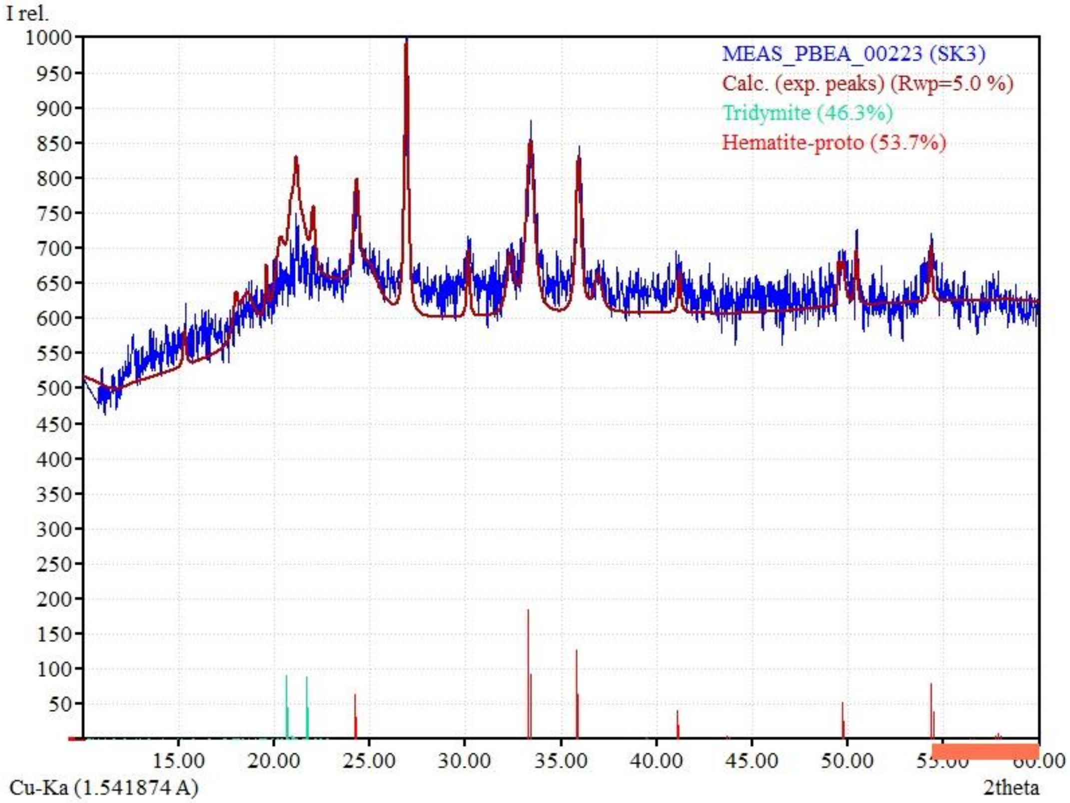
I rel.
1000
950
900
850
800
750
700
650
600
550
500
450
400
350
300
250
200
150
100
50
MEAS_PBEA_00223 (SK3)
Calc. (exp. peaks) (Rwp=5.0 %)
Tridymite (46.3%)
Hematite-proto (53.7%)
15.00
20.00
25.00
30.00
35.00
40.00
45.00
50.00
55.00
60.00
Cu-Ka (1.541874 A)
2theta

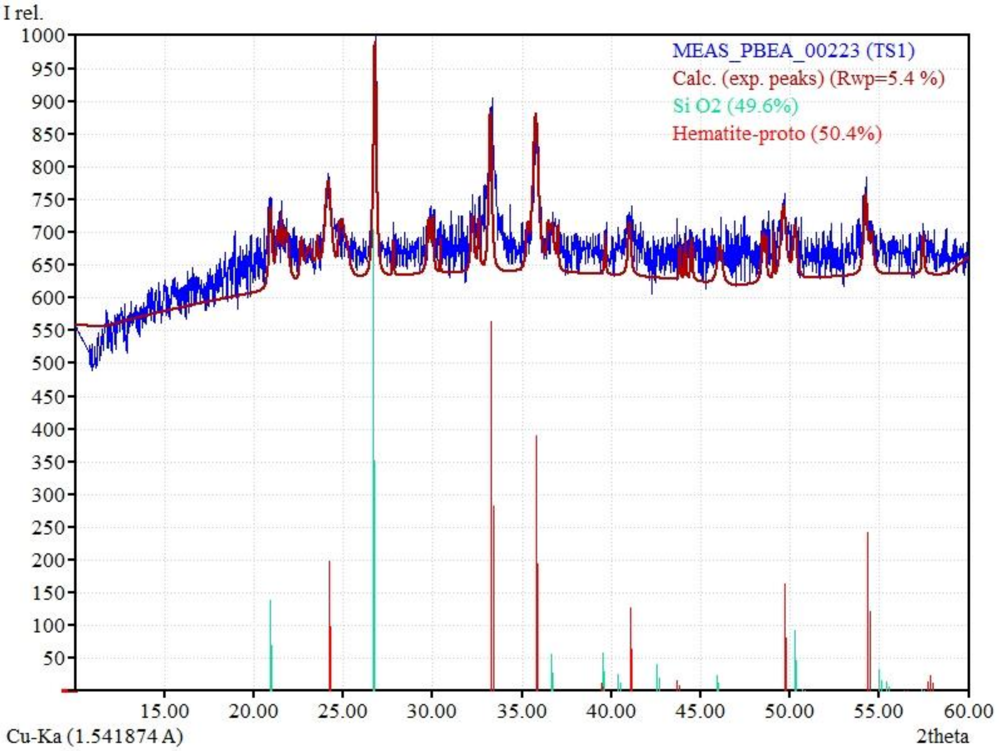
I rel.
1000
950
900
850
800
750
700
650
600
550
500
450
400
350
300
250
200
150
100
50
MEAS_PBEA_00223 (TS1)
Calc. (exp. peaks) (Rwp=5.4 %)
Si O2 (49.6%)
Hematite-proto (50.4%)
15.00
20.00
25.00
30.00
35.00
40.00
45.00
50.00
55.00
60.00
Cu-Ka (1.541874 A)
2theta

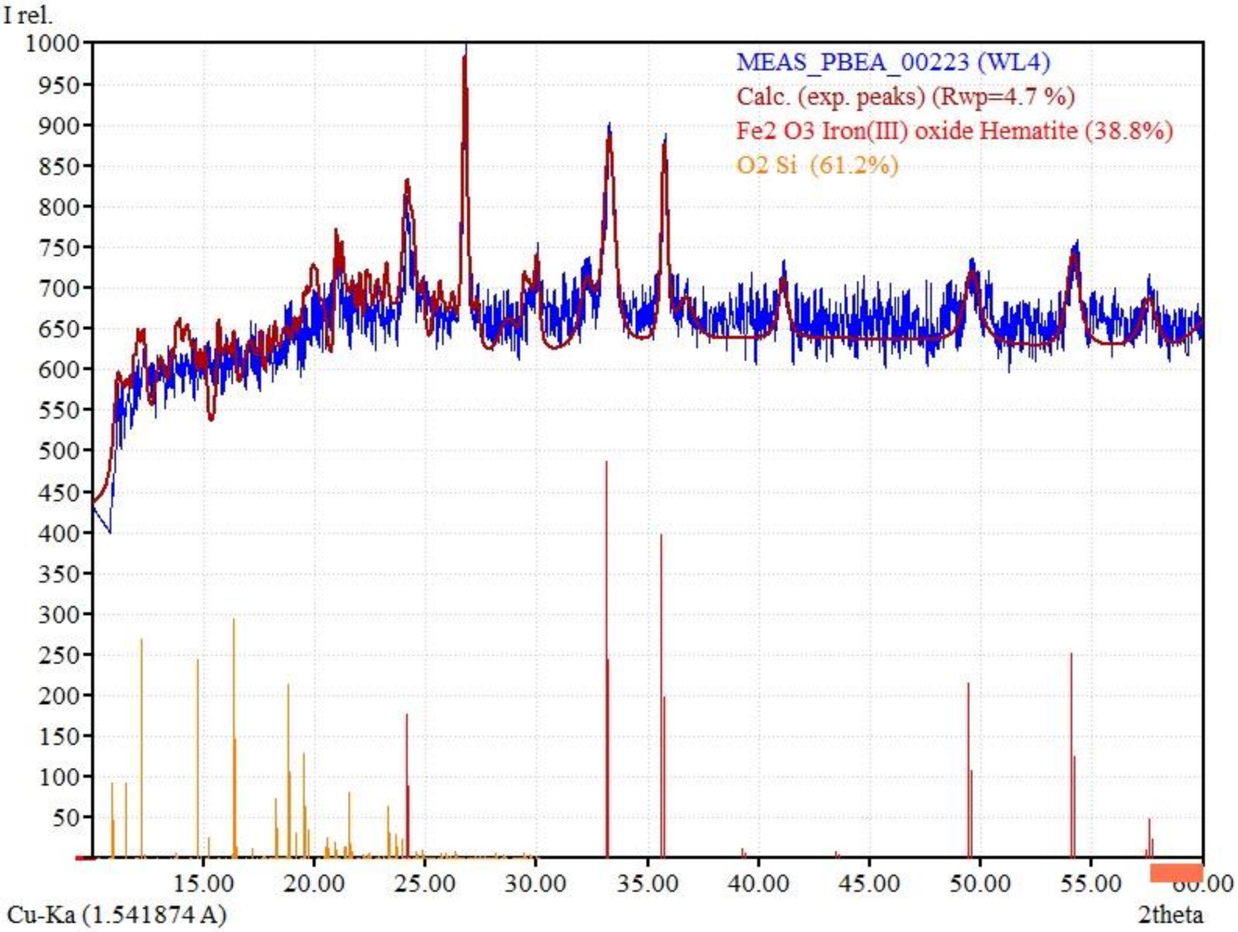
I rel.
1000
950
900
850
800
750
700
650
600
550
500
450
400
350
300
250
200
150
100
50
MEAS_PBEA_00223 (WL4)
Calc. (exp. peaks) (Rwp=4.7 %)
Fe2 O3 Iron(III) oxide Hematite (38.8%)
O2 Si (61.2%)
15.00
20.00
25.00
30.00
35.00
40.00
45.00
50.00
55.00
60.00
Cu-Ka (1.541874 A)
2theta

Appendix 4: Fractional image of band ratios and PCA

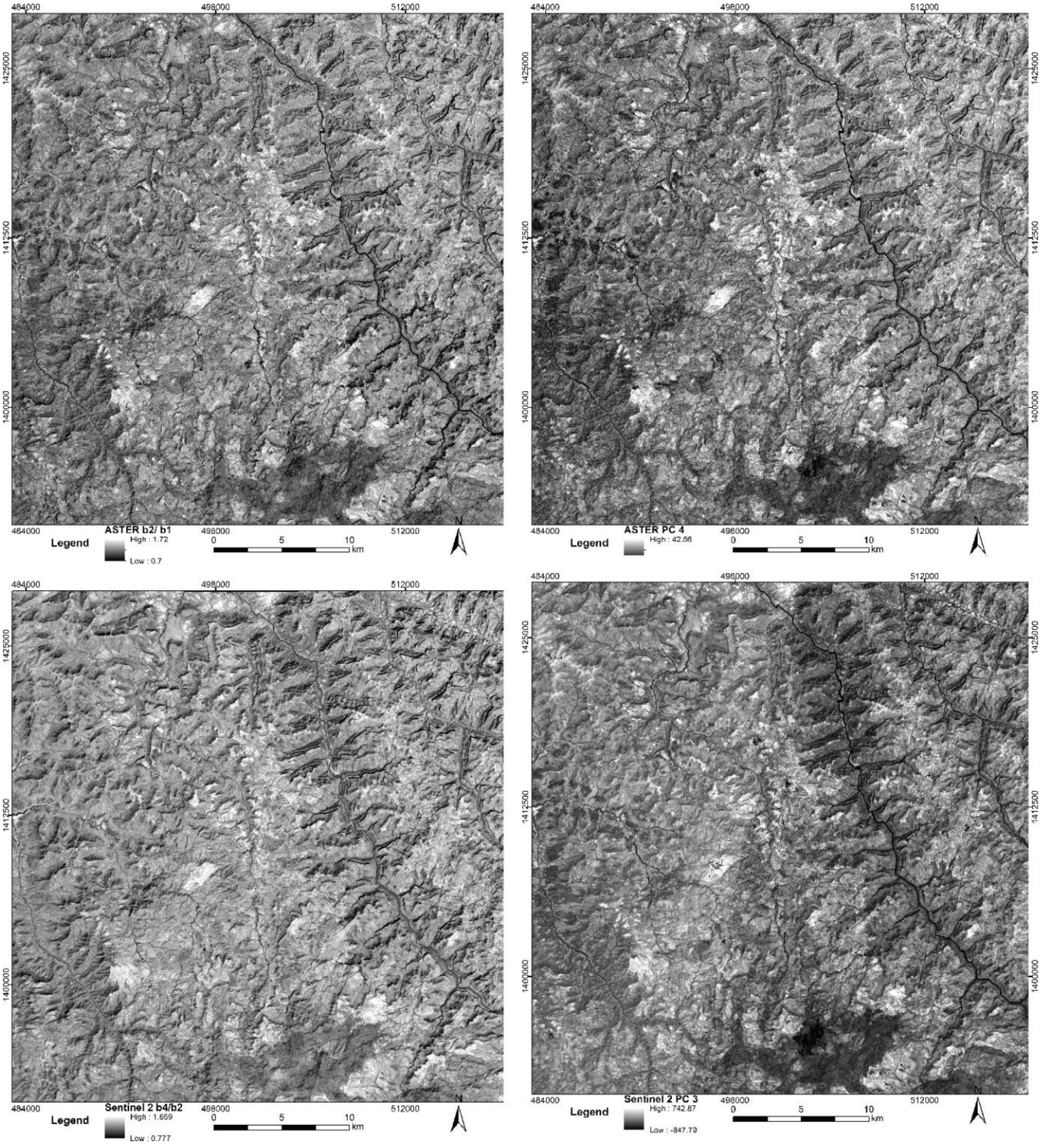

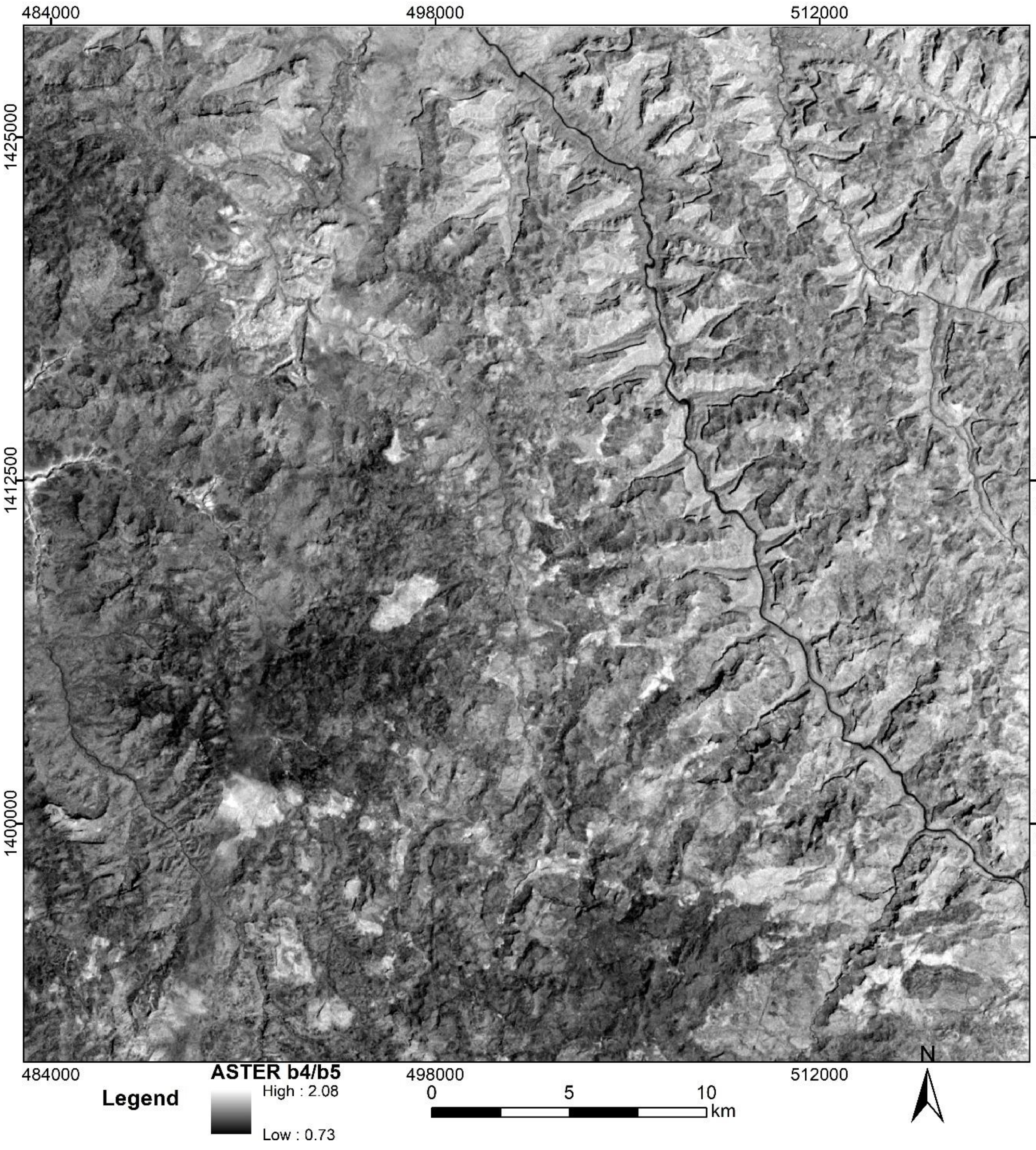
484000
498000
512000
1425000
1412500
1400000
484000
498000
512000
Legend
ASTER b4/b5
High : 2.08
Low : 0.73
0
5
10
km
N

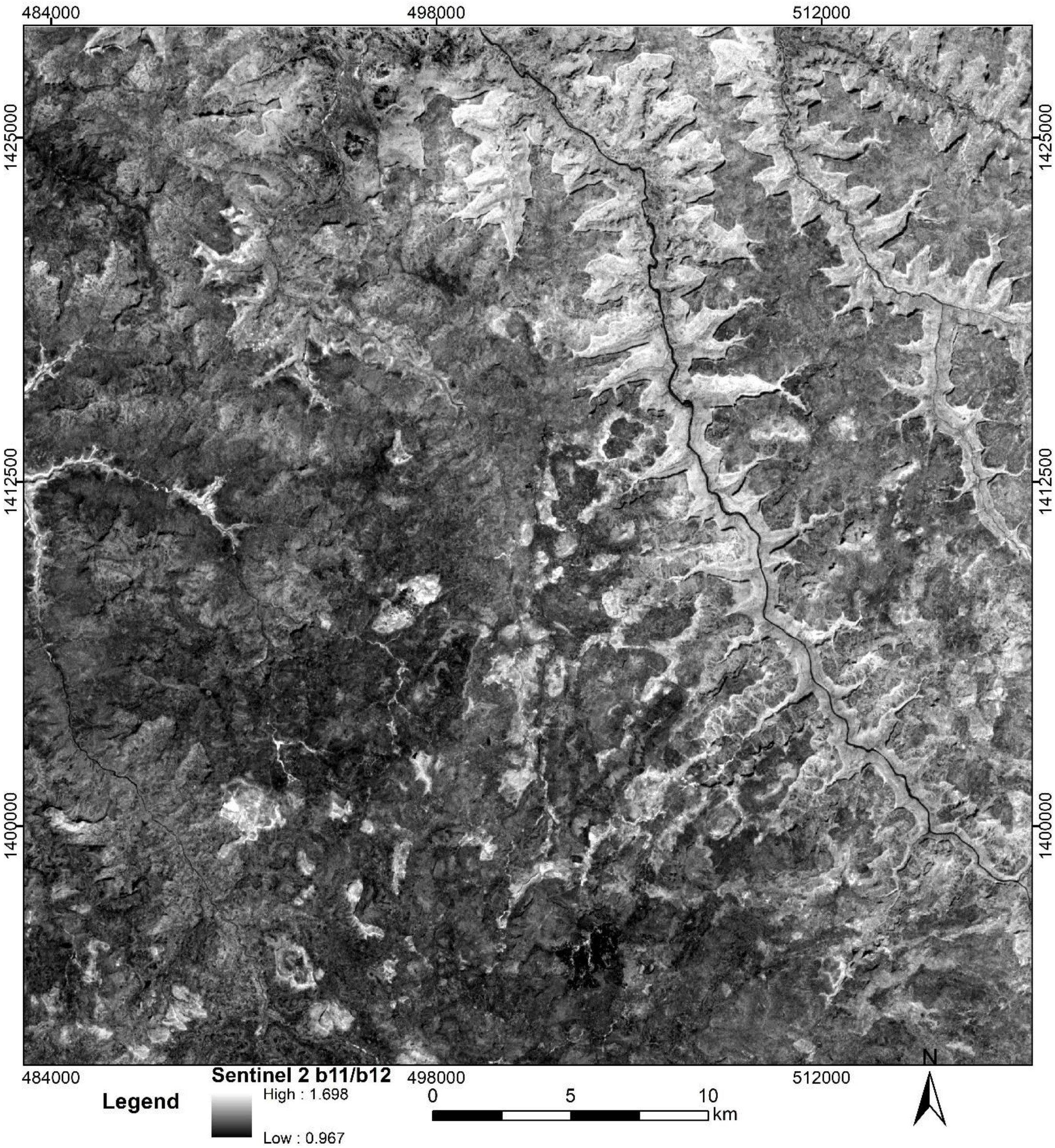

Appendix 5: GEE code used to export mosaicked Sentinel 2 images

```
//This is the Sentinel 2 collection (all the possible available Sentinel-2 imagery)
```

```
var S2_collection = ee.ImageCollection("COPERNICUS/S2")
.filterBounds(geometry)
.filterDate('2023-01-01', '2023-02-28'); // change date range here
// This tells us what images are inside the collection
print(S2_collection);
// These are the bands that we want to be displayed
var S2_bands = ['B1', 'B2', 'B3'];
// This turns the whole S2 collection into one image, finding the middle value for each pixel
var S2_mosaic = S2_collection.median().select(S2_bands).clip(geometry);
// This controls how we want the S2 image to be displayed
var S2_display = {bands: S2_bands, min: 0, max: 3000};
// This adds the S2_mosaic to the map, using the S2_display visual parameters, and giving it the name "S2_Image"
Map.addLayer(S2_mosaic, S2_display, "S2_Image");
// This automatically pans the map to the middle of our area of interest
Map.centerObject(geometry);
// This exports our Sentinel-2 image to Google Drive where we can download it
Export.image.toDrive({
image: S2_mosaic,
description: 'Sentinel-2',
scale: 10,
maxPixels: 1e13,
region: geometry
});
```